

FILTERING OF ACOUSTIC INFORMATION FROM AERO-OPTICAL MEASUREMENTS

A Dissertation

Submitted to the Graduate School
of the University of Notre Dame
in Partial Fulfillment of the Requirements
for the Degree of

Doctor of Philosophy

by
Brian Lowell Catron

R. Mark Rennie , Co-Director

Eric J. Jumper, Co-Director

Graduate Program in Aerospace and Mechanical Engineering

Notre Dame, Indiana

December 2021

Draft document [December 28, 2021 at 0:24]

FILTERING OF ACOUSTIC INFORMATION FROM AERO-OPTICAL MEASUREMENTS

Abstract

by

Brian Lowell Catron

Abstract Goes Here

To my wife Karen & our son Arthur

CONTENTS

Figures	v
Tables	ix
Symbols	xi
Acknowledgments	xiii
Chapter 1: Introduction	1
Chapter 2: Literature Review	7
2.1 Aero-Optics	7
2.1.1 Typical Optical Wavefront Measurement System	10
2.2 Acoustics	14
2.2.1 Basic Acoustics	14
2.2.2 Duct Acoustics	14
2.2.2.1 Characteristic Equations of Cross-Sections	17
Chapter 3: Aero-Optical and Acoustical Coupling	21
3.1 Simulating an Optical Wavefront Measurement from an Acoustic Field Function	21
3.2 Simple Examples of Acoustic-Optical Coupling	23
3.2.1 Planar Acoustic Waves	23
3.2.2 Spherical Acoustic Waves	26
3.2.2.1 Theoretical OPD Calculations	27
3.2.2.2 Measurement of a Spherical Acoustic Wave with an Optical Beam	28
3.3 Estimating the Acoustic Field Inside a Wind-Tunnel Test-Section	32
3.3.1 Mode-Marching Method Procedure	35
3.3.2 University of Notre Dame White Field Wind-Tunnel Simulation	36
3.4 Summary	43
Chapter 4: Multidimensional Spectral Estimation of Optical Wavefronts	45
4.1 One-Dimensional Power Spectrum Calculation	48
4.2 N-Dimensional Power Spectra Calculation	49
4.3 Non-Rectangular Spatial Windows	50
4.4 Wavefront Multidimensional Spectrum	51
4.4.1 2-D Slices of the Multidimensional Spectral Estimation	54
4.4.2 3-D Representations of Multidimensional Spectral Estimation	57
4.4.3 Acoustic Cone	64
4.4.4 Signal Aliasing	65
4.5 Summary	67

Chapter 5: Synthetic Wavefront	69
5.1 General Spectrum Construction	70
5.2 Aero-Optical Signal	73
5.3 Stationary Mode Signals	74
5.4 Sound and Vibration Signals	74
5.4.1 Blade-Passing Frequency Disturbance	74
5.4.2 Acoustic Cone	75
5.5 Mean-Lensing Signal	77
5.6 Background Noise Signal	77
5.7 Synthetic Wavefront Creation	78
5.8 Comparison to Measured Data	78
Chapter 6: Single Sensor Filtering Techniques	83
6.1 Temporal Filter Methods	83
6.2 Upstream/Downstream Moving	85
6.3 Velocity Filtering	89
6.4 Baseline Spectrum	92
6.5 Basic Filter Summary	93
Chapter 7: Multiple Sensor Filtering Techniques	97
7.1 Optical Tip and Tilt	97
7.2 LSE-SPOD	98
7.3 Filtering Experimental Data	101
Chapter 8: Conclusion	111
Bibliography	113

FIGURES

1.1	Diffractive-limited far-field intensity of a beam normalized by the performance at $1\text{-}\mu\text{m}$.	2
1.2	Strehl ratio due to the OPD_{RMS} of the Airborne Laser Laboratory (ALL) at various laser wavelengths. ALL had an estimated Strehl ratio of 95% with its $10.6\text{-}\mu\text{m}$ laser.	3
1.3	Hypothetical iterative design process of an airborne directed-energy system. The required performance level is shown by the red line and the testing environment's contamination is shown by the orange line.	4
2.1	Gladstone-Dale constant for air over the visible wavelength range.	8
2.2	(a) Diffractive limited on target intensity as a function of wavelength normalized by the value at $\lambda = 1 \mu\text{m}$. (b) Strehl ratio as a function of wavelength for an aberration that gives $\text{SR} = 0.95$ at $\lambda = 10.6 \mu\text{m}$.	10
2.3	OPD_{RMS} values necessary to obtain Strehl ratios of 0.9, 0.7, and 0.5 over a range of wavelengths.	11
2.4	Typical double-pass optical wavefront measurement setup.	12
2.5	Diagram of a Shack-Hartmann wavefront sensor comprised of four lenslets. The black line represents the perturbed wavefront and the red line the mean slope over each lenslet. The focal point of the wavefront is shifted by Δx from the center-line of the lenslet based on the mean slope of the wavefront. [1]	13
2.6	Duct with a rectangular cross-section.	15
2.7	Characteristic solutions to Equation 2.26 with rigid wall in a rectangular cross-section where $m=0:2$ and $n=0:3$. Nodal lines are depicted by the dot-dash lines. The cross-sectional wave numbers, k_m , listed are for a duct of unit length and height.	18
2.8	Characteristic solutions to Equation 2.26 with rigid wall in a circular cross-section where $m=0:2$ and $n=0:3$. Nodal lines are depicted by the dot-dash lines. The cross-sectional wave numbers, k_m , listed are for a duct of unit radius.	19
3.1	General geometry for various sample calculations for showing the acoustic-optical coupling effect.	24
3.2	Theoretical time-averaged OPD_{RMS} per meter of beam propagation as a function of sound pressure level, SPL, for several Λ/A_p ratios and $\theta = 0$.	25
3.3	Theoretical time-averaged OPD_{RMS} for a rms sound pressure of 1 Pa (SPL of 94 dB), l_n of 1 m, and various angles and Λ/A_p ratios.	25
3.4	Theoretical time-averaged OPD_{RMS} for the two acoustic waves ($u+c$ and $u-c$) for the blade pass frequency (534 Hz) at Mach 0.6 with a RMS sound pressure of 1 Pa (SPL of 94 dB), l_n of 1 m, and A_p of 15 cm.	26
3.5	Diagram of the geometry used in the spherical wave simulation.	28
3.6	Theoretical time-averaged OPD_{RMS} for a spherical acoustic wave. The top plot shows a perfect spherical acoustic signal integrated over $\pm 5\text{-m}$. The bottom plot shows has a Tukey window applied along the beam length to partially emulate source directivity which significantly reduces the measured oscillations.	29

3.7	Spherical acoustic wave measurement test.	30
3.8	Comparison of measured wavefront to simulated ones for the highest-amplitude speaker excitation at each frequency.	33
3.9	Deformable mesh for calculating the acoustic modes in the circular to square transitions at three stages.	34
3.10	CAD model of the University of Notre Dame Whitefield wind-tunnel. The specifications of the tunnel at the numbered cross-sections are shown in Table 3.3.	38
3.11	Wind-tunnel discretization at a Mach number of 0.6. The solid lines in the sound transmission plots represent the transmitted pressure ratio while the dotted lines represent the reflected pressure ratio.	39
3.12	Cross-sectional slices of the acoustic field through the circle to square transition for the acoustic waves traveling upstream. Left side are the waves traveling from the fan at a phase of 0-radians and the right side at a phase of $\pi/2$ -radians. The top plots are the fan acoustic field, the middle plots are halfway through the transition, and the bottom plots are just into the square duct.	40
3.13	Cross-sectional acoustic field slices in the center of the test-section at various initial phase angles.	41
3.14	The real component of the acoustic mode coefficients making up the upstream-traveling acoustic field in the middle of the test-section as a function of the initial phase angle.	42
3.15	The real component of the acoustic mode coefficients making up the downstream-traveling acoustic field in the middle of the test-section as a function of the initial phase angle.	43
3.16	Comparison of a measured optical wavefront and a simulated one passing through the estimated acoustic field.	44
4.1	Multidimensional spectral estimation plot example and comparison to traditional power spectrum measurements. A single row of an optical wavefront measurement was used in this example. The top plot shows the typical power spectrum averaged over the entire row of data. Both the middle and bottom plots show the multidimensional spectrum plot with the y-axis as spacial-frequency in the middle and velocity in the bottom assuming $u = f/\xi_x$	46
4.2	Horizontal moving optical disturbances comparison. The top plot shows a slice of the three-dimensional spectrum focusing on the plane waves that are traveling in the horizontal direction. The middle plot is a recreation of the two-dimensional spectrum by integrating through the vertical spatial-frequencies. The bottom plot is the two-dimensional spectrum.	52
4.3	Recovery of time-based power spectrum from two-dimensional spectral estimate. . .	54
4.4	Horizontal and vertical moving optical disturbances. This is the same data as presented in Figure 4.1 but after calculating the full three-dimensional spectral estimate. These optical disturbances are plane waves that are traveling solely in their respective directions.	55
4.5	Temporal-frequency slices at 5 and 10 kHz with the various horizontal velocities labeled.	56
4.6	Three-dimensional view of the multidimensional spectral plot showing an isosurface at a power of $10^{-14} \mu\text{m}^2/\text{Hz}/\text{m}^{-1}/\text{m}^{-1}$. The isosurface encompasses 99.9% of the power of the wavefront.	59
4.7	Multidimensional spectral estimate isosurfaces as the Mach number increased from 0.3 to 0.5. The isosurfaces are all shown at a power of $10^{-14} \mu\text{m}^2/\text{Hz}/\text{m}^{-1}/\text{m}^{-1}$ and all encompass 99.9% of the wavefront power.	60

4.8	Multidimensional spectral estimate isosurfaces of different viewing angles through the test section at a Mach number of 0.5. The isosurfaces are all shown at a power of $10^{-14} \mu\text{m}^2/\text{Hz}/\text{m}^{-1}/\text{m}^{-1}$ and all encompass 99.9% of the wavefront power.	61
4.9	Multidimensional spectral estimate slices at various temporal-frequencies.	63
4.10	Acoustic duct mode lines showing the spatial-frequency location as a function of temporal-frequency, Mach number, and mode number.	65
4.11	Artificially increased temporal sample rate using a dispersion analysis. The black box represents original dispersion plot.	66
5.1	Multidimensional spectral estimation that the synthetic wavefront is based on.	71
5.2	Synthetic wavefront input dispersion plot of an aero-optical signal and various signal corruption components. The aero-optical signal is shown in red, the stationary modes in blue, duct acoustics in magenta, blade-passing frequency related corruption in green, slowly varying mean-lensing in yellow, and background in cyan.	72
5.3	Sample frames from the synthetic wavefront with the total wavefront signal on top and the aero-optical only signal bottom. Flow is from right to left.	79
5.4	Synthetic wavefront output dispersion plot of an aero-optical signal and various signal corruption components.	80
6.1	The <i>opdrms</i> of high-pass temporal filtered wavefronts relative to the <i>opdrms</i> of the aero-optical only unfiltered wavefront. Power spectra of both of the simulated wavefront versions.	84
6.2	Measured wavefronts filtered at the blade-passing frequency (532 ± 10 Hz). The left column is band-stop filtered while the right is band-pass filtered.	86
6.3	Multidimensional spectral isosurface of the synthetic wavefront with a downstream filter in place.	88
6.4	Multidimensional spectral isosurface of the synthetic wavefront with a low-pass velocity-filter in place.	90
6.5	Boundary layer velocity measurement of the synthetic wavefront using a combination of a low-pass velocity filter and a high-pass radial frequency filter. The maximum value at $u_{BL}/U = 0.8$ corresponds with the actual value used in the creation of the synthetic wavefront.	91
6.6	Velocity low-pass filter used to determine the mean disturbance velocity of measured data presented in Figure 4.6. The velocity in the x-direction was measured to be 207 m/s and -17 m/s in the y-direction.	92
6.7	Baseline spectrum estimation. The top left plot shows the unfiltered multidimensional spectrum and the baseline spectrum on the top right. The green line in each of these plots represents the location at which the spectra in the bottom plot is shown.	94
7.1	Schematic of the SPOD algorithm (taken from [50]). The numbers in parentheses denote the equations used.	99
7.2	The locations of some of the additional sensors used in the LSE-SPOD filtering. The sensors are labeled with the sensor numbers, see Table 7.1.	102
7.3	CAD drawing view of the inside of the test-section with some of the sensor locations labeled. Flow is from left to right. The numbers in the circles are the sensor numbers on the model side of the test-section. The numbers in the square are the sensor numbers opposite of the model side. The dashed line represents the optics window opposite of the model for the beam angle of 90° . The window was moved up and downstream depending on the beam angle.	102

7.4	Power-spectra of the additional sensor measurements at the three Mach numbers tested. The x-axis is in Strouhal number per characteristic length (St/l).	105
7.5	A multidimensional power spectrum of an unfiltered wavefront and the same wavefront filtered with the LSE-SPOD method using all 16 additional microphone or accelerometer measurements.	106
7.6	A multidimensional power spectrum of an unfiltered wavefront and the same wavefront filtered with the LSE-MSPOD method using all 16 additional microphone or accelerometer measurements.	107

TABLES

3.1	Curve fit values for Figure 3.6 and Equation 3.14	31
3.2	Comparison of microphone and wavefront computation of $ A_0 $	32
3.3	Wind-tunnel cross-section specifications	37
5.1	Values used in the construction of the multidimensional spectrum for the boundary layer signal	73
5.2	Values used in the construction of the multidimensional spectrum for the signal of the stationary modes	74
5.3	Values used in the construction of the multidimensional spectrum for the blade-passing frequency disturbance	75
5.4	Values used in the construction of the multidimensional spectrum for the acoustic cone disturbance	76
5.5	Values used in the construction of the multidimensional spectrum for the mean-lensing disturbance	77
7.1	Additional sensors used the the LSE-SPOD filtering.	103
7.2	OPD _{RMS} (μm) comparison of using different combinations of additional sensor information in the LSE-MSPOD filtering process.	108

SYMBOLS

Ap	Aperture size - Typically diameter
I	Actual on target intensity
I_0	Diffraction-limited intensity
k	Wavenumber ($k = 2\pi/\lambda$)
n	Index of refraction
OPD	Optical path difference
OPD_{RMS}	Time-averaged spatial OPD root-mean-square
$\text{OPD}_{\text{RMS}}(t)$	Spatial OPD root-mean-square as a function of time
SR	Strehl ratio ($\text{SR} = I/I_0$)
Greek	
δ	Boundary layer thickness
$\langle \theta^2 \rangle$	Mean-squared of the fluctuating deflection angle

ACKNOWLEDGMENTS

CHAPTER 1

INTRODUCTION

There have been two major attempts to field a directed-energy system aboard an aircraft to date [28]. The first was the Airborne Laser Laboratory (ALL) which took place in the late 1970's and early 1980's which used a CO₂ laser with a wavelength of 10.6-μm. The second was the Airborne Laser (ABL) program which operated in the 2000's and used a COIL laser at 1.315-μm. Airborne optical systems like ALL and ABL have to deal with a phenomenon known as “aero-optics,” which refers to optical distortions caused by compressible aero-dynamic flow features that pass through the outgoing beam. These optical distortions were first noticed due to image degradation in wind tunnel measurements in the 1950's [56] as well as in photo-reconnaissance missions in the 1960's [30].

The peak on-target irradiance of a beam passing through an optical disturbance, I , divided by the diffraction-limited performance, I_0 , is known as the Strehl ratio [34], SR,

$$\text{SR} = \frac{I}{I_0}. \quad (1.1)$$

The diffraction-limited performance is the beam intensity that would exist on the same target if not for the optical disturbance. The Airborne Laser Laboratory had an estimated Strehl ratio of 95%[28] so that the “aero-optics problem” effectively did not apply for this case. Following the Airborne Laser Laboratory program there was a desire to move toward shorter wavelengths in order to take advantage of improved diffraction-limited performance, leading to a smaller-diameter focused spot on target with a higher irradiance I_0 : [27],

$$\frac{I_0}{P} = \frac{1}{\pi} \left(\frac{Ap}{\lambda z} \right)^2, \quad (1.2)$$

where P is the laser output power, Ap is the aperture size, and z is the propagation distance. The improvement in diffraction-limited performance as the laser wavelength is decreased is shown in Figure 1.1. By only changing the laser source from a 10-μm to 1-μm wavelength the diffraction-limited performance can be increased 100 times.

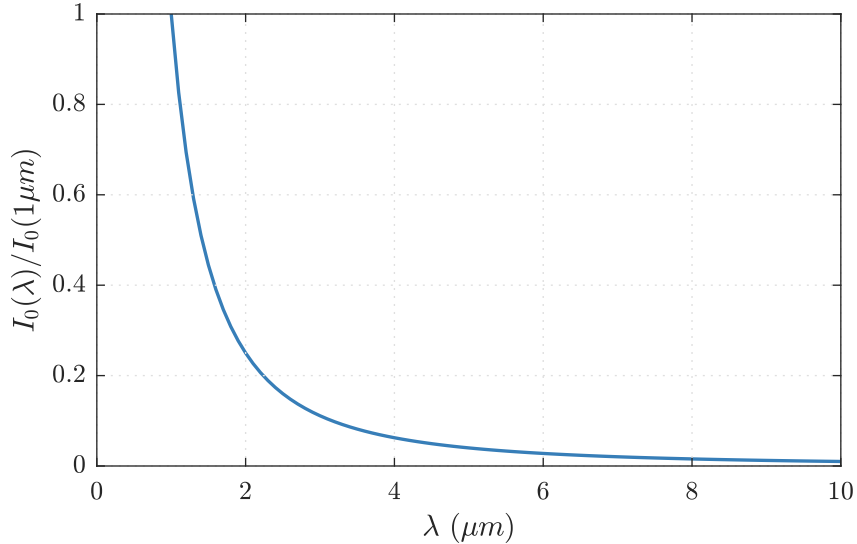


Figure 1.1. Diffraction-limited far-field intensity of a beam normalized by the performance at 1-μm.

Aero-optical issues start to become important as the wavelength is decreased as is evident from the Maréchal approximation [35] which relates the Strehl ratio to wavelength,

$$\text{SR} \approx \exp \left\{ - \left[\frac{2\pi \text{OPD}_{\text{RMS}}}{\lambda} \right]^2 \right\}, \quad (1.3)$$

where OPD_{RMS} is the spatial root-mean-square of the optical path difference over the aperture and is a way to quantify the optical disturbance as will be discussed further in Chapter 2. As stated above, the ALL had a Strehl ratio of 95%; however, if the ALL system's laser was swapped with another laser of a lower wavelength, the Strehl ratio would significantly decrease as shown by Figure 1.2. While going from 10 to 1-μm hypothetically results in a 100-fold increase in diffraction-limited performance, the actual on-target intensity that this hypothetical system obtains would be essentially zero due to the much larger effect that aero-optical aberrations have on the outgoing beam as the wavelength is reduced. This means that the aero-optical problem can no longer be ignored, which was recognized as one of the main developmental risks of the ABL program [14].

As the next generation of airborne directed-energy systems are developed some amount of ground testing of those systems will need to occur. In order to understand the aero-optical environment that these systems will experience in the air, wind tunnel tests will need to be employed. These tests are cheaper to perform than, for example, flight testing, and allow for quicker iteration of design

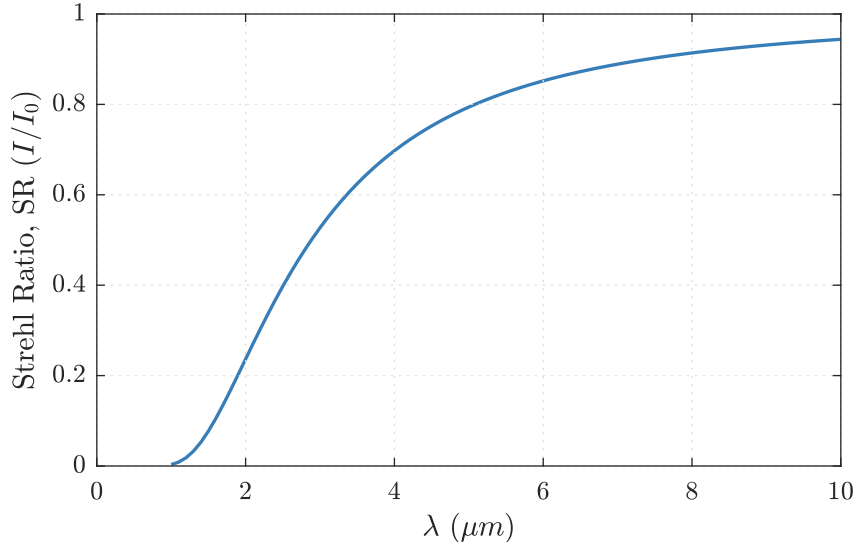


Figure 1.2. Strehl ratio due to the OPD_{RMS} of the Airborne Laser Laboratory (ALL) at various laser wavelengths. ALL had an estimated Strehl ratio of 95% with its 10.6- μm laser.

parameters. However, as will be described in further detail in Chapter 2, wind-tunnel measurements of aero-optical effects typically require passing a test beam into and through the test-section, so that the test beam is susceptible to acquiring additional optical contamination including but not limited to the boundary layer present on the wall and the acoustic environment generated by the wind tunnel fan [20]. Note that it is common in signal-processing terminology to use the word “noise” to describe unwanted interference that appears in addition to the “signal” that is the objective of the measurement; however, in this dissertation, the word “contamination” is used to describe any optical noise sources that are unrelated to the aero-optical signal, in order to avoid confusion with use of the word “noise” to describe acoustic noise which, as will be shown, is also a source of optical contamination.

Assuming that the optical disturbances from aero-optical effects are statistically independent from the contaminating optical disturbances from the testing environment, we can estimate the total optical disturbance as

$$OPD_{RMS,TOTAL}^2 = OPD_{RMS,MODEL}^2 + OPD_{RMS,ENVIRONMENT}^2. \quad (1.4)$$

As an example of the effect that optical contamination may have on system design, Figure 1.3 illustrates a hypothetical iterative design process, where the design objective is to obtain a design that

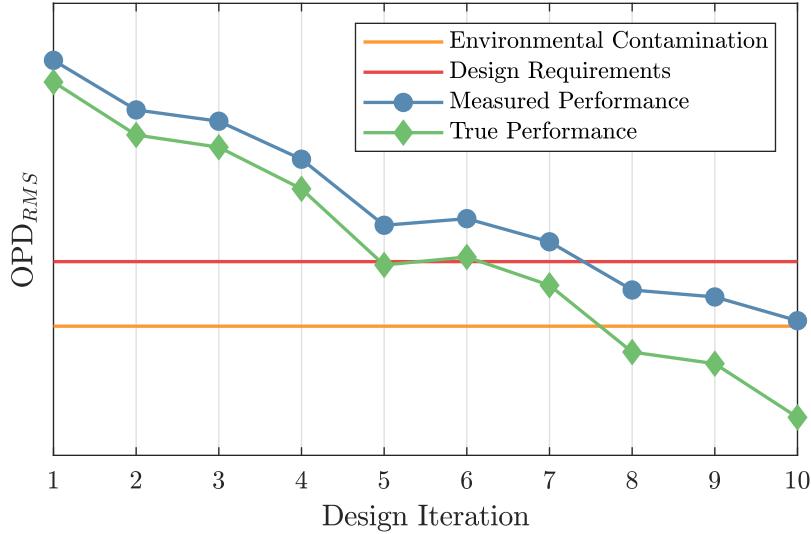


Figure 1.3. Hypothetical iterative design process of an airborne directed-energy system. The required performance level is shown by the red line and the testing environment's contamination is shown by the orange line.

meets a required level of performance shown in red, in the presence of a level of environmental optical contamination shown in orange. The design process was simulated by an initial aero-optical OPD_{RMS} shown on the left of the plot, and the improvement in system performance achieved with each design iteration was simulated as a nearly linear reduction in OPD_{RMS} combined with 15% random variation. If only the measured data, that is, including the effect of environmental contamination using Equation 1.4, is used to assess the system's performance then three additional design iterations are needed to achieve a usable design, which can add significantly to the development time and costs. If the environmental contamination is greater than the design requirement, the measured performance will never reach the required performance criteria. However, if the environmental contamination can be estimated, mitigated and/or removed, then the measured performance is a more accurate evaluation of the true aero-optical performance, and design convergence can be achieved more quickly and with more accurate results.

This dissertation will examine the environmental contamination of aero-optical measurements in wind tunnels, with a particular focus on the contamination due to acoustic noise within the wind tunnel. A review of the available literature and important concepts is given in Chapter 2. In Chapter 3, the optical disturbances caused by acoustic waves from simple plane and spherical waves are presented, leading to a process for estimating the acoustical environment within the test section of a wind tunnel. The strength of an spherical acoustic wave will be assessed with both microphone

and optical measurements. Multi-dimensional spectral techniques will be used to analyze optical wavefronts in Chapter 4 and to filter optical wavefronts in Chapter 6. These filtering techniques will contain some optical contamination particularly in regions where the various signal components interfere with one another. In order to further reduce the optical contamination, Chapter 7 will utilize additional sensor information from both microphones and accelerometers to remove some of the overlapping contamination to obtain a better picture of the actual optical performance of an airborne directed-energy system from ground test measurements.

CHAPTER 2

LITERATURE REVIEW

The literature review will consist of primarily two sections. The first section will examine aero-optics while the second will look at acoustics inside of ducts.

2.1 Aero-Optics

Optical communication and directed energy systems require a tightly focused beam on target in order to meet system performance objectives. The farfield performance of airborne optical systems can be degraded by the nearfield flow that becomes optically active at compressible flow speeds. “Aero-optics” is the study of the optical effect of these nearfield flow disturbances. Examples of important aero-optical flows that have been studied extensively include boundary layers [20, 55, 58], shear layers [15, 49], shock waves [28], and even tip vortices [46]. The effect of acoustic disturbances on aero-optical measurements has also been shown in both flight testing [13] and ground testing [10, 11].

In these optically active flows the index-of-refraction, n , varies locally as does the other fluid properties. Gladstone and Dale [18] found that the index-of-refraction is primarily a function of density with a loose dependence on the wavelength of light. Gladstone and Dale proposed a “specific refractive energy” now known as the Gladstone-Dale constant, K_{GD} ,

$$K_{GD} = \frac{n - 1}{\rho}. \quad (2.1)$$

For air the refractive index can be related to state quantities [57]

$$n - 1 = 77.6 \times 10^{-6} \frac{P}{T} \left(1 + \frac{7.53 \times 10^{-3}}{\lambda^2} \right), \quad (2.2)$$

where P is in mbar, T is in K, and λ is in μm . By combining this relationship with the ideal gas

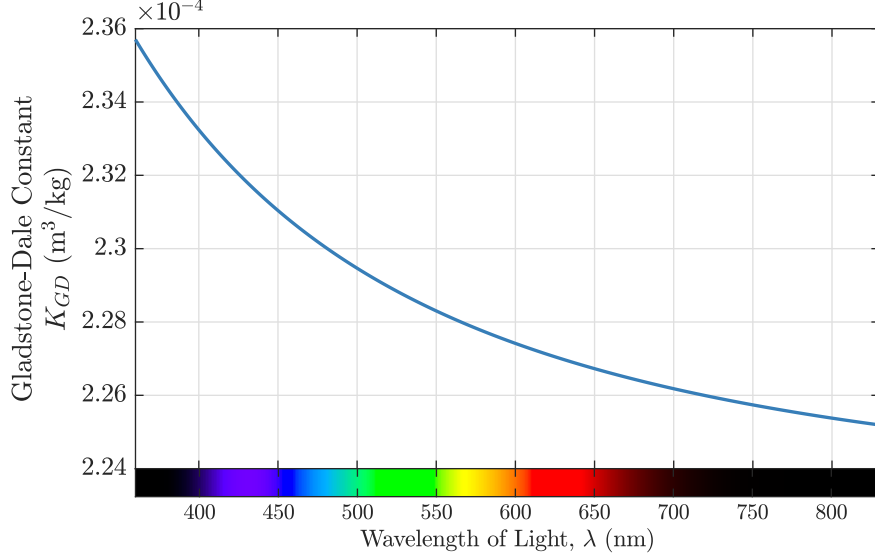


Figure 2.1. Gladstone-Dale constant for air over the visible wavelength range.

law, the Gladstone-Dale constant can be determined as a function of light wavelength,

$$K_{GD} = 2.23 \times 10^{-4} \left(1 + \frac{7.53 \times 10^{-3}}{\lambda_{\mu m}^2} \right) \left[\frac{m^3}{kg} \right]. \quad (2.3)$$

The Gladstone-Dale constant for air over the visible range is shown in Figure 2.1. While the value for K_{GD} does vary over the visible range, it is only a few percent, and many sources use an average value of $2.27 \times 10^{-4} \text{ m}^3/\text{kg}$ for the visible and near-infrared [26]. The Gladstone-Dale relationship is typically presented as

$$n = 1 + K_{GD}\rho \quad (2.4)$$

but when applied to situations where there are significant fluctuations in the flow an alternate form is often more useful

$$n' = K_{GD}\rho' \quad (2.5)$$

where ' denotes the quantity represents the fluctuating component ($n' = n - \bar{n}$).

When a beam with an initially planar wave front passes through a region of optical active flow its wave front aberrated. The optical path length (OPL) at any point in the beam can be obtained by integrating the index of refraction along the propagation of an optical ray [29].

$$\text{OPL}(x, y, t) = \int_{s_1}^{s_2} n(x, y, z, t) ds \quad (2.6)$$

The optical path difference (OPD), is then the spatially-averaged OPL over an aperture removed from the OPL.

$$\text{OPD}(x, y, t) = \text{OPL}(x, y, t) - \langle \text{OPL}(x, y, t) \rangle \quad (2.7)$$

When working with fluctuating components, the OPD can be calculated directly

$$\text{OPD}(x, y, t) = \int_{s_1}^{s_2} n'(x, y, z, t) ds. \quad (2.8)$$

When OPD is combined with the beam intensity profile, one can compute the farfield complex amplitude distribution using the Fraunhofer approximation [19].

$$U(x_0, y_0, t) \propto \iint_{Ap} \exp \left\{ \frac{2\pi j}{\lambda} \left[\text{OPD}(x_1, y_1, t) - \frac{(x_0 x_1 + y_0 y_1)}{z} \right] \right\} dx_1 dy_1 \quad (2.9)$$

where U is the complex amplitude, the subscripts 0 and 1 represent the coordinates of the farfield and nearfield respectively. The intensity can be computed from the complex amplitude via: $I = UU^*$. For cases in which optical aberrations are nonexistent (i.e. $\text{OPD}(x, y, t) = 0$), the farfield irradiance pattern that results from Equation 2.9 is caused entirely by diffraction from the optical aperture, and is referred to as the “diffraction-limited” irradiance pattern. For a beam with a flat wave front and circular aperture, the farfield irradiance pattern is the Airy’s disk, and the peak irradiance at the center of the disk, I_0 , is the maximum irradiance that can be achieved by the optical system:

$$I_0 = \left(\frac{kAp^2}{8z} \right)^2 \quad (2.10)$$

where k is the wavenumber ($k = 2\pi/\lambda$), Ap is the aperture diameter, and z is the distance from the aperture. In the presence of aero-optical aberrations, $\text{OPD}(x, y, t)$ is non-zero, and the farfield irradiance pattern in this case tends to be more spread out and diffuse than the diffraction-limited case; furthermore, the beam may be shifted off target by optical tip/tilt imposed by the aberrations.

The Strehl ratio (SR), is the ratio of intensity on target (I) to the diffraction-limited on target intensity (I_0):

$$\text{SR} = \frac{I}{I_0} \quad (2.11)$$

The Strehl ratio can be computed accurately by applying Equation 2.9 twice, once for the diffraction-limited case to obtain I_0 , and a second time with the OPD field due to aero-optical aberrations included to obtain I . The farfield performance, can also be estimated via the Maréchal approximation:

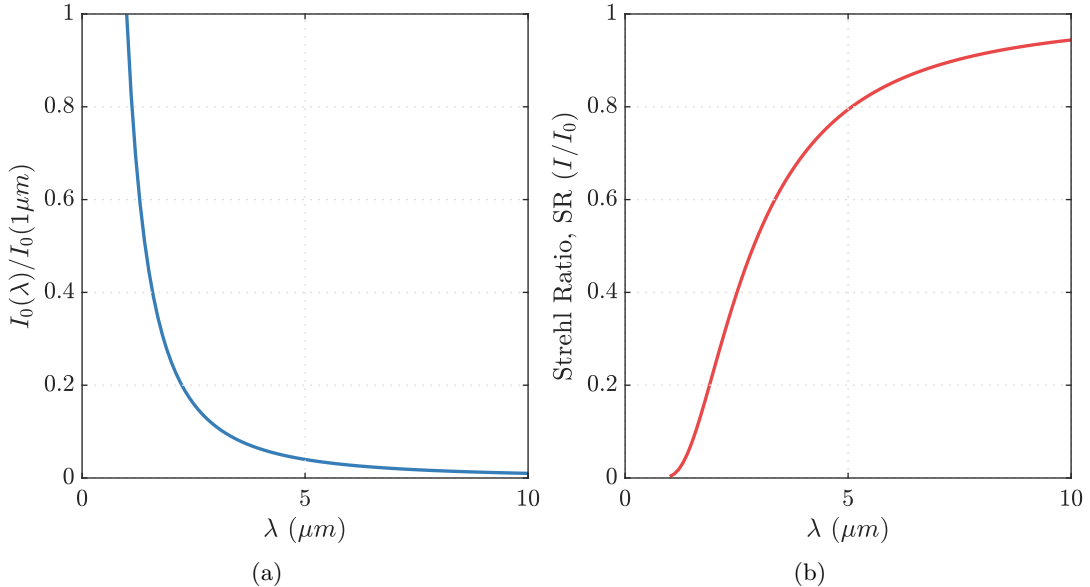


Figure 2.2. (a) Diffraction limited on target intensity as a function of wavelength normalized by the value at $\lambda = 1 \mu m$. (b) Strehl ratio as a function of wavelength for an aberration that gives SR = 0.95 at $\lambda = 10.6 \mu m$.

$$SR(t) \equiv \frac{I(t)}{I_0} \approx \exp \left\{ - \left[\frac{2\pi OPD_{RMS}(t)}{\lambda} \right]^2 \right\} \quad (2.12)$$

where OPD_{RMS} is the spatial rms of the wave front and λ is the wavelength of the beam. Equation 2.12 shows a key relationship between OPD, wavelength, and the farfield performance, plotted in Figure 2.2b. On the other hand, Equation 2.10 shows that the diffraction-limited farfield irradiance increases as the wavelength is shortened, plotted in Figure 2.2a. Together, Figure 2.2a and 2.2b show that as modern optical systems move to shorter wavelengths to increase I_0 , aero-optical aberrations cause a much more serious degradation of the Strehl ratio, illustrating why aero-optical considerations are critical in the development of any airborne optical system.

Figure 2.3 shows the OPD_{RMS} necessary to achieve various Strehl ratios over a range of wavelengths. As the wavelength of light decreases the required OPD_{RMS} decreases linearly for a fixed Strehl ratio.

2.1.1 Typical Optical Wavefront Measurement System

A diagram of a typical double-pass Shack-Hartmann wavefront front sensor setup is shown in Figure 2.4. The system starts with the laser in the bottom of the plot, which is then expanded

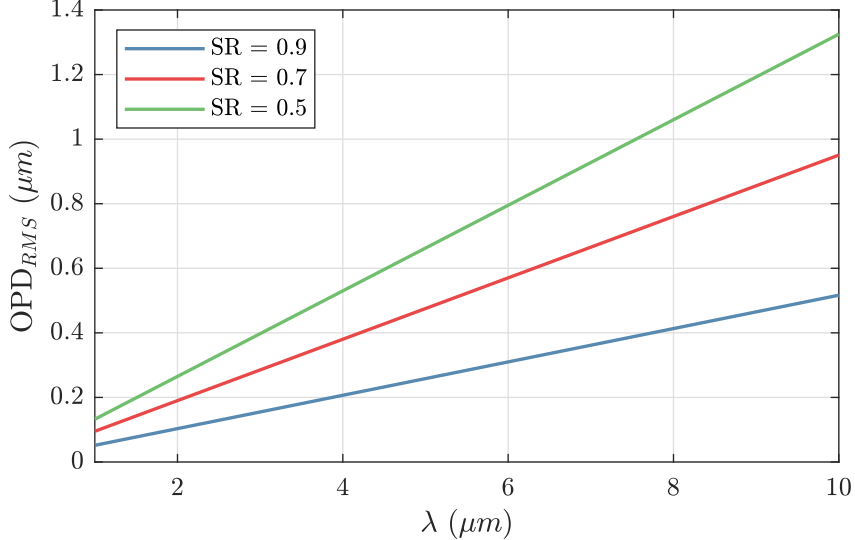


Figure 2.3. OPD_{RMS} values necessary to obtain Strehl ratios of 0.9, 0.7, and 0.5 over a range of wavelengths.

to a larger diameter. The beam expander used in this research increased the diameter of the beam to approximately 1-inch. The larger diameter beam then passes through a beam splitter where half of the intensity is discarded and the other half proceeds to the primary telescope. The primary telescope expands the beam to the desired size for the first passage through the measurement region. For measurements made in a wind-tunnel, the beam angle, γ , is typically defined based on the flow direction [20] with 0° being looking straight into the flow and 180° looking downstream.

A large mirror is used to return the beam along the same path for a second passage through the measurement region where the primary telescope shrinks the beam back down to a 1-inch diameter. On the return path, the beam splitter sends half of the intensity back through the beam expander to the laser and half to the reimaging telescope. The reimaging telescope serves two purposes, the first is to create an image plane for the wavefront sensor at the desired object plane location, typically the return mirror for a double-pass setup. The second is to reduce the beam diameter for the wavefront sensor to a size that depends on the resolution and frame rate needed for a measurement.

The Shack-Hartmann wavefront sensor is comprised of a lenslet array and a camera [17]. A diagram of how the wavefront sensor functions can be seen in Figure 2.5. The perturbed wavefront is represented by the black lines on the top with the measurable component shown in red which is the mean slope over each lenslet. By measuring the displacement, [41], of the focal dot from its normal position, the average slope, θ_x and θ_y , of the wavefront over a lenslet can be

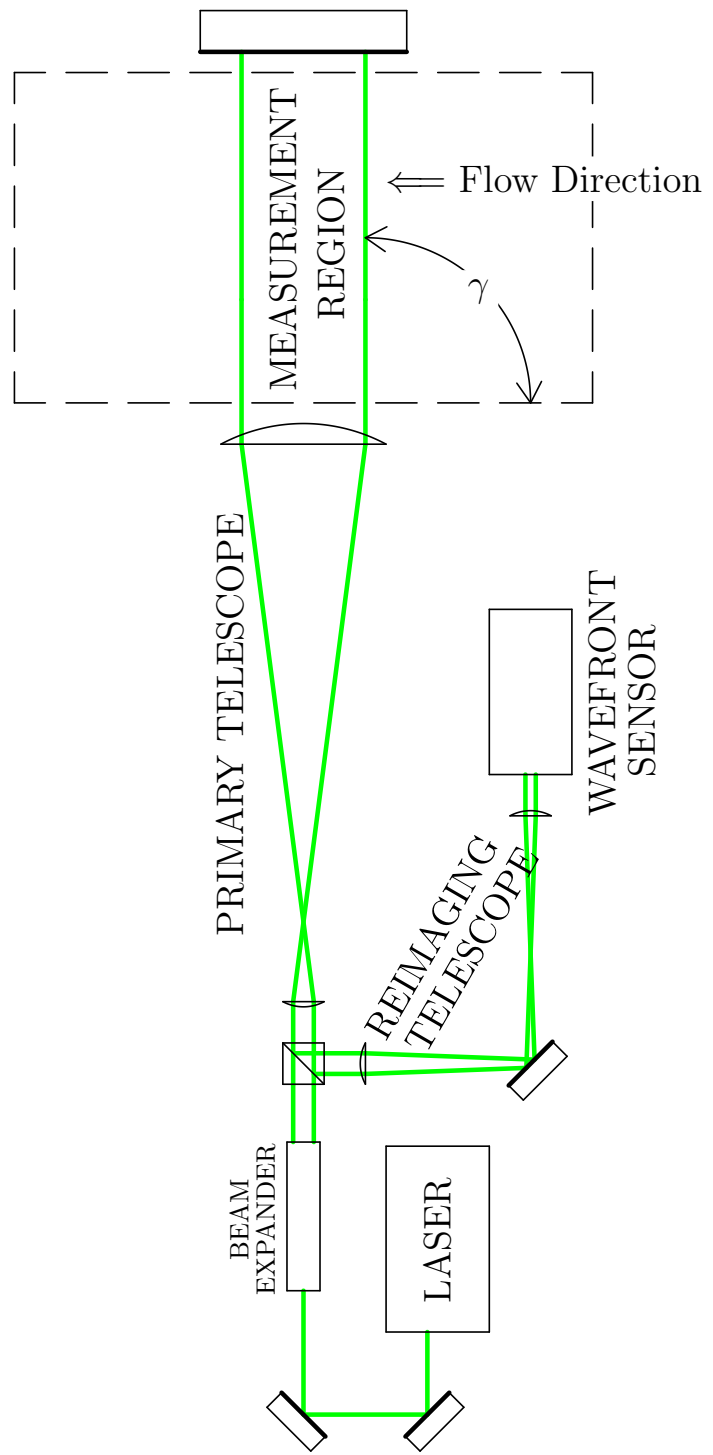


Figure 2.4. Typical double-pass optical wavefront measurement setup.

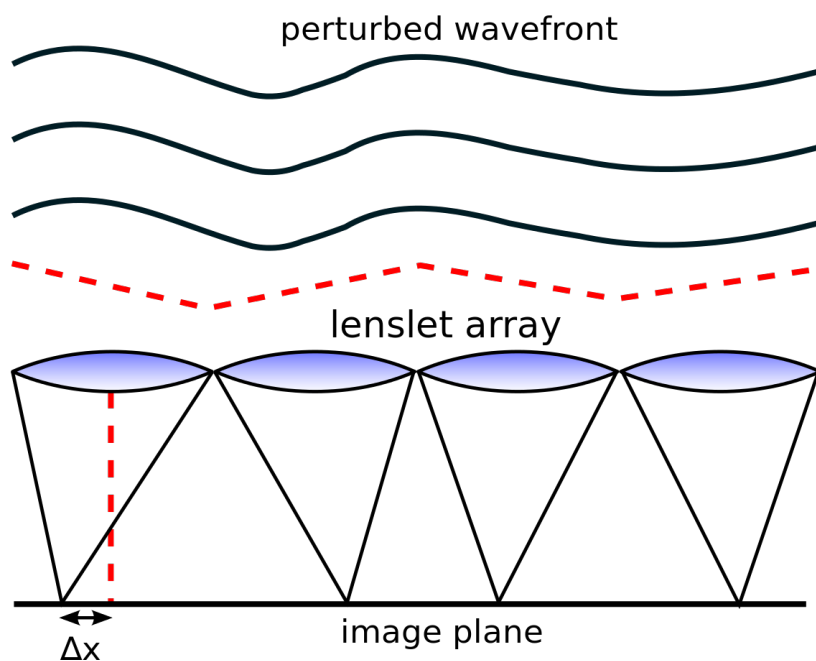


Figure 2.5. Diagram of a Shack-Hartmann wavefront sensor comprised of four lenslets. The black line represents the perturbed wavefront and the red line the mean slope over each lenslet. The focal point of the wavefront is shifted by Δx from the center-line of the lenslet based on the mean slope of the wavefront. [1]

measured,

$$\theta_x = \tan^{-1} \frac{\Delta x}{f} \approx \frac{\Delta x}{f}, \quad (2.13)$$

where f is the focal length of the lenslet. With an array of gradient data, the optical path difference at each lenslet can be calculated using a number of integration methods [23].

2.2 Acoustics

2.2.1 Basic Acoustics

Starting with the conservation of mass,

$$\frac{\partial \rho}{\partial t} + \nabla \cdot (\rho \mathbf{u}) = 0, \quad (2.14)$$

and separating the density into a time-averaged (ρ_0) and fluctuating portion (ρ'), $\rho = \rho_0 + \rho'$. The fluctuating conservation of mass equation is obtained by separating the density ($\rho = \rho_0 + \rho'$) into a temporally averaged density, ρ_0 , and a

$$\frac{\mathbf{D}\rho'}{\mathbf{Dt}} + \nabla \cdot (\rho_0 \mathbf{u}) = 0 \quad (2.15)$$

For acoustics waves of frequency less than 10^9 Hz the compression of the fluid can be assumed to be adiabatic [38].

$$\left. \frac{\partial p}{\partial \rho} \right|_s = c_0^2 \quad (2.16)$$

2.2.2 Duct Acoustics

Acoustic waves are often enclosed inside of some sort of structure. This section will look at acoustics when confined to a duct in which the acoustic waves primarily travel along one-axis and have walls confining the acoustics along the other two axes as is the case inside of a wind tunnel. Figure 2.6 shows the diagram used for deriving the acoustic properties inside of a constant area duct.

This derivation is primarily influenced from Munjal [40] along with Jacobsen and Juhl [24]. The primary assumption used in this derivation is that the duct is of constant cross-section. This means that all mean quantities (ρ_0 , \mathbf{u}_0 , ...) a constant throughout space and time. Starting with the

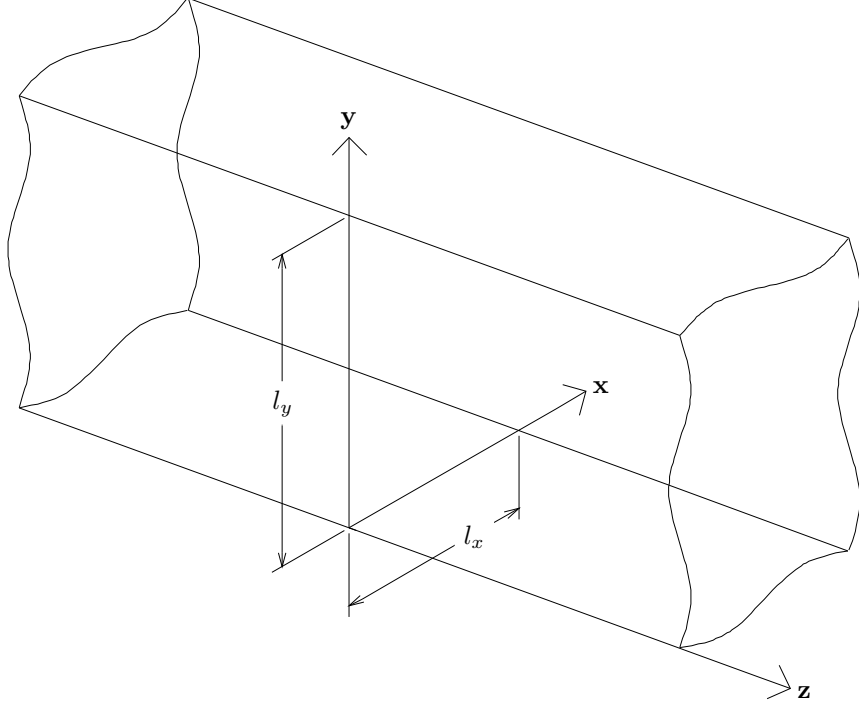


Figure 2.6. Duct with a rectangular cross-section.

linearized inviscid forms of the conservation of mass,

$$\frac{\mathbf{D}\rho}{\mathbf{Dt}} + \rho_0 \nabla \cdot \mathbf{u} = 0, \quad (2.17)$$

and conservation of momentum,

$$\rho_0 \frac{\mathbf{D}\mathbf{u}}{\mathbf{Dt}} + \nabla p = 0. \quad (2.18)$$

The definition of the speed of sound (Equation 2.16) is then substituted into Equation 2.17,

$$\frac{1}{c_0^2} \frac{\mathbf{D}p}{\mathbf{Dt}} + \rho_0 \nabla \cdot \mathbf{u} = 0, \quad (2.19)$$

where c_0 is the speed of sound at average fluid properties (ρ_0, p_0, T_0, \dots). Next the difference between the material derivative (\mathbf{D}/\mathbf{Dt}) of Equation 2.19 and the partial derivative ($\partial/\partial\mathbf{x}$) of Equation 2.18 with respect to space is taken which results in the convected 3-D wave equation,

$$\left(\frac{\mathbf{D}^2}{\mathbf{Dt}^2} - c_0^2 \nabla^2 \right) p = 0. \quad (2.20)$$

Expanding the material derivative and dividing by c_0^2 ,

$$\left(\frac{1}{c_0^2} \frac{\partial^2}{\partial t^2} + \frac{2\mathbf{M}}{c_0} \frac{\partial^2}{\partial t \partial \mathbf{x}} - (1 - \mathbf{M}^2) \nabla^2 \right) p = 0, \quad (2.21)$$

where $\mathbf{M} = \mathbf{u}_0/c_0$. By using the fact that $c_0 = \omega/k_0$, Equation 2.20 can be written in a more convenient form,

$$\left(\frac{1}{\omega^2} \frac{\partial^2}{\partial t^2} + \frac{2\mathbf{M}}{\omega k_0} \frac{\partial^2}{\partial t \partial \mathbf{x}} - \frac{1 - \mathbf{M}^2}{k_0^2} \nabla^2 \right) p = 0, \quad (2.22)$$

where ω is the angular frequency and k_0 is the total wavenumber.

At this point the pressure field is going to be written in a complex form and assumed to be separable in both time and space such that $\hat{p}(\mathbf{x}, t) = \hat{p}(x, y)\hat{p}(z)\hat{p}(t)$. The temporal solution is assumed to take the form

$$\hat{p}(t) = \exp \{j\omega t\}. \quad (2.23)$$

This results in the spatial component of the convecting wave equation

$$((1 - \mathbf{M}^2) \nabla^2 - 2jk_0 \mathbf{M} \nabla + k_0^2) \hat{p}(x, y)\hat{p}(z) = 0. \quad (2.24)$$

This can be further split into axial and cross-sectional components by splitting k_0 into components,

$$k_0 = \sqrt{k_{xy}^2 + k_z^2}, \quad (2.25)$$

and because the mean flow is only in the axial direction ($\mathbf{M} = M\hat{\mathbf{k}}$). The cross-sectional component is a typical Helmholtz equation

$$\left(\frac{\partial^2}{\partial x^2} + \frac{\partial^2}{\partial y^2} \right) \hat{p}_{xy}(x, y) + k_{xy}^2 \hat{p}(x, y) = 0, \quad (2.26)$$

whose solution,

$$\hat{p}(x, y) = \Psi_m(x, y), \quad (2.27)$$

is one of infinity many eigen-function solutions with discrete wavenumbers, k_m . The axial component of the convecting wave equation,

$$(1 - M^2) \frac{\partial^2 \hat{p}(z)}{\partial z^2} - 2jk_0 M \frac{\partial \hat{p}(z)}{\partial z} + k_z^2 \hat{p}(z) = 0, \quad (2.28)$$

retains the total wavenumber in second term which means its solution will depend on the cross-

sectional wavenumber value at cross-sectional mode. The solution to the axial convecting wave equation,

$$\hat{p}(z) = p_m^+ \exp \{-jk_{zm}^+ z\} + p_m^- \exp \{+jk_{zm}^- z\}, \quad (2.29)$$

has waves traveling in both directions with the axial wavenumber in each direction for a given mode

$$k_{zm}^\pm = \frac{\mp M k_0 + \sqrt{k_0^2 - (1 - M^2) k_m^2}}{1 - M^2}. \quad (2.30)$$

The solution for a three-dimensional acoustic wave in a duct with a constant but arbitrary cross-section in complex pressure is the combination of the component solutions presented in Equations 2.23, 2.27, and 2.29,

$$\hat{p}(x, y, z, t) = \Psi_m(x, y) (p_m^+ \exp \{-jk_{zm}^+ z\} + p_m^- \exp \{+jk_{zm}^- z\}) \exp \{j\omega t\}. \quad (2.31)$$

The two solutions for a plane wave ($\Psi_m = 1$, $k_m = 0$) traveling in a duct have a characteristic speed of $u \pm c_0$. Acoustic modes will travel indefinitely if $k_0^2 - (1 - M^2) k_m^2 > 0$ (the quantity inside of the square-root of Equation 2.30). This presents a frequency at which a given mode will cut-on,

$$f_{cuton} = \frac{c_0}{2\pi} \sqrt{(1 - M^2) k_m^2}. \quad (2.32)$$

Below this frequency, an acoustic mode will be exponentially attenuated as it travels through the duct.

2.2.2.1 Characteristic Equations of Cross-Sections

In order to determine the characteristic equations of an acoustic field within a cross-section the solution to Equation 2.26 needs to be determined. A typical boundary condition that is used in the solution of this 2-D Helmholtz equation is using the assumption that the walls are rigid.

$$\nabla p_{x,y}(x, y) \cdot \mathbf{n}_{wall} = 0 \quad (2.33)$$

This boundary condition results in the acoustic waves being perfectly reflected off of the duct walls. There are several known empirical solution sets of the characteristic equations for specific geometry with the rigid wall assumption.

Characteristic Functions for a Rectangular Duct

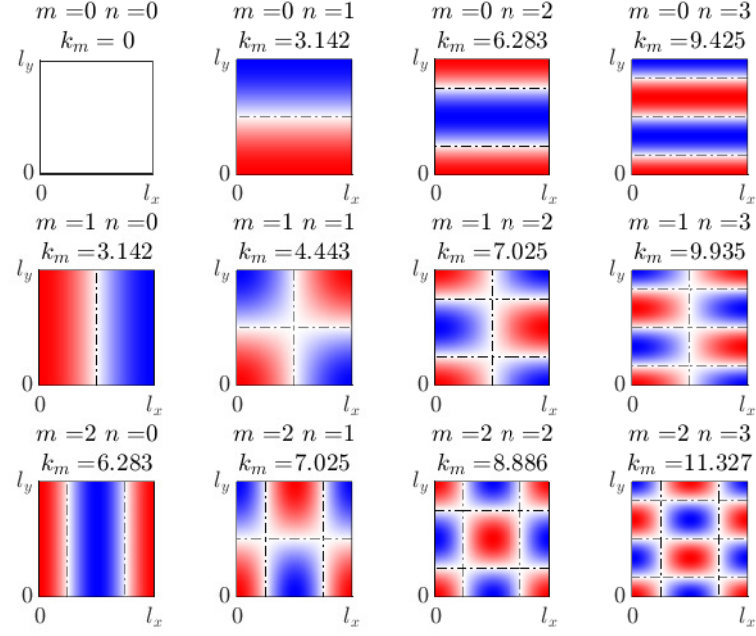


Figure 2.7. Characteristic solutions to Equation 2.26 with rigid wall in a rectangular cross-section where $m=0:2$ and $n=0:3$. Nodal lines are depicted by the dot-dash lines. The cross-sectional wave numbers, k_m , listed are for a duct of unit length and height.

The first of these solutions is for a rectangular cross-section,

$$\Psi_{m,n}(x, y) = \cos(k_x x) \cos(k_y y), \quad (2.34)$$

where the wave numbers along each axis are $k_x = m\pi/l_x$ and $k_y = n\pi/l_y$. The duct has a width of l_x and a height of l_y . The total cross-sectional wave number for use in determining the axial wave numbers is

$$k_m^2 = k_x^2 + k_y^2. \quad (2.35)$$

Figure 2.7 shows the characteristic functions when $m=0:2$ and $n=0:3$ for a rectangular cross-section of width of l_x and height of l_y . The lines depicted in the figure are nodal lines and represent locations where there is zero pressure fluctuations for that acoustic mode.

Characteristic Functions for a Circular Duct

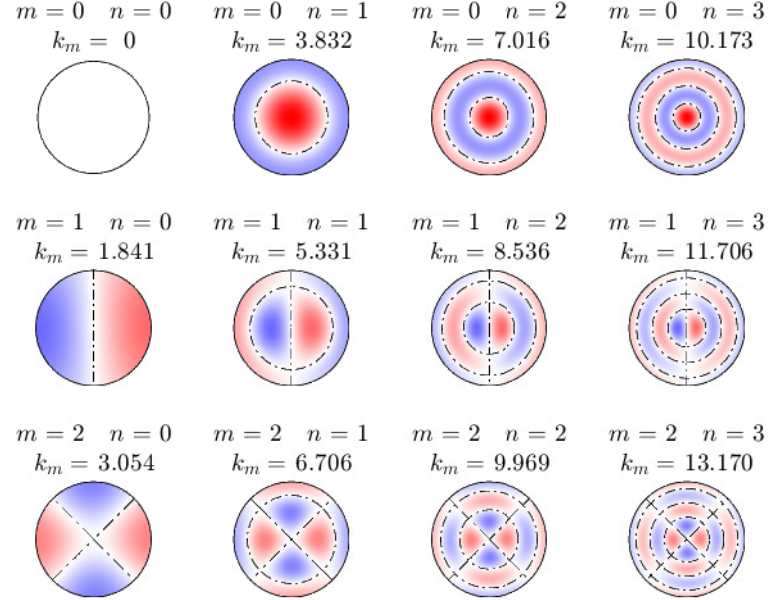


Figure 2.8. Characteristic solutions to Equation 2.26 with rigid wall in a circular cross-section where $m=0:2$ and $n=0:3$. Nodal lines are depicted by the dot-dash lines. The cross-sectional wave numbers, k_m , listed are for a duct of unit radius.

The second set of known empirical solutions is for a circular cross-section with radius R ,

$$\Psi_{m,n}(r, \theta) = J_m(k_{mn}r) \exp \{ \pm jm\theta \}, \quad (2.36)$$

where J_m is the m^{th} Bessel function of the first kind and the \pm indicates the direction of spin. If the left and right spin coefficients are equal in magnitude then a non-spinning mode is created. In order to satisfy the solid wall boundary condition $J'_m(k_{mn}R) = 0$ which determines a set of discrete values for the cross-sectional wave number at the n^{th} zero for the m^{th} Bessel function. Figure 2.8 shows the characteristic functions for a circular duct.

CHAPTER 3

AERO-OPTICAL AND ACOUSTICAL COUPLING

Acoustic waves are isentropic compression waves with the fluctuating pressure, p' , determining the strength of the wave. This fluctuating pressure is related to the sound pressure level, SPL by

$$\text{SPL} = 20 \log_{10} \left(\frac{p_{rms}}{p_0} \right) \quad (3.1)$$

where p_{rms} is the root mean square of the pressure fluctuation, and p_0 is the reference pressure (20 μPa for air). The pressure fluctuations can be related to the density fluctuations via the definition of the speed of sound:

$$c_0^2 = \left(\frac{\partial p}{\partial \rho} \right)_s = \frac{p'}{\rho'} \quad (3.2)$$

where c_0 is the speed of sound at mean fluid properties and the subscript s denotes constant entropy. It can be shown by combining Equations 2.5 and 2.7 that the fluctuating density can be related to the OPD,

$$\text{OPD} = K_{GD} \int_{s_1}^{s_2} \rho' ds. \quad (3.3)$$

This can be combined with Equation 3.2,

$$\text{OPD} = \frac{K_{GD}}{c_0^2} \int_{s_1}^{s_2} p' ds, \quad (3.4)$$

to provide a way of computing the optical path difference of a sound pressure field.

3.1 Simulating an Optical Wavefront Measurement from an Acoustic Field Function

The following analysis is presented for the case of a measurement field subject to acoustic excitation at a discrete frequency. Parameter values at each point in the field oscillate at the frequency of the acoustic field, with a magnitude and phase relationship to the acoustic field that can be represented by complex notation and that depends on the physics of the interaction with the acoustic field.

The effect of a complex acoustic pressure field on an optical wavefront can be simulated by applying Equation 3.4. To accomplish this, two separate coordinate systems will need to be defined. The first is the beam coordinate system, \mathbf{x}_B , that will have a measurement aperture, which is typically circular, defined in the xy-plane and assuming the beam propagates in the z-direction. The second is the acoustic coordinate system, \mathbf{x}_A , that will be defined based on the source location or the geometry that the acoustic waves are propagating through. A function representing the transformation from one coordinate system to the other can be defined as

$$\mathbf{x}_A = R\mathbf{x}_B + T, \quad (3.5)$$

where R is a matrix which represents the rotation and T is a vector that represents the translation.

The important parameters for defining the aperture on which the beam coordinate system is based are the aperture size, Ap , and the spatial discretization which, if the beam is measured using a Shack-Hartmann wavefront sensor, is the number of lenslets or sub-apertures in the wavefront sensor, $N_{lenslets}$. Assuming that the aperture is either circular or square and the lenslet size and sub-aperture size is approximately $Ap/N_{lenslets}$, the x locations of the center of the sub-apertures go from $-Ap/2(1 - 1/N_{lenslets})$ to $Ap/2(1 - 1/N_{lenslets})$ by steps of $Ap/N_{lenslets}$ with the y locations having the same values. This gives a matrix representing both x_{Ap} and y_{Ap} that is $N_{lenslets}$ by $N_{lenslets}$. For the purpose of removing piston, tip, and tilt and creating a mask that represents the beam aperture, the radial coordinates, ρ_{Ap} and θ_{Ap} , of the aperture should also be calculated. A circular beam will have a mask defined by,

$$Mask_{Ap} = \begin{cases} 1, & \text{if } \rho_{Ap} \leq Ap/2 \\ 0, & \text{otherwise.} \end{cases} \quad (3.6)$$

The beam coordinate frame is the aperture coordinates extruded in the z-direction over the range of desired z-values.

After the beam coordinates are transformed into the acoustic coordinates using Equation 3.5, the complex pressure field, $\hat{p}(x, y, z, t)$ can be calculated at the points that are within the optical beam. If the pressure field is separable into spatial and temporal components, then the integration along the beam length only needs to be done once for each temporal frequency,

$$\widehat{\text{OPD}}(x, y) = \frac{K_{GD}}{c_0^2} \int_{z_1}^{z_2} \hat{p}(x, y, z)_{Ap} dz, \quad (3.7)$$

where $\widehat{\text{OPD}}(x, y)$ is the complex optical path difference as measured in the aperture plane. If a complex density field is known instead, than Equation 3.24 becomes

$$\widehat{\text{OPD}}(x, y) = K_{GD} \int_{z_1}^{z_2} \hat{\rho}(x, y, z)_{Ap} dz. \quad (3.8)$$

For the purposes of calculating time-averaged optical properties of simulated beam passing through a known complex pressure or density field a phase vector was defined, $\phi = [0, 2\pi)$. The measurable component as a function of phase is

$$\text{OPD}(x, y, \phi) = \text{REAL} \left[\widehat{\text{OPD}}(x, y) \exp\{-j\phi\} \right], \quad (3.9)$$

or as a function of time for all temporal frequencies,

$$\text{OPD}(x, y, t) = \text{REAL} \left[\sum \widehat{\text{OPD}}(x, y) \exp\{-j\omega t\} \right], \quad (3.10)$$

where there is a separate $\widehat{\text{OPD}}(x, y)$ computed for each temporal frequency. One of the more important parameters that can be calculated from OPD is the spatial RMS, OPD_{RMS} , which is calculated at each time or phase step at the points where the aperture mask equals one.

3.2 Simple Examples of Acoustic-Optical Coupling

Two basic acoustic pressure fields will be numerically examined for their optical properties. The first will be a planar acoustic wave that will be numerically simulated over a variety of conditions. The second will be a spherical acoustic wave that will be both numerically simulated and validated experimentally.

3.2.1 Planar Acoustic Waves

A planar wave is the simplest solution to the wave equation and varies only in time and the direction of travel. A planar wave can be calculated from the set of solutions for duct acoustics, Equation 2.31, given that $\Psi_m(x, y) = 1$,

$$\hat{p}(z, t) = p_m \exp \left\{ j(\omega t \mp k_{zm}^{\pm} z) \right\}. \quad (3.11)$$

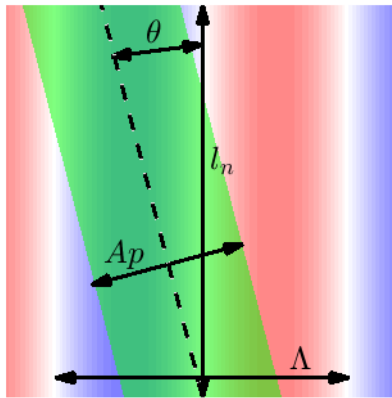


Figure 3.1. General geometry for various sample calculations for showing the acoustic-optical coupling effect.

This section will show the effect that acoustic waves have on the optical wavefront of a planar wave with the general geometry shown in Figure 3.1. For the following example, l_n is the width of the acoustic disturbance (for example, the width of the wind tunnel), θ is the angle between the planar acoustic wave and the beam direction, A_p is the aperture diameter of the beam, and Λ is the wavelength of the acoustic wave.

Figure 3.2 shows the time averaged OPD_{RMS} per meter of beam propagation when the beam path is parallel ($\theta = 0$) to the peaks and troughs of the planar acoustic wave as SPL is varied. As the sound pressure level increases the time averaged OPD_{RMS} also increases and can easily reach the point of being a significant factor in the measured optical disturbance. There is little difference between 0.1 and $1 \Lambda/A_p$, but as the wavelength gets much larger compared to the beam diameter, then the optical effect of the noise is greatly reduced, this effect is known as “aperture filtering.” Aperture filtering accounts for the fact that an aperture that is smaller than the wavelength of the optical disturbance only passes a portion of that optical disturbance, so that the measured OPD_{RMS} is reduced [54].

The effect of aperture filtering is more clearly shown in Figure 3.3. As the Λ/A_p ratio increases from 0.1, time-averaged OPD_{RMS} remains fairly constant until it starts to drop around Λ/A_p of 0.7 and starts to asymptotically approach zero which it basically reaches by Λ/A_p of 10. Figure 3.3 also shows the effect of changing the beam angle, θ , through the acoustic field. For nonzero θ , the beam encounters alternating high and low index of refraction as it passes through the test

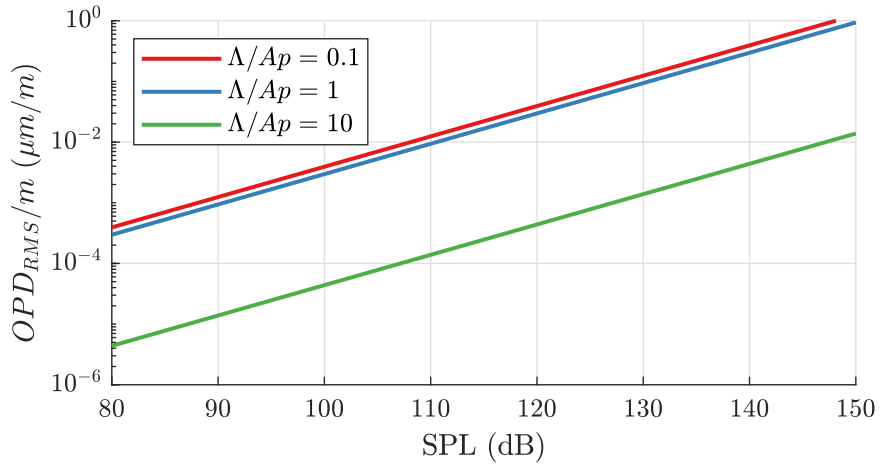


Figure 3.2. Theoretical time-averaged OPD_{RMS} per meter of beam propagation as a function of sound pressure level, SPL, for several Λ/Ap ratios and $\theta = 0$.

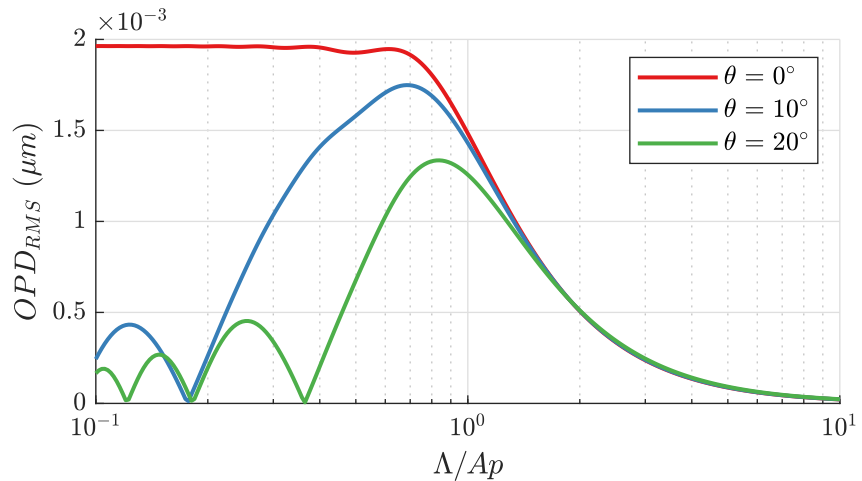


Figure 3.3. Theoretical time-averaged OPD_{RMS} for a rms sound pressure of 1 Pa (SPL of 94 dB), l_n of 1 m, and various angles and Λ/Ap ratios.

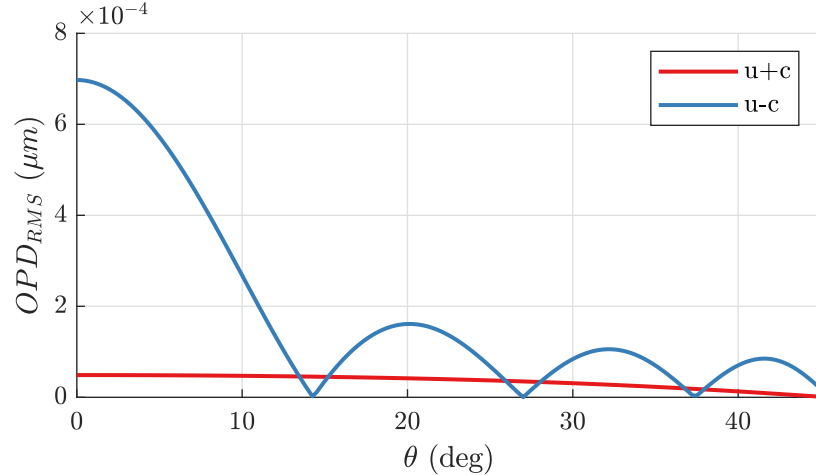


Figure 3.4. Theoretical time-averaged OPD_{RMS} for the two acoustic waves ($u+c$ and $u-c$) for the blade pass frequency (534 Hz) at Mach 0.6 with a RMS sound pressure of 1 Pa (SPL of 94 dB), l_n of 1 m, and Ap of 15 cm.

region, so that the time-averaged OPD_{RMS} begins to decrease compared to the $\theta = 0^\circ$ case below $\Lambda/Ap = 1$. There are also points of zero optical disturbance that occur at $\theta_{zero} = \tan^{-1}(n\Lambda/l_n)$ for $n \neq 0$; these points occur because the peaks and valleys of the optical disturbance caused by the sound wave effectively cancel out over the length of the integration path, $l_n/\cos\theta$.

Figures 3.2 and 3.3 show the optical effect of plane acoustic waves in a no-flow environment. The effect of wind-tunnel flow is to stretch (downstream-traveling waves) or compress (upstream-traveling waves) the wavelength of the acoustic noise thereby altering the filtering effect of the beam aperture. Figure 3.4 shows a typical optical disturbance from the two transverse acoustic waves ($u+c$ and $u-c$) present in a wind tunnel at Mach 0.6. Both waves have an RMS sound pressure of 1 Pa and the beam has an aperture of 15 cm and propagates through an acoustic field inside a duct of width, l_n , of 1 m. Over the vast majority of the look back angles the upstream-traveling acoustic wave has a much greater effect on the optical disturbance compared to the downstream-traveling acoustic wave, due to the much shorter wavelength of the upstream-traveling waves which is less affected by aperture filtering. However, the upstream-traveling wave goes through several zero points so that the downstream-traveling wave dominates at some beam angles.

3.2.2 Spherical Acoustic Waves

The acoustic field from a speaker may be assumed to be a spherical wave from a pulsating point if the frequency is sufficiently low and the measurement region is far enough away from the source

[48]. This pressure field when converted to complex pressure is represented by

$$\hat{p}(r, t) = \frac{A_0}{r} \exp \{-j(kr - \omega t)\}, \quad (3.12)$$

where A_0 is the fluctuating pressure strength and r is the distance from the source to the measurement point. The RMS pressure of this field can be represented by

$$p_{rms} = \frac{|A_0|}{r\sqrt{2}}. \quad (3.13)$$

3.2.2.1 Theoretical OPD Calculations

A set of optical properties were calculated for a beam passing through a spherical acoustic field as defined by a point source using the process described previously in Section ?? and shown in Figure 3.5. These calculations used a circular aperture size of 0.25-m in diameter that was assumed to be measured using a Shack-Hartmann WFS with 32x32 sub-apertures with a non-dimensional acoustic wavelength, Λ , of $Ap/4$ to $10Ap$. The normal vector from the point source to the axis of the measurement beam defined the coordinate system. This normal distance, R , was a minimum $5Ap$ and a maximum of $25Ap$, keeping the measurement beam away from the singularity at the origin of the acoustic source. The OPD for the beam was integrated over a distance of ± 5 -m from the plane of the point source. To calculate the time-averaged OPD_{RMS} the phase of the source was varied from 0 to 2π with 25 total steps.

The result of these OPD_{RMS} calculations is shown in Figure 3.6. The top plots shows the expected optical disturbance ratio, $OPD_{RMS}/|A_0|$, for a perfectly spherical acoustic field measured over the beam length. The oscillations in the solutions for different R/Ap are caused by end effects in the integration. Because speakers often have a directivity in their emission, the oscillations can be greatly reduced by using a windowing function in the z-direction, such as a Hanning or Tukey window, the roughly model this directivity as shown in the bottom plot. While this plot was calculated with a single aperture diameter, the general trend holds for all other aperture diameters that were tested, the only effect was the size and width of the oscillations.

The peak of the optical disturbance ratio, $OPD_{RMS}/|A_0|$, is located at $\Lambda/Ap \approx 0.75$ for a circular aperture. The signal is reduced above this value due to aperture filtering and below this value because the shorter wavelengths have a reduced distance before alternating high and low index-of-refraction regions reduce the optical path difference. When the acoustic source point is sufficiently far enough away from the measurement beam, $R/Ap \geq 2$, the optical disturbance ratio,

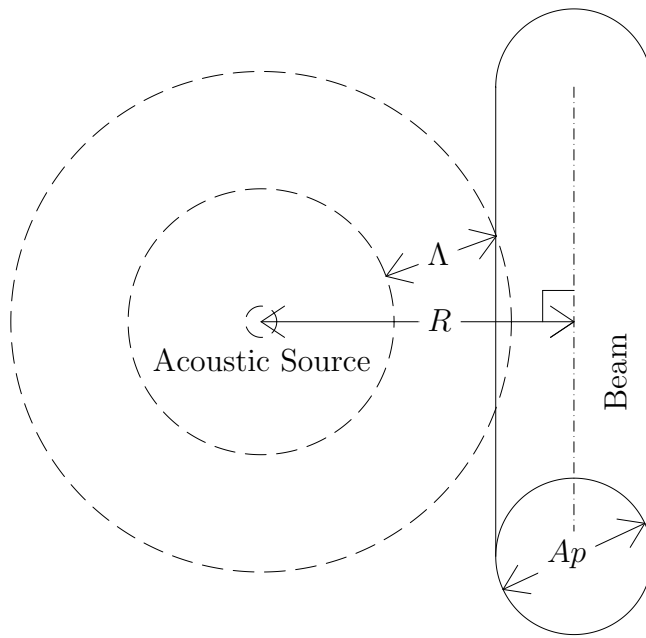


Figure 3.5. Diagram of the geometry used in the spherical wave simulation.

$\text{OPD}_{\text{RMS}} / |A_0|$ when multiplied by $\sqrt{R/Ap}$, can be collapsed onto a single curve for a range of Λ/Ap of 0.1 to 10. Above $\Lambda/Ap = 10$ the curves start to diverge away from one another. An approximate function fit to these data is

$$\frac{\text{OPD}_{\text{RMS}} \sqrt{R/Ap}}{|A_0|} \approx \frac{p_1(\Lambda/Ap)^3 + p_2(\Lambda/Ap)^2 + p_3(\Lambda/Ap) + p_4}{(\Lambda/Ap)^3 + q_1(\Lambda/Ap)^2 + q_2(\Lambda/Ap) + q_3} \quad (3.14)$$

with coefficient values shown Table 3.1. This functional fit has a coefficient of determination, R^2 , value of 0.9991.

3.2.2.2 Measurement of a Spherical Acoustic Wave with an Optical Beam

A small bench top experiment was used to compare the simultaneous optical and microphone measurements of an acoustic field from a speaker as shown in Figure 3.7. The distance from the center of the beam to the speaker was 102 mm with a beam diameter of 28 mm. An ACO model 7016B microphone [12] was placed directly over the speaker at a distance of 158 mm and was used with a Brüel & Kjær model 2670 preamplifier [7]. The speaker used was a Peerless model XT25SC90-04 [45] which has a fairly flat on-axis response from 1-kHz to 40-kHz.

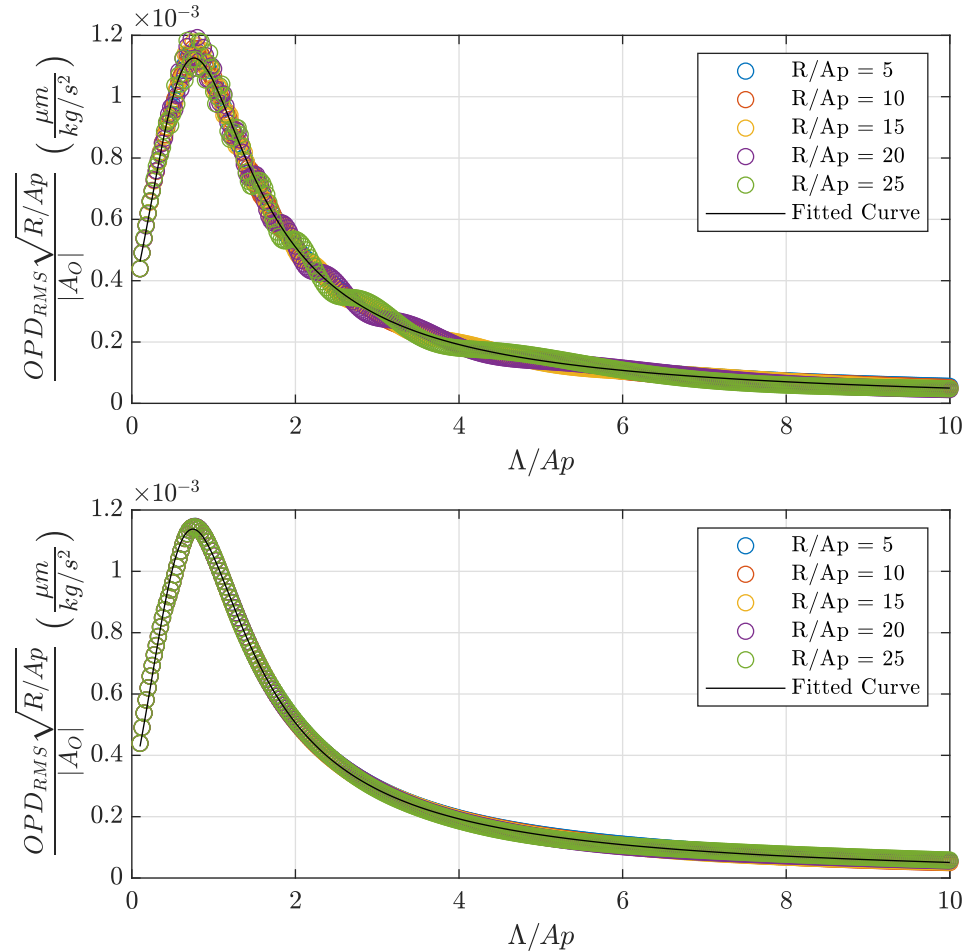


Figure 3.6. Theoretical time-averaged OPD_{RMS} for a spherical acoustic wave. The top plot shows a perfect spherical acoustic signal integrated over $\pm 5\text{-m}$. The bottom plot shows has a Tukey window applied along the beam length to partially emulate source directivity which significantly reduces the measured oscillations.

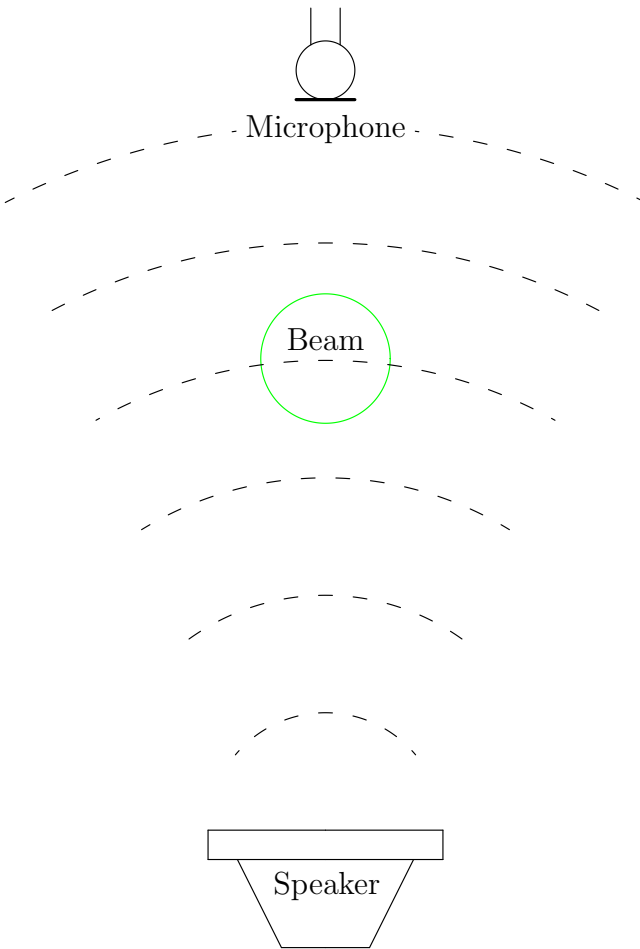


Figure 3.7. Spherical acoustic wave measurement test.

TABLE 3.1
CURVE FIT VALUES FOR FIGURE 3.6 AND EQUATION 3.14

Coefficient	Value
p_1	-1.845e-05
p_2	4.769e-04
p_3	4.520e-03
p_4	1.435e-03
q_1	5.399e+00
q_2	-5.145e+00
q_3	4.869e+00

The wavefront measurements system utilized in these measurements is similar to that shown in Figure 2.4 except there was no primary telescope. The speaker was located in the center of the measurement region which was about 2 feet in length and the re-imaging telescope reduced the beam diameter by a factor of two and re-imaged the return mirror. Optical wavefronts and microphone measurements were taken at 49 kHz. The speaker was sinusoidally excited at three different frequencies (9, 14, and 18 kHz) at a variety of voltages.

The absolute value of the fluctuating pressure strength, $|A_0|$, was calculated two different ways. First, the power spectrum of the microphone data was used to calculate the average p_{rms} at the excitation frequency and the fluctuating pressure strength using Equation 3.13. For the second method, the optical wavefront was band-pass filtered at the excitation frequency using a process that will be discussed in Chapter 6. The time averaged OPD_{RMS} of the filtered wavefront data was then used to calculate the fluctuating pressure strength using Equation 3.14.

The results of these measurements of the fluctuating pressure strength is shown in Table 3.2. The differences between the two techniques for measuring the fluctuating pressure strength fell into two groups. For the 9 kHz cases, the differences ranged from 20-26% while for the higher frequency cases the differences were between 1.1-1.5%. In all cases the wavefront measurement reported a higher fluctuating pressure strength. With the exception of the highest excitation case at 9 kHz, the differences between the two techniques was fairly constant for each frequency group. Some of these differences maybe attributable to the frequency response of the microphone.

TABLE 3.2

COMPARISON OF MICROPHONE AND WAVEFRONT COMPUTATION OF $|A_0|$

$f_{speaker}$	$V_{speaker}$	p_{rms}	OPD_{RMS}	$ A_0 _{mic}$	$ A_0 _{wf}$	Diff
(Hz)	(mV)	(Pa)	(μm)	(kg/s^2)	(kg/s^2)	(%)
9000	100	5.65	6.545e-04	1.26	1.55	20.38
9000	250	12.23	1.421e-03	2.73	3.36	20.56
9000	500	19.52	2.386e-03	4.36	5.64	25.62
14000	1250	5.20	6.831e-04	1.16	1.18	1.24
14000	250	9.33	1.230e-03	2.09	2.12	1.50
14000	375	9.68	1.272e-03	2.16	2.19	1.16
18000	125	3.73	4.987e-04	0.83	0.84	1.10

In Figure 3.8, measured wavefronts are compared to the wavefronts simulated using the method described in Section ?? for the highest excitation cases at each frequency. The 9 kHz case shows some anomalies on the measured wavefront on the right side, and deviates from a spherical wave significantly, likely contributing to the significantly higher estimated pulsating field strength value when compared to the microphone estimate in Table 3.2. The 14 and 18 kHz cases show some remarkable agreement between the measured and simulated images. Optical wavefront measurements can therefore be used for making non-intrusive acoustic field measurements especially when the acoustic field is simple.

3.3 Estimating the Acoustic Field Inside a Wind-Tunnel Test-Section

Several mode-matching methods have been previously employed to solve the acoustic field in ducts, ranging from methods designed to solve axially-segmented turbofan duct liners [36] to muffler modeling [25]. These methods require the entire field to be solved simultaneously because there are duct modes traveling in both directions at each axial-spatial location. Using the turbofan duct liner version, a single azimuthal order, m , and only a few radial orders, n , need to be computed for the various boundary conditions with a constant mesh used through all the segments. In the muffler model version, step changes in the cross-section are employed, allowing for a constant mesh to be generated to account for all possible cross-sections.

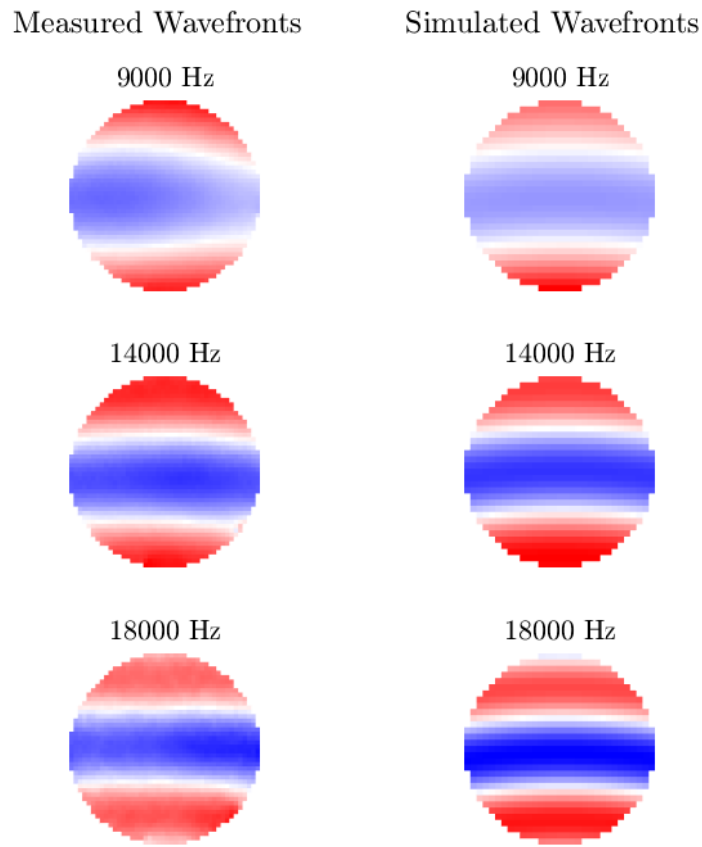


Figure 3.8. Comparison of measured wavefront to simulated ones for the highest-amplitude speaker excitation at each frequency.

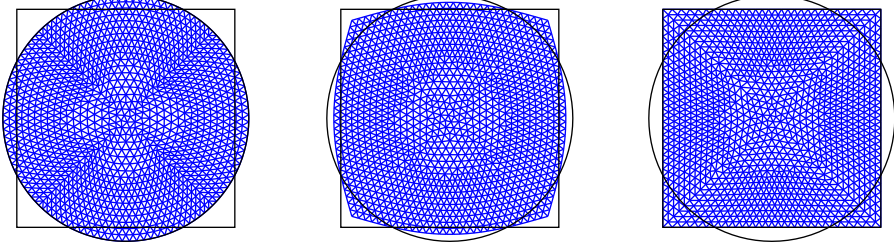


Figure 3.9. Deformable mesh for calculating the acoustic modes in the circular to square transitions at three stages.

For a wind-tunnel that has numerous cross-sectional area changes, specifically, a square cross-section for the test-section and a circular cross-section for the fan, the mode-matching method can become computational expensive. At each axial-location, all possible duct modes need to be calculated up to at the very least the cutoff mode k_m , if not higher [16], to fully resolve local duct modes. As such, in order to reduce the computational cost of simulating the acoustic environment inside of a wind tunnel, a mode marching method was employed instead of a mode-matching method, where an initial cross-sectional pressure field was marched from the wind-tunnel fan in both directions around the wind-tunnel and through the test-section. Although the mode-marching method is computationally simpler than the mode-matching method, there are also arguments for using the mode-marching method that are justified by the expected acoustic behavior in typical wind-tunnel circuits. Specifically, since the wind-tunnel test section normally has the smallest cross-sectional dimensions, higher-order acoustic modes tend to be reflected away from the test section; hence using a mode-marching method that does not rigorously account for reflections or all high-order modes should not add significant inaccuracy to the predicted results.

For the circular to square transition on either side of the wind-tunnel fan, a deformable mesh was used such that there would be a one-to-one mapping of mesh points throughout the transition. An example of the deformable mesh is shown in Figure 3.9 at both the square and circular limits and halfway in between. Because cross-sectional wavenumber scales with the area ($k_m^2 A = \text{const}$), all modes were solved for a cross-section of unit area. For the simulation of the Notre Dame White Field wind tunnel (described below) modes in the square cross-sections of the wind tunnel were calculated with both the deformable mesh and a rectangular mesh in order to allow for easy transitions in the cruciform region of this wind-tunnel's diffuser.

3.3.1 Mode-Marching Method Procedure

1. Starting Acoustic Pressure Disturbance

The method starts with an initial acoustic pressure disturbance that could be either measured, computed, or assumed.

$$\hat{p}^0(x, y) \quad (3.15)$$

For wind tunnels, the acoustic disturbance is generated by the main fan; hence \hat{p}^0 is the rotating radial fan modes associated with the rotating fan blades [?].

2. Modal Best Fit

The pressure disturbance at the current axial location is best fit to the possible modes.

$$\hat{p}^i(x, y) = \Psi_m^i(x, y) \cdot C_m^i \quad (3.16)$$

where Ψ_m^i are the possible modes for the local duct shape.

3. Transmitted Pressure Ratio

The pressure attenuation due to Mach number change [47] as a ratio of transmitted pressure to incident pressure is computed for an acoustic wave traveling with subsonic flow,

$$\frac{p_t}{p_i} = \left(\frac{1 + M_n}{1 + M_{n+1}} \right) \left(\frac{2M_{n+1}}{M_n + M_{n+1}} \right) \left(\frac{X_{n,n}}{X_{n,n+1}} \right) \left(\frac{X_{n,n}}{X_{n+1,n+1}} \right)^{1/(\gamma-1)}, \quad (3.17)$$

or traveling against subsonic flow,

$$\frac{p_t}{p_i} = \left(\frac{1 - M_n}{1 - M_{n+1}} \right) \left(\frac{2M_{n+1}}{M_n + M_{n+1}} \right) \left(\frac{X_{n,n}}{X_{n,n+1}} \right) \left(\frac{X_{n,n}}{X_{n+1,n+1}} \right)^{1/(\gamma-1)}, \quad (3.18)$$

where

$$X_{a,b} = 1 + \frac{\gamma - 1}{2} M_a M_b. \quad (3.19)$$

4. Reflected Pressure Ratio

The reflected pressure ratio is a useful quantity to keeping track of, because one of the main assumptions of the mode marching method is that the reflections are negligible. The pressure attenuation due to Mach number change [47] as a ratio of reflected pressure to incident pressure is computed for an acoustic wave traveling with subsonic flow,

$$\frac{p_r}{p_i} = \left(\frac{1 + M_n}{1 - M_n} \right) \left(\frac{M_{n+1} - M_n}{M_{n+1} + M_n} \right) \frac{Y_{n,n+1}}{X_{m,n+1}}, \quad (3.20)$$

or traveling against subsonic flow,

$$\frac{p_r}{p_i} = \left(\frac{1 - M_n}{1 + M_n} \right) \left(\frac{M_{n+1} - M_n}{M_{n+1} + M_n} \right) \frac{Y_{n,n+1}}{X_{m,n+1}}, \quad (3.21)$$

where

$$Y_{a,b} = 1 - \frac{\gamma - 1}{2} M_a M_b. \quad (3.22)$$

5. March Modes Forward

March the acoustic modes forward to the next axial location.

$$\hat{p}_{i+1}(x, y) = \frac{p_t}{p_i} \sum \Psi_m^i(x, y) \cdot C_m^i \cdot \exp\{\mp j k_{zm}^\pm z\} \quad (3.23)$$

6. Repeat

Repeat steps 2-5 until the desired location is reached (i.e. the wind-tunnel test section). Different starting pressure disturbances can also be checked.

3.3.2 University of Notre Dame White Field Wind-Tunnel Simulation

The University of Notre Dame White Field wind-tunnel is capable of reaching speeds of Mach 0.6 in the 3 foot by 3 foot test-section. A CAD model of the wind-tunnel is shown in Figure 3.10. The cross-sectional area and distance from the wind-tunnel fan going upstream are presented in Table 3.3 along with some comments on the segments between some of the cross-sections. For the distances in Table 3.3 the corners have been straightened out and set to a length equal to the center-line arc from the entrance to the exit of that segment. The transition segments on either side of the wind-tunnel fan convert the circular cross-section to a square cross-section. Between cross-section 6 and 7 the diffuser has a cruciform splitting it into four separate segments in which the duct modes were independently marched. The test-section is 2.75-m long and the main contraction shape from section 8 to 9 follows a fifth-order polynomial. Acoustic reflections that would be due to turning vanes or other internal structures have been neglected along with the fan hub and motor shaft geometry.

The wind-tunnel was discretized into smaller segments that were a maximum of 0.25-m in length. The speed throughout the wind-tunnel was determined via isentropic relations and the pressure transmission ratios were computed using Equations 3.17 and 3.18. Pressure reflection ratios were calculated using Equations 3.20 and 3.21 and verified to be small. Figure 3.11 shows these parameters for the tunnel at a Mach number of 0.6 in the test-section with flow going from right-to-left. For most of the wind-tunnel the Mach number is around 0.1 with the transmission pressure ratio (solid lines) at effectively unity. In the regions of rapid Mach number change around the contraction and the test-section diffuser, the transmission pressure ratio can deviate significantly from unity, especially for sound waves traveling upstream. These regions also show some reflected pressure ratios (dotted lines) that are non-negligible. For acoustic waves traveling in both directions, the section on the opposite side of the test section produces some reflected acoustic waves back into the test section.

The wind-tunnel fan was modeled using a circular duct mode of $m = 8$ and $n = 0$ at a frequency of 520-Hz which corresponds to the blade-passing frequency of the Mach number 0.6 case. The duct mode of $m = 8$ and $n = 0$ is the largest cut-on mode in which the azimuthal mode number is a whole-number fraction of the total number of fan blades, 32. The peak-to-peak acoustic pressure of the fan was set to unity to allow the results to be easily scaled. To check for the possibility of

TABLE 3.3
WIND-TUNNEL CROSS-SECTION SPECIFICATIONS

Section	Area (m^2)	Z (m)	Comment
1	5.07	0.00	Circle to Square Transition
2	4.68	2.42	
3	4.68	4.56	
4	3.57	8.65	
5	3.57	10.71	
6	1.97	14.33	Cruciform
7	0.84	17.99	Test-Section
8	0.84	20.73	Sixth Order Contraction
9	5.44	23.07	
10	5.44	24.30	
11	5.44	26.54	
12	8.04	29.65	
13	8.04	31.88	Circle to Square Transition
14	4.67	39.25	

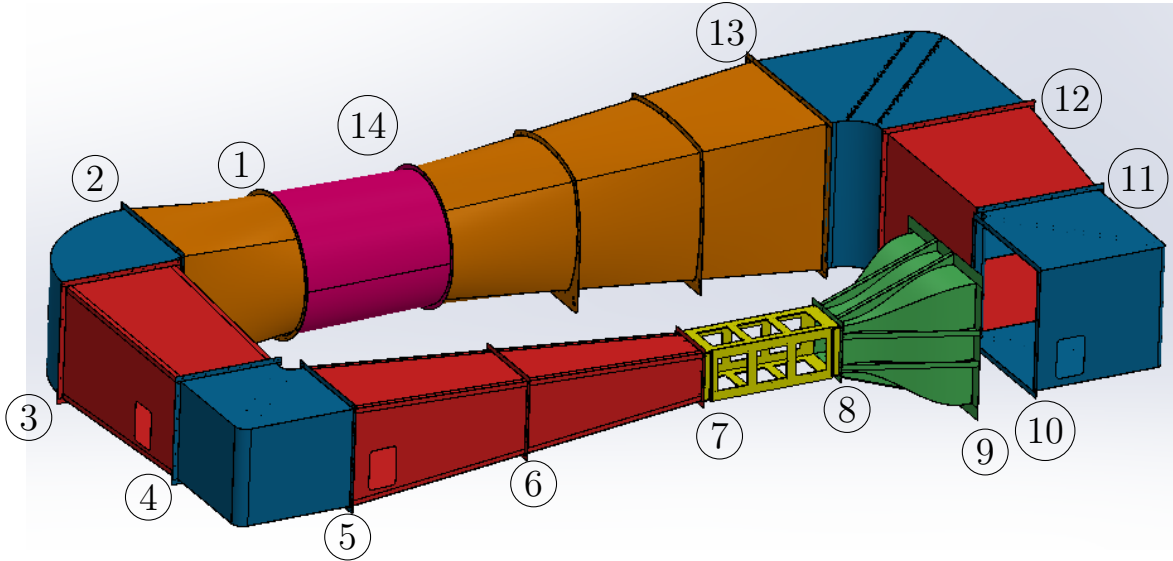


Figure 3.10. CAD model of the University of Notre Dame Whitefield wind-tunnel. The specifications of the tunnel at the numbered cross-sections are shown in Table 3.3.

some duct modes only being present at certain orientations of the fan blades, the initial acoustic pressure disturbance was rotated by replacing ωt in the temporal portion of Equation 2.31 with a phase offset that varied from 0 to 2π .

Cross-sectional slices of the acoustic field as the waves march upstream from the fan through the circle to square transition are shown in Figure 3.12. The plots on the left side are at an initial phase angle of 0-radians and the right side are at a phase angle of $\pi/2$ -radians. The top plots are the cross-sectional slices of the acoustic field directly upstream of the fan, the middle plots are halfway through the transition, and the bottom plots are just into the square duct. As an acoustic wave propagates upstream, a phase shift can be observed with the halfway transitioned cross-sectional slices having an opposite local phase. As the acoustic wave enters the square duct the 0-radian phase, left side, bears little resemblance to the original acoustic wave while the $\pi/2$ -radian phase shows some significant similarities.

The acoustic field cross-section at the center of the test-section is shown in Figure 3.13 for a variety of initial phase angles. As the fan blades rotate so too does the acoustic field within the test-section. The real component of the duct modes are shown in Figure 3.14 as a function of the initial phase angle. The primary duct mode in the test-section is the $m = 2, n = 2$ mode with contributions from pairs of modes $m = 0, 2, n = 2, 0$ which are in phase with one another and out of phase mode pairs $m = 1, 3, n = 3, 1$. Note that for Figures 3.14 and 3.15 the $m = 0, 2, n = 2, 0$

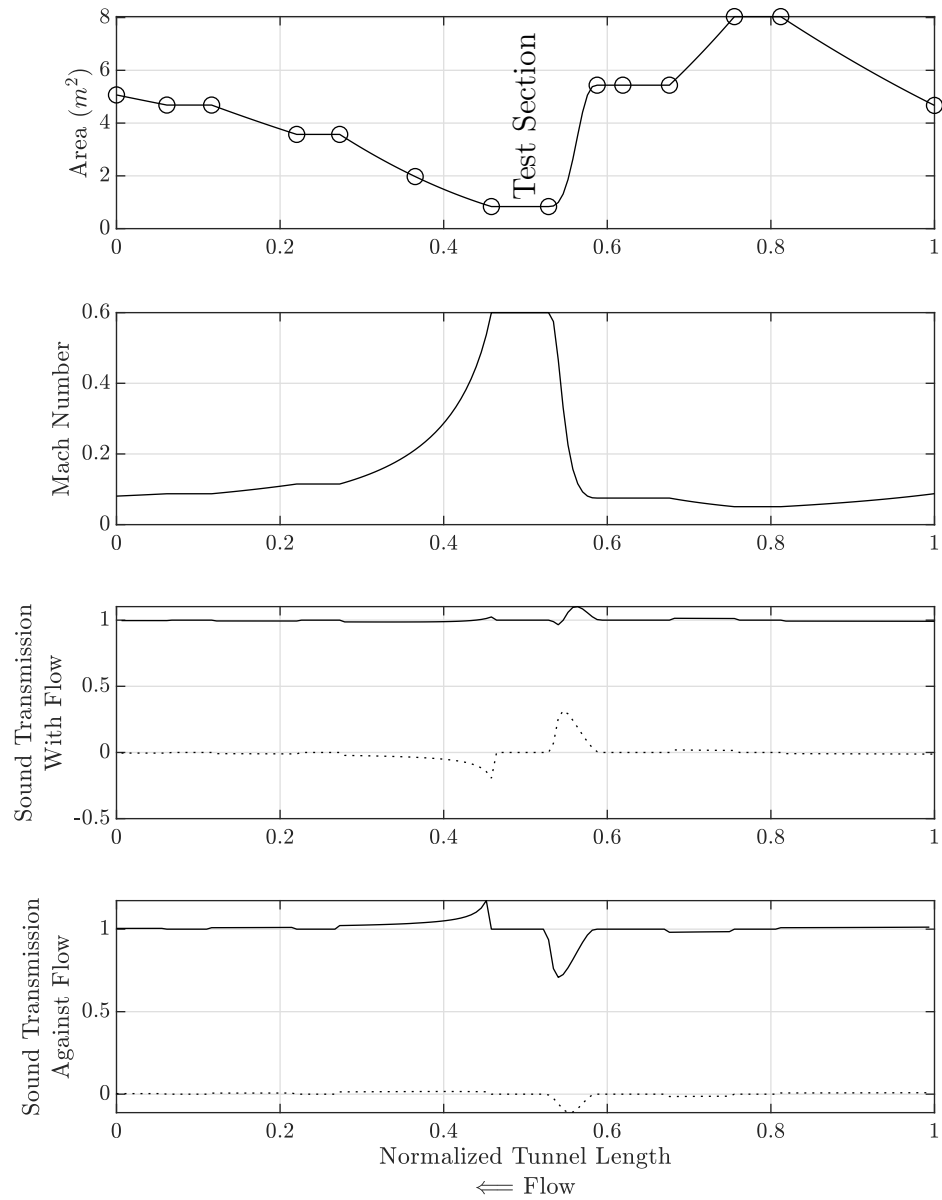


Figure 3.11. Wind-tunnel discretization at a Mach number of 0.6. The solid lines in the sound transmission plots represent the transmitted pressure ratio while the dotted lines represent the reflected pressure ratio.

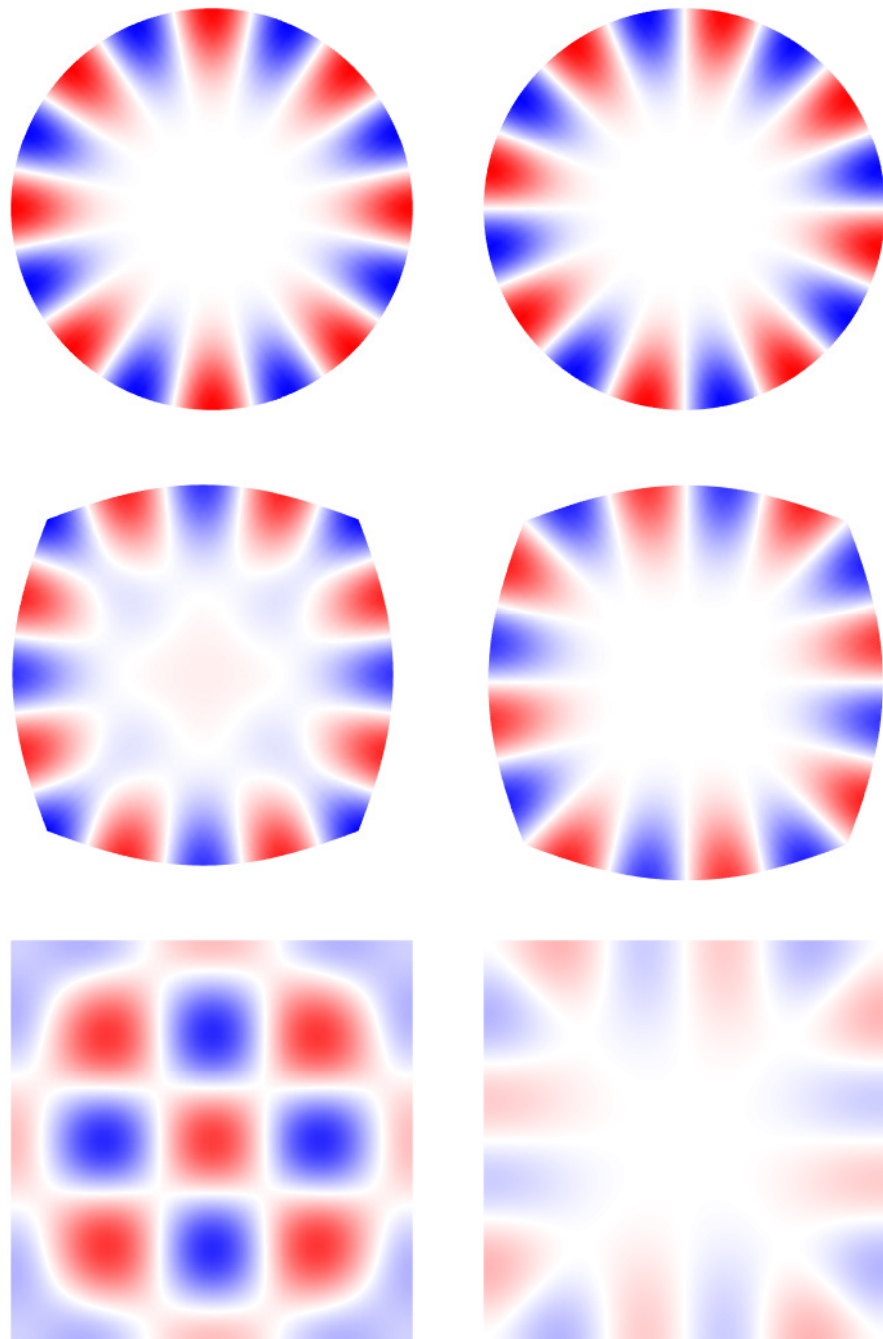


Figure 3.12. Cross-sectional slices of the acoustic field through the circle to square transition for the acoustic waves traveling upstream. Left side are the waves traveling from the fan at a phase of 0 -radians and the right side at a phase of $\pi/2$ -radians. The top plots are the fan acoustic field, the middle plots are halfway through the transition, and the bottom plots are just into the square duct.

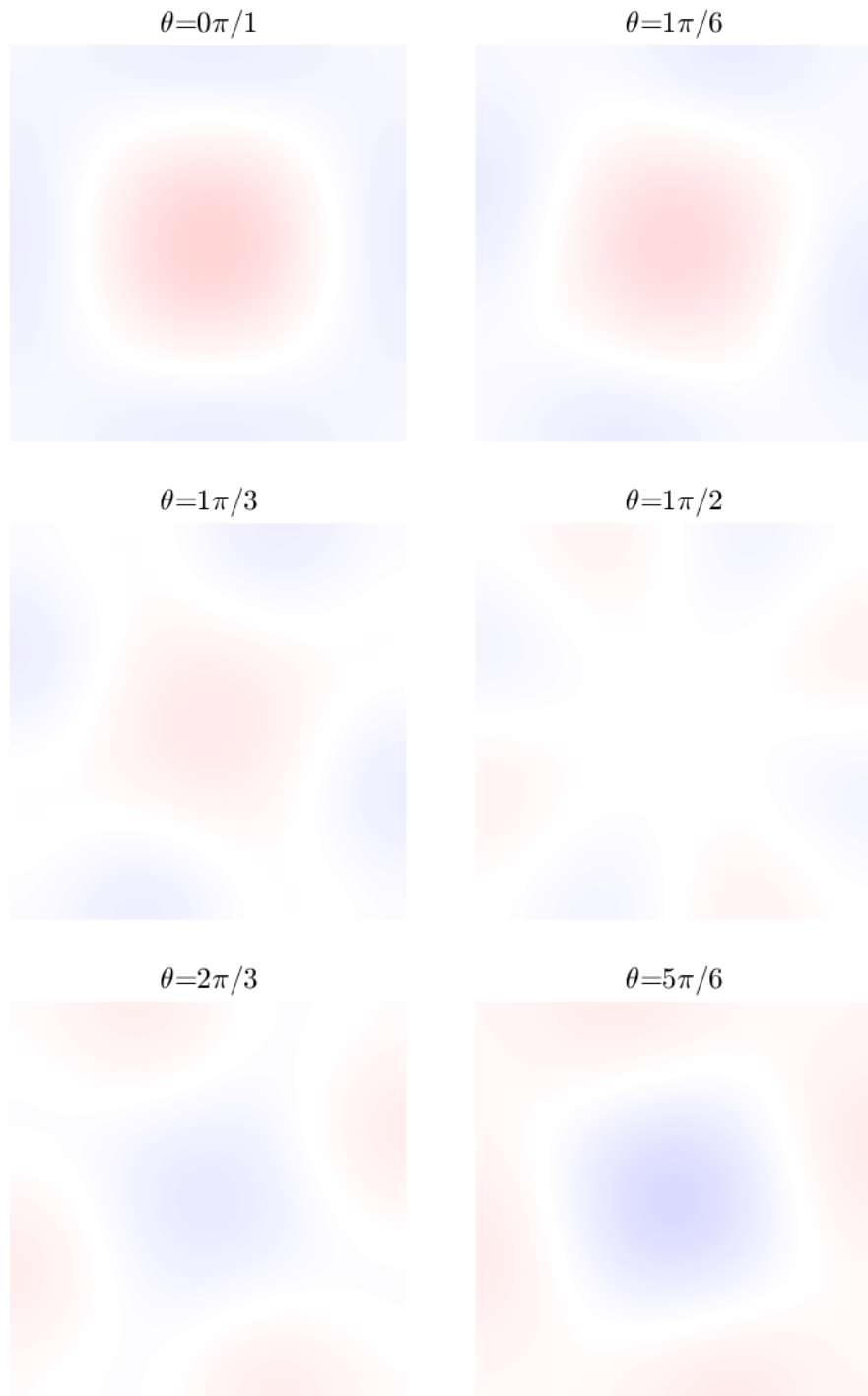


Figure 3.13. Cross-sectional acoustic field slices in the center of the test-section at various initial phase angles.

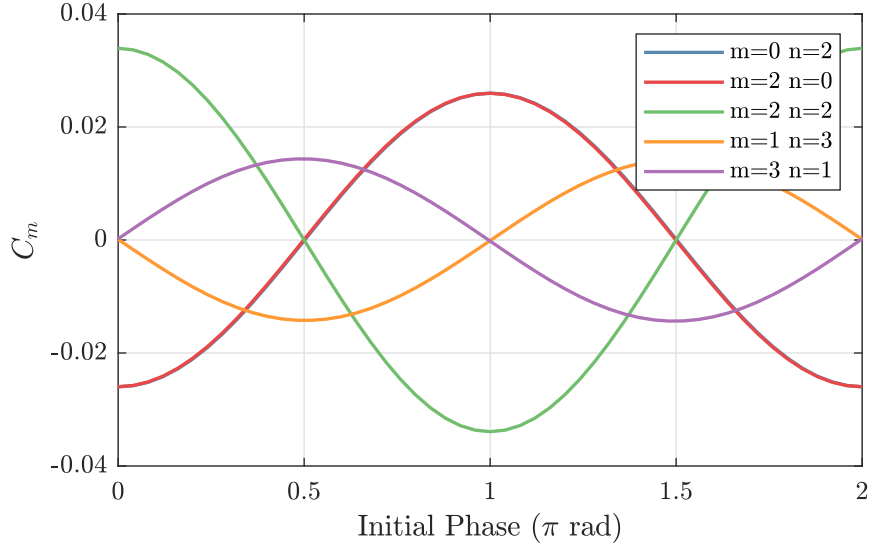


Figure 3.14. The real component of the acoustic mode coefficients making up the upstream-traveling acoustic field in the middle of the test-section as a function of the initial phase angle.

modes overlap one another in the plots. These five modes can be used to simulate the optical response of the fan driven acoustics inside of the test section by using the maximum value of the modal coefficient and a relative phase angle between the different modes by using Equation 2.31 and

$$\widehat{\text{OPD}}(x, y) = \frac{K_{GD}}{c_0^2} \int_{z_1}^{z_2} \hat{p}(x, y, z) A_p dz, \quad (3.24)$$

where $\widehat{\text{OPD}}$ is the complex optical path difference and K_{GD} is the Gladstone-Dale constant. The temporal portion of Equation 2.31 can be applied after the integration process in Equation 3.24 and just before taking the real component to simulate a measured value at a particular instant in time.

The acoustic duct modes in the center of the test-section for the acoustic waves traveling in the direction of the flow are shown in Figure 3.15. The downstream-traveling acoustic field inside of the test-section is comprised of the same duct modes as the upstream-traveling acoustic field but the mode coefficient are approximately an order-of-magnitude lower. All of the phase offsets for the modes remain the same except for the $m = 2, n = 2$ mode which is now different by π radians compared to the upstream-traveling modes in Figure 3.14. When the downstream-traveling acoustic field enters the cruciform after the test-section a portion of it is reflected, see Figure 3.11. When the maximum reflected pressure ratio, approximately -0.2, is combined with the strength of the downstream-traveling acoustic field, the acoustic field reflected back into the test-section is 1-2

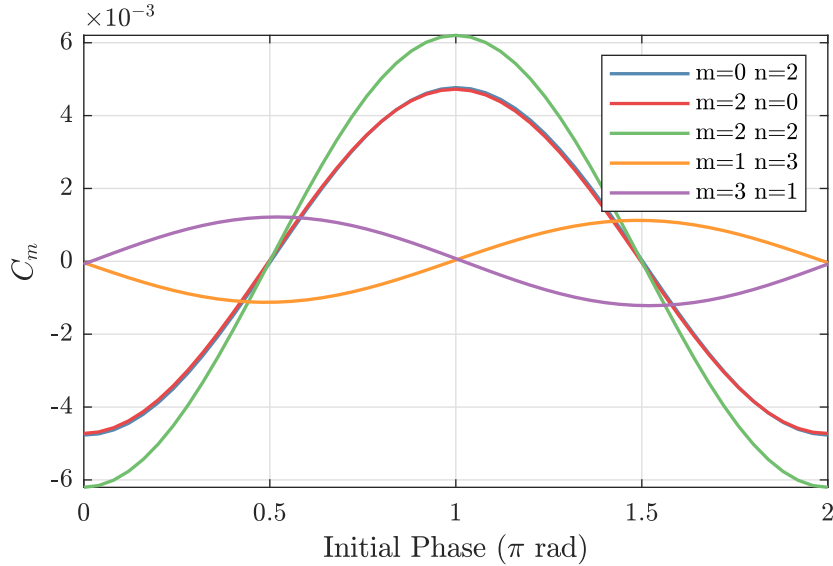


Figure 3.15. The real component of the acoustic mode coefficients making up the downstream-traveling acoustic field in the middle of the test-section as a function of the initial phase angle.

orders-of-magnitude lower than the upstream-traveling acoustic field from the fan. On the other hand, the reflected field from the upstream-traveling acoustic field after it leaves the test-section is on the same order-of-magnitude as the downstream-traveling acoustic field.

A comparison between a measured optical wavefront that has been band-pass filtered at the blade-passing frequency and a simulated optical wavefront that has been shot through the estimated acoustic field computed by the mode-marching method is shown in Figure 3.16. Qualitatively, there is significant agreement between the two wavefronts. Since there was no microphones installed in either the test-section or around the wind-tunnel fan, there cannot be a quantitative comparison made.

3.4 Summary

Acoustic waves affect the transmission of light by causing the local index-of-refraction to change with the pressure fluctuations. When the acoustic field is well modeled, as was the case with the spherical wave measurements, an optical wavefront measurement can provide an accurate measurement of the acoustic field strength non-intrusively.

The mode-marching method provides a computationally rapid way of estimating an acoustic signal as it travels through a duct system like a wind-tunnel. This method assumes that the

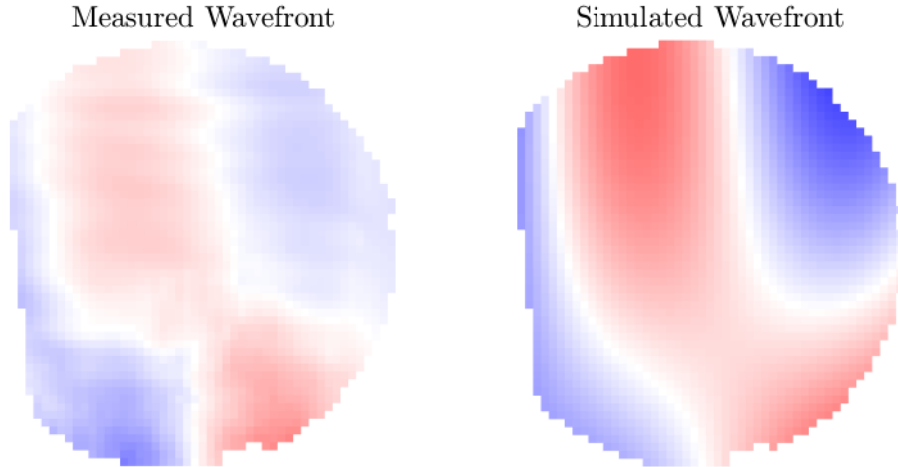


Figure 3.16. Comparison of a measured optical wavefront and a simulated one passing through the estimated acoustic field.

reflected component will be minimal and can be ignored. A significant contribution of this work to the computational procedure of this method is computing the eigen-functions for the wind-tunnel fan transition geometries that are neither circular nor rectangular. These computations would become even more costly if the cross-section cannot be assumed to have a uniform flow speed [60]. Finally, note that the mode-marching method used here has neglected the effect that the corners would have on the signal or other internal geometry such as the turning vanes or the turbulence screens.

The main benefit to using a mode-marching method is to simulate narrow-band signals that appear in the optical wavefront spectra and to have some level of confidence that the source of that signal is the wind-tunnel fan. If the narrow-band signal does not match up with the simulated signal, it could have a source that may not be due to the testing environment and would likely need to be investigated further. If there is significant agreement between the measured and simulated signals, a simple stop-band filter could be used to eliminate the contamination.

CHAPTER 4

MULTIDIMENSIONAL SPECTRAL ESTIMATION OF OPTICAL WAVEFRONTS

As described in Chapter 1, the objective of this research is to develop methods to evaluate and, if possible, eliminate the effect of facility-related acoustic noise on aero-optical measurements. As such, the first goal of the research is to establish analytical methods to identify and isolate acoustic sources of optical signals within a given data sample. This is a significant challenge since, as will be shown later, acoustic sources of optical aberrations typically have a magnitude and frequency content that is in the same range as the signal that is the objective of the measurement. This chapter will begin with a brief overview of some of the benefits to analyzing multidimensional data in this way, followed by a short discussion on how these spectrum are calculated, and conclude with a more in depth discussion on the analysis of multidimensional spectral estimates.

The multi-dimensional spectral approach that is employed throughout this research helps identify and characterize acoustic sources of optical noise as well as aero-optical signals. The spectral approach is also used as the basis for methods to filter the acoustic sources. For measurements in multiple dimensions, such as a line of sensors that are recorded over time, a multidimensional spectral estimation not only produces temporal frequency content but can also be used to identify the direction and speed of travel of a particular wave. The benefits of using multidimensional spectral estimation are shown in Figure 4.1. A single row of sub-apertures was from an optical wavefront measurement with a 5 inch diameter beam propagating normally through a wind-tunnel test section with a free-stream Mach number of 0.5. This measurement was performed in the University of Notre Dame Whitefield Wind Tunnel in a test section that contained a model representing the fuselage of the AAOL aircraft [28] with window that was flat and flush to the outer mold line of the fuselage. The top plot shows a traditional power spectrum ensemble-averaged over the row of data. Both the blade-passing frequency (517 Hz) and its sub-harmonic had similar amplitudes with an additional five harmonics showing significant spikes above the local baseline measurement. There are three additional strong peaks at approximately 3100, 4850, and 5850 Hz that are likely due to additional fan vibration that is currently limiting the top speed of the tunnel.

Both the middle and bottom plots show the multidimensional spectral estimation plot of two-

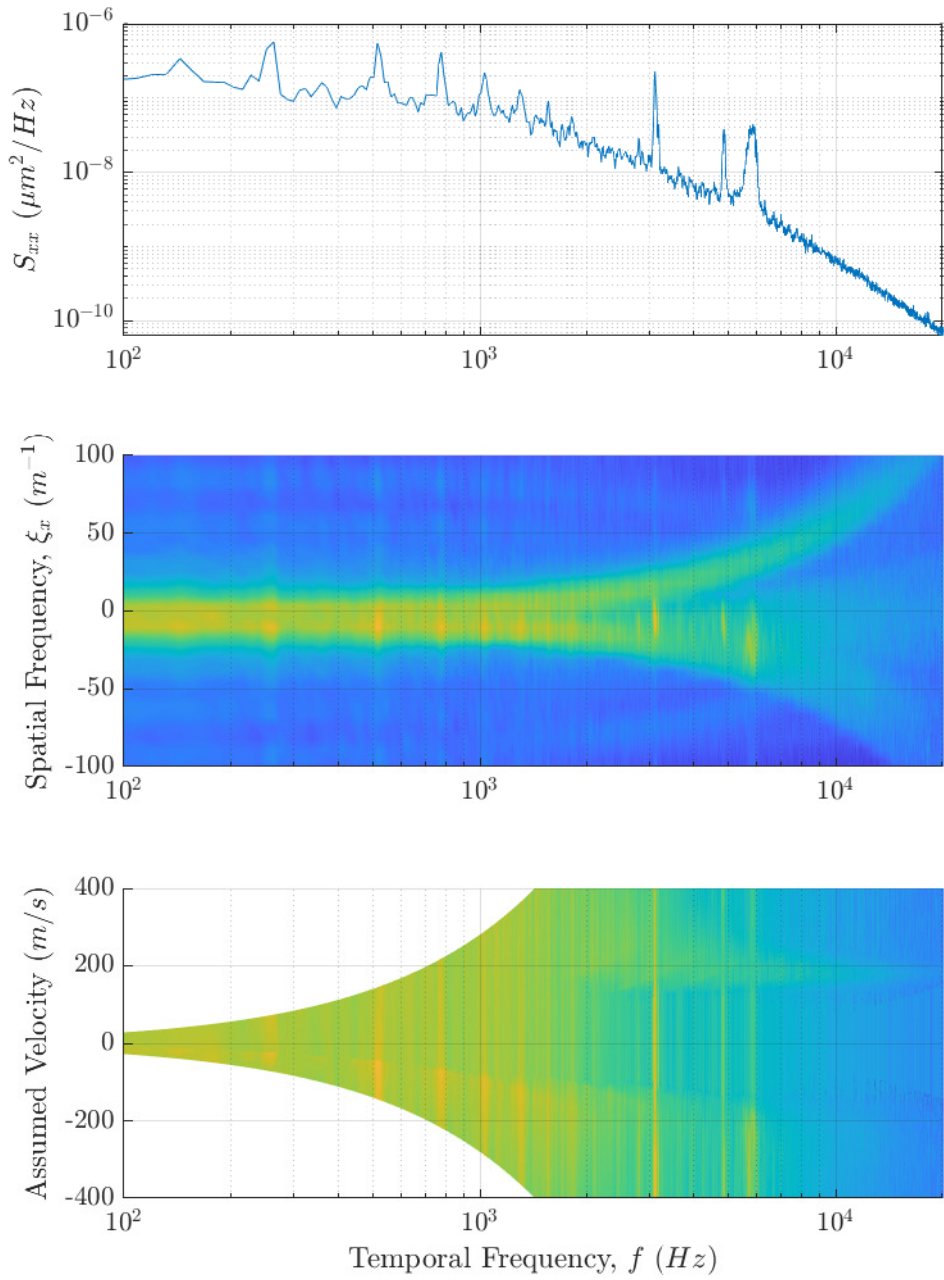


Figure 4.1. Multidimensional spectral estimation plot example and comparison to traditional power spectrum measurements. A single row of an optical wavefront measurement was used in this example. The top plot shows the typical power spectrum averaged over the entire row of data. Both the middle and bottom plots show the multidimensional spectrum plot with the y-axis as spacial-frequency in the middle and velocity in the bottom assuming $u = f/\xi_x$.

dimensional measurement. The colorbars were intentionally not shown in order to allow for all three plots to be aligned in the temporal-frequency axis and the color is representative of the logarithm of the power or variance in the wavefront signal (i.e. $\text{OPD}_{\text{RMS}}^2$) with yellow representing more power and blue representing less. The colorbar range in this plot is the same is constant with the other plots throughout this chapter. In the middle plot the y-axis represents the stream wise spatial frequency, ξ_x with the units of inverse meters. It is important to note that, unlike temporal-frequencies, spatial-frequencies can have positive or negative values depending on the direction of travel of the disturbance; this means that, waves with positive spatial-frequencies are moving in the direction of flow. The upstream and downstream traveling signals begin to diverge at around 2000 Hz with the signal below that point primarily laying on the upstream traveling side of the plot. The blade-passing frequency and its various harmonics can also be discerned in the center plot, by the vertical “streaks” that line up with the peaks in the standard spectrum shown in the top plot; the center spectral plot shows that these fan blade-passing signals have significant broadband spatial-frequency content. All of these narrow-band signals have a majority of their signal traveling upstream. In addition to optical disturbances branching off in the upstream and downstream moving directions there are significant disturbances along zero spatial-frequency representing a collection of standing waves. Elsewhere in this paper the multidimensional spectral estimation will be plotted with the temporal-frequency axis linearly. This data has been plotted logarithmically along the temporal-frequency axis to better show the low frequency content. When plotted linearly, the two primary upstream and downstream traveling signals lay in a straight line.

A dispersion analysis can be performed on these multidimensional spectral estimates. In order to obtain the velocity of a given wave we can start with the most basic forms of the wave equation,

$$\hat{y} = a \exp\{j\theta\}, \quad (4.1)$$

where θ is the phase of the wave and equal to $kx - \omega t$. From here we can take the partial of θ with respect to time and set it equal to zero,

$$\frac{\partial \theta}{\partial t} = 0 = \frac{\partial k}{\partial t} \frac{\partial x}{\partial t} - \frac{\partial \omega}{\partial t} \frac{\partial t}{\partial t}, \quad (4.2)$$

which can be rearranged to

$$u = \frac{\partial \omega}{\partial k} = \frac{\partial f}{\partial \xi}. \quad (4.3)$$

If we are to assume that a wave packet intercepts the origin ($f = \xi = 0$) then every point on the

spectral plot can be labeled with an assumed velocity,

$$u_{assumed} = \frac{f}{\xi_x}. \quad (4.4)$$

The bottom plot shows the same multidimensional spectral estimation plot as the middle one but with the y-axis representing an assumed velocity. There is not much in the way of velocity measurement capability at low temporal-frequencies. The primary optical disturbance moving in the direction of flow is moving at the free-stream velocity of approximately 175 m/s. The upstream traveling disturbance is traveling at the same speed but due to the signal being broader is more difficult to measure this way. The stationary modes in the middle plot are nowhere to be found on the bottom plot. When the assumed velocity for these waves is calculated their speed approaches infinity.

4.1 One-Dimensional Power Spectrum Calculation

Power spectral analysis is typically performed on one-dimensional data sets, for example, a single sensor measurement over time. On the other hand, if a sensor array were used, a multi-dimensional power spectrum could be computed that would also show spatial frequency information at each instant in time. For a single-point measurement that varies in time, $x(t)$, the power spectrum calculation is

$$S_{xx} = \frac{|\text{FFT}\{x(t)\}|^2}{N f_s}, \quad (4.5)$$

where FFT is the Fast Fourier Transform, N is the number of samples, and f_s is the sample rate [4]. For data that has only a real component the Fast Fourier Transform function produces magnitude and phase relations at each frequency step, f_s/N , over the range from zero-frequency up to but not including the Nyquist frequency, $f_s/2$, with a mirrored set of data that can be represented either below (starting at $-f_s/2$) or above (ending just below f_s) this range. The Nyquist frequency not being included and the mirrored data is due to an assumption that is integral to the Fourier Transform, which is that the signal is assumed to be periodic.

The total energy, σ^2 , of the signal must be preserved through the transform from physical space-time to frequency space

$$\sigma^2 = \frac{\sum x^2(t)}{N} = \Delta f \sum S_{xx}(f). \quad (4.6)$$

Additionally, because of the periodic nature of the Fourier Transform and a finite sample length of discrete data, spectral leakage can cause the power in one frequency bin to leak into adjacent frequency bins. To minimize this spectral leakage, windowing functions are employed which typically force the end points of the signal to zero. The Hann window,

$$w(t) = 1/2 \left[1 - \cos \left(\frac{2\pi t}{T} \right) \right], \quad (4.7)$$

is one of the more commonly used windowing functions [6] where $w(t)$ is the window function, t is the time at a given sample, and T is the total sample time. Since the windowing of a data set changes the signal energy some correction is needed to be applied. For an arbitrary windowing function the correction factor, c_w , can be obtained by substituting the windowing function in place of $x(t)$ in Equation 4.6,

$$c_w = \frac{1}{\sqrt{\sum w^2(t)/N}}. \quad (4.8)$$

For a Hann window this correction factor approaches $\sqrt{8/3}$ as N goes to infinity. When Equation 4.5 is combined with a windowing function and associated correction the double sided power spectra equation in one dimension becomes

$$S_{xx} = \frac{|c_w \text{FFT}\{x(t)w(t)\}|^2}{N f_s}. \quad (4.9)$$

A simple MATLAB function for computing the power spectrum of a one-dimensional signal with an arbitrary windowing function is shown in Appendix ??.

4.2 N-Dimensional Power Spectra Calculation

For measurements with multiple spatial and temporal dimensions the Fast Fourier Transform is applied n -times where n is the total number of dimensions, with each application in a different dimension,

$$\text{FFT}_n(x) = \text{FFT}(\text{FFT}(\cdots \text{FFT}(\text{FFT}(x, 1), 2) \cdots, n-1), n), \quad (4.10)$$

where $\text{FFT}(x, n)$ is the Fast Fourier Transform of x in the n^{th} dimension [3]. For a n -dimensional array the operation becomes [37]

$$\mathbf{S}_{\mathbf{xx}} = \frac{|c_w \text{FFT}_n\{f(\mathbf{x})w(\mathbf{x})\}|^2}{\prod \overrightarrow{N f_s}}, \quad (4.11)$$

where $\mathbf{S}_{\mathbf{xx}}$ is the n -dimensional power spectra array or dispersion array, $f(\mathbf{x})$ is a n -dimensional set of data, $w(\mathbf{x})$ is a n -dimensional windowing function, \vec{N} is a vector denoting the number of elements in each dimension, \vec{f}_s is a vector denoting the sample rate in each dimension, and

$$c_w = \frac{1}{\sqrt{\sum w^2(\mathbf{x}) / \prod \vec{N}}}. \quad (4.12)$$

The signal energy conservation relationship becomes

$$\sigma^2 = \frac{\sum_{\mathbf{x}}}{\prod \vec{N}} = \prod \vec{\Delta f}_s \sum \mathbf{S}_{\mathbf{xx}}, \quad (4.13)$$

where $\vec{\Delta f}_s$ is a vector representing the frequency step sizes in each dimension. A simple MATLAB code for calculating the dispersion of x with an arbitrary windowing function is shown in Appendix ??.

4.3 Non-Rectangular Spatial Windows

For n -dimensional data sets that fill a rectangular array, a windowing function can be created by multiplying together a series of one-dimensional windowing functions in the direction of each dimension. For non-rectangular data sets, such as is often the case with optical wavefront measurements, a windowing function can take some additional steps in its construction. In cases when the spatial measurement locations are constant throughout time, the windowing function can be split into two separate components,

$$w(\mathbf{x}) = w_t(t) \cdot w_s(x, y), \quad (4.14)$$

the temporal windowing function, $w_t(t)$, and the spatial windowing function, $w_s(x, y)$. This study uses a Hann window for the temporal windowing function and a modified Hann window for the spatial windowing function. For the case of a perfectly circular aperture, the Hann window can be reformulated to be based on the normalized radius, ρ_N , of the aperture,

$$w_s(\rho_N) = \begin{cases} \frac{1+\cos(\pi \cdot \rho_N)}{2} & \text{if } \rho_N < 1 \\ 0 & \text{otherwise.} \end{cases} \quad (4.15)$$

This modified Hann window is two-dimensional with a value of one at the center of the aperture and decreases to zero at the edge of the aperture in the same manner as a Hann windows decreases

from the center to either end.

Because the wavefronts measurements often had a clipped edge or some other obscuration, a different method was employed in this study. For an arbitrary shaped aperture, the minimum distance from any given measurement location to the edge of the aperture was used to create the spatial windows. The minimum distance can be computed given the a set of points (x and y) that spans the measurement range and the set of points outside of the aperture (x_O and y_O),

$$d_{min}(x, y) = \min \left\{ \sqrt{(x - x_O)^2 + (y - y_O)^2} \right\}. \quad (4.16)$$

This distance is then normalized by the maximum value and the resulting spatial window given a modified Hann window,

$$w_s(x, y) = \frac{1 + \cos \{\pi \cdot (1 - d_{min}^{norm}(x, y))\}}{2}. \quad (4.17)$$

This same basic idea can be extended to data sets where the locations of measurements in space vary with time.

4.4 Wavefront Multidimensional Spectrum

At the beginning of this chapter a multidimensional spectral plot for data resolved in time and one spatial dimension was shown along with a typical power spectrum plot in Figure 4.1. This was shown to facilitate a simple discussion of some of the benefits of using multidimensional spectrum analysis on optical wavefronts. That simple analysis was performed on only a single row of a wavefront data set and provided an insight into the disturbances that were moving in the horizontal (stream wise) direction only. When multidimensional spectral estimation is performed over all dimensions of a wavefront (i.e. time and both spatial dimensions), as will be done for the remainder of this chapter, additional detail is available, that also enables the determination of optical disturbances moving vertically (i.e. cross-stream to the flow) or any direction in between. Figure 4.2 shows a comparison between the two-dimensional single row spectrum and a three-dimensional spectral slice showing the horizontal moving optical disturbances at both zero-vertical spatial frequency and integrated through the vertical spatial frequencies in order to obtain the two-dimensional spectrum. The top plot shows the three-dimensional spectral estimation plot at $\xi_y = 0 \text{ m}^{-1}$, which shows planar waves traveling in the horizontal direction. The middle plot shows the three-dimensional spectrum integrated through the vertical spatial-frequency axis creating an estimate of the two-dimensional

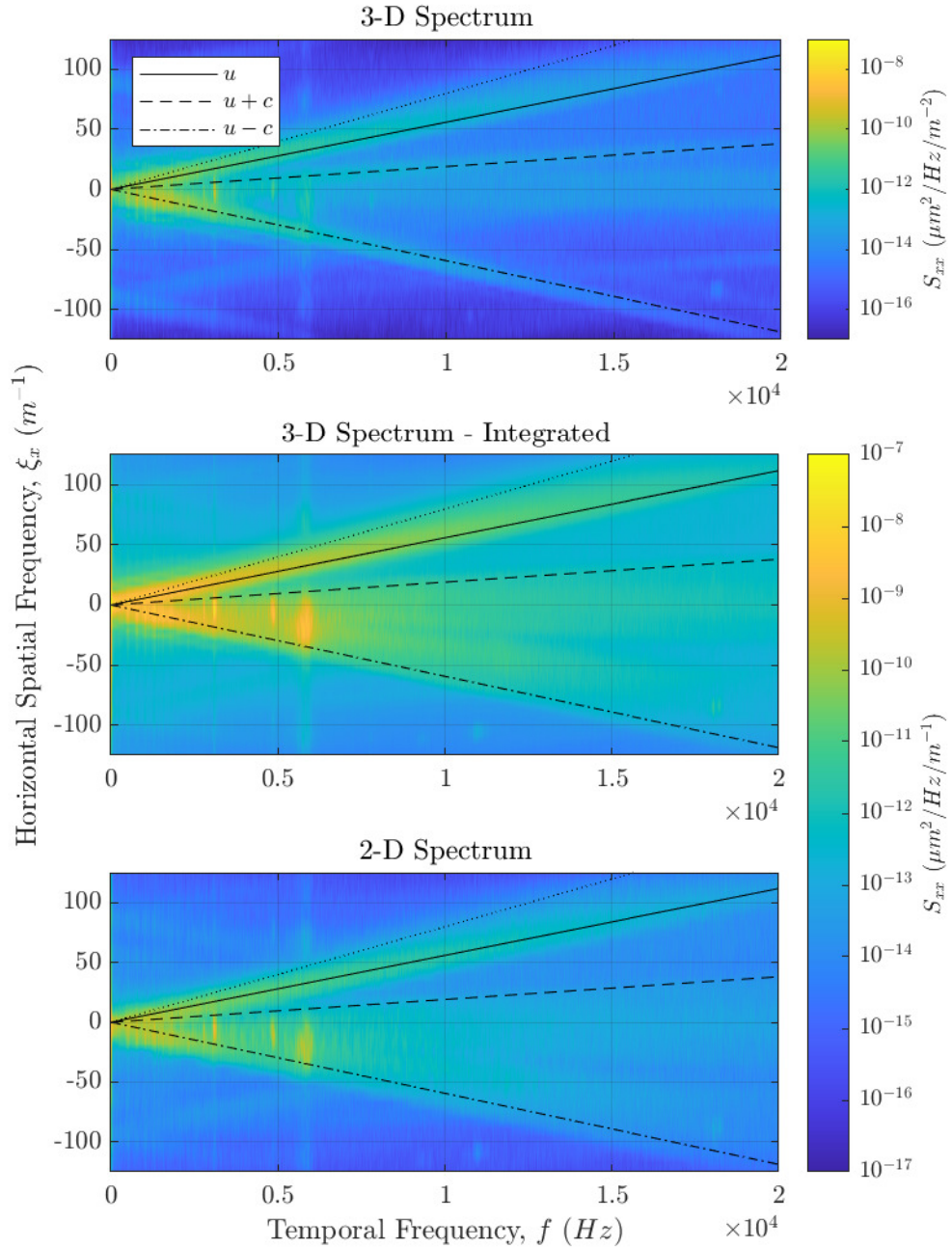


Figure 4.2. Horizontal moving optical disturbances comparison. The top plot shows a slice of the three-dimensional spectrum focusing on the plane waves that are traveling in the horizontal direction. The middle plot is a recreation of the two-dimensional spectrum by integrating through the the vertical spatial-frequencies. The bottom plot is the two-dimensional spectrum.

spectrum. The bottom plots shows the two-dimensional spectral plot that was previously shown in Figure 4.1 but this time with a linear temporal-frequency axis. Both of the two-dimensional spectrum whether directly computed or integrated show a significant increase in the signal content between the acoustic lines ($u \pm c$).

The three-dimensional spectral slice shows signal at the same limits characteristic velocity limits of the free-stream velocity, u , and the acoustic lines, $u \pm c$, as the two-dimensional spectrum of signal along with some signal laying along the temporal-frequency axis at $\xi_y = 0 \text{ m}^{-1}$. This signal represents a collection of stationary modes at each temporal-frequency. If this were a flow-related phenomenon the velocity of the disturbance according to Equation 4.4 would be near infinity; as such, it is more likely caused by mechanical vibration of the wind tunnel and components of the optical measurement system. On the three-dimensional spectrum plot there are signals that run parallel to u and $u - c$ that do not emanate origin but from $\xi_x \approx \pm 80 \text{ m}^{-1}$ that show the assumed velocity is not always valid. I can't think of a good explanation for these other than some mean lensing feature that is both convecting and traveling at $u - c$ and maybe $u + c$. Could be a ghost beam at a different magnification. There is also an aliased signal that runs parallel to $u + c$ starting at $\xi_x \approx -50 \text{ m}^{-1}$ and decaying towards the left. Aliased signals are due to the sample rate, either spatial or temporal, being to low.

The middle plot of Figure 4.2 shows the integrated spectrum through vertical spatial-frequency axis which effectively recreates the two-dimensional spectrum plot. A reduced order spectrum can be calculated by

$$S_{xx}^{n-1} = \int S_{xx}^n df_s^m, \quad (4.18)$$

where S_{xx}^n is the n-dimensional spectrum and df_s^m is the differential frequency in the m -th dimension. This can also be shown in Figure 4.3. While the integrated signal over estimated the spectrum going from three-dimensions to two in Figure 4.2, it under estimated the spectrum going from two to one dimensions. Unfortunately, due to the limited number of spatial sample points and the large dynamic range of the signal, this integrated value can contain a significant of error.

Due to the the signal being relatively sparse, a reduced order spectrum can be estimated by

$$S_{xx}^{n-1} \approx \max(S_{xx}^n, m) f_s^m, \quad (4.19)$$

where $\max(S_{xx}^n, m)$ is the maximum value of the spectrum along dimension m and f_s^m is the sample rate for that dimension. The calculated temporal power spectrum from the two-dimensional spec-

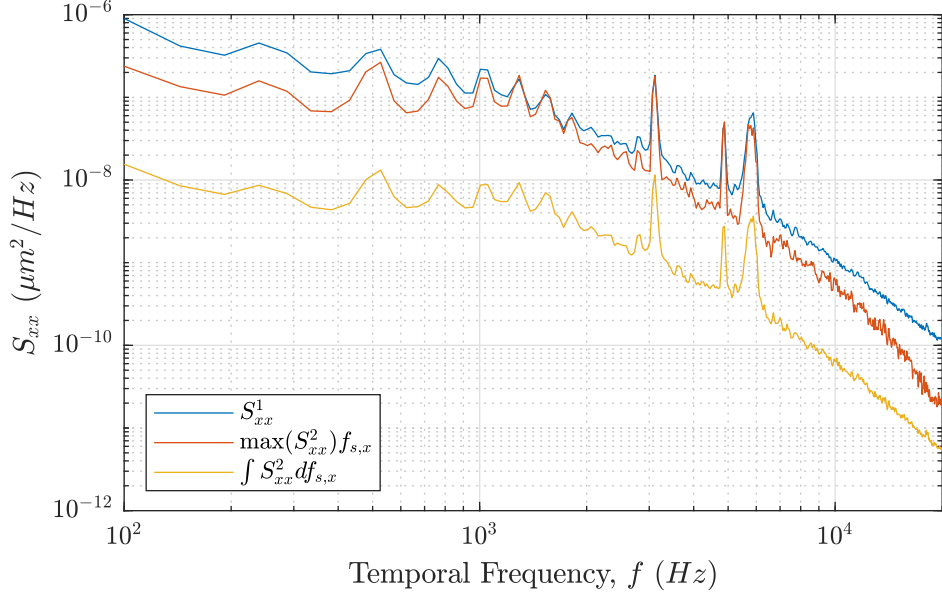


Figure 4.3. Recovery of time-based power spectrum from two-dimensional spectral estimate.

trum using the maximum value is a good estimation at the center of the frequency range but has some additional decay at both low and high frequencies. The calculated reduced order spectrum appears to follow the functional form of actual spectrum but with a significant offset.

4.4.1 2-D Slices of the Multidimensional Spectral Estimation

The full multidimensional spectrum contains information of flow features that are not only moving in the horizontal direction as the two-dimensional dispersion showed but also in every direction of the two-dimensional optical wavefront. Figure 4.4 shows two-dimensional slices of the full spectrum that on the top show the horizontal (stream wise) moving disturbances at $\xi_y = 0 \text{ m}^{-1}$ and on the bottom show the vertical (cross-stream) moving disturbances at $\xi_x = 0 \text{ m}^{-1}$. Since the wavelength is $\lambda = 1/\xi$, the waves that make up the disturbances shown in these slices are plane waves that are traveling solely in the these directions.

The top plot shows the two-dimensional spectrum for horizontally moving optical disturbances that was been shown previously. There are three major flow-related structures that can be observed. The flow-related structure that lays along u is caused by the boundary layers on both walls of the wind tunnel. It can be seen that the boundary-layer signal has a peak at the free-stream velocity, u , and has a slight decay as the velocity decreases towards the dotted line of $0.7u$ with a sharp decay as

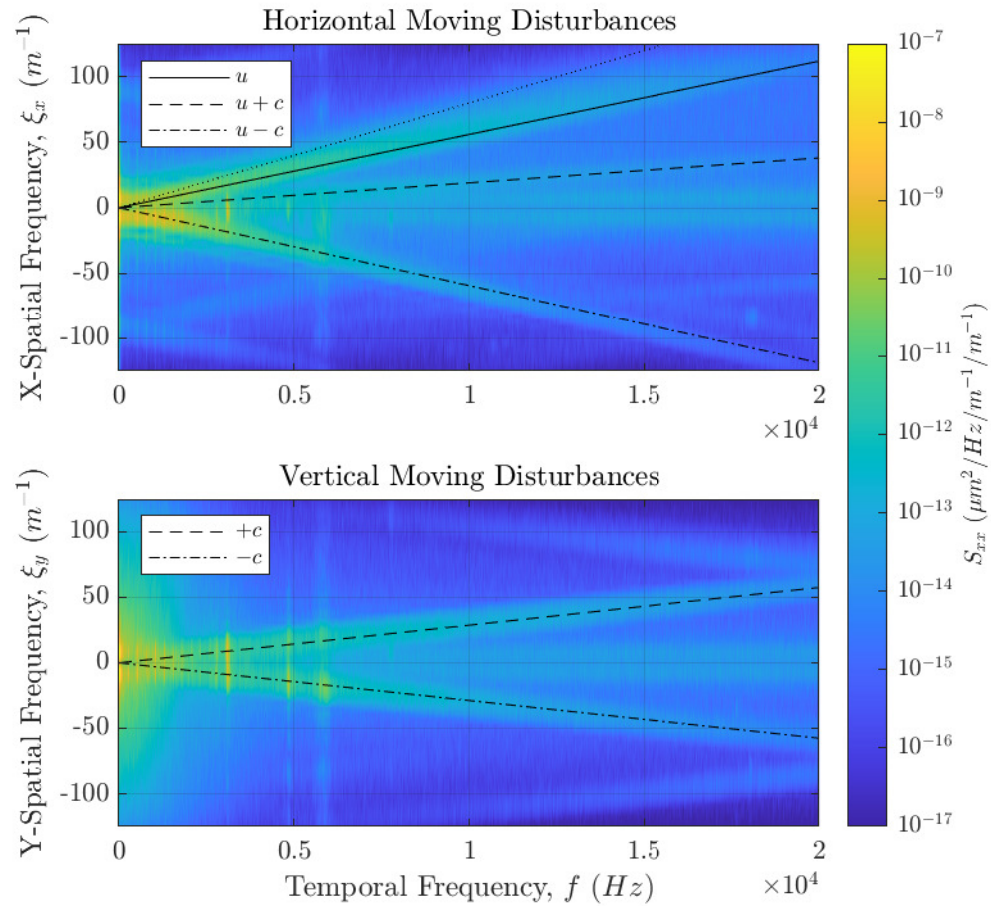


Figure 4.4. Horizontal and vertical moving optical disturbances. This is the same data as presented in Figure 4.1 but after calculating the full three-dimensional spectral estimate. These optical disturbances are plane waves that are traveling solely in their respective directions.

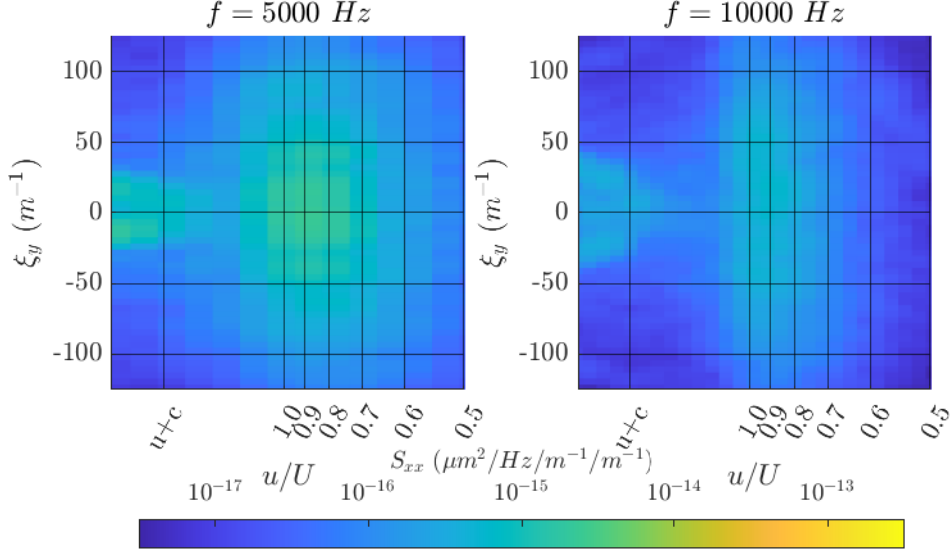


Figure 4.5. Temporal-frequency slices at 5 and 10 kHz with the various horizontal velocities labeled.

the velocity increases. While the boundary layer velocity has typically be reported as approximately $0.83u$ [20], this data shows the boundary layer velocity has a range of velocities at each given frequency in which the peak velocity component has some dependence on the temporal frequency. This can be more clearly seen in two temporal-frequency slice in Figure 4.5. Here the horizontal spatial-frequency has been replaced with the normalized horizontal velocity. The significant decay of the signal as the speed increases above the free-stream velocity there is a gradual decay as the speed decreases. There is also additional signal decay as the absolute value of the vertical spatial-frequency increases. The velocity of this boundary layer optical disturbance will be measured in Chapter 6 using a velocity filter to show a mean velocity of $0.85u$, which is near the generally accepted value of $0.83u$ [20].

The other two major flow-related structures in Figure 4.4 are related to acoustic signals traveling in both directions through the wind-tunnel, denoted by the dashed and dot-dash lines in the figure. The downstream-traveling acoustic wave, $u + c$, has a low signal power than the upstream-traveling acoustic wave, $u - c$. The likely explanation for this difference in signal power is that most of the acoustic energy in the wind tunnel is generated by the fan which propagates upstream and downstream within the wind-tunnel ducting. However, sound waves that move in the flow direction have their wavelength stretched as the flow is accelerated into the test-section contraction, while

sound waves moving against the flow have their wavelength contracted. Hence the downstream-traveling waves have a longer wavelength as they pass through the measurement beam and thus more of the optical signal from the downstream-travelling waves is filtered out due to aperture filtering [53]. At low temporal-frequencies, the blade-passing frequency (520 Hz) and its associated harmonics appear as vertical lines with regular spacing in Figure 4.4.

The two main features on the vertical spectral slice plot on the bottom of Figure 4.4 are the signals moving at the speed of sound ($\pm c$) including some significant aliasing of these signals. These two lines represent acoustic waves that are traveling either straight up or down through the measurement beam. The blade-passing frequency and its harmonics are also visible in the vertical moving wave plots in both directions and have much less broadband spatial content in the vertical direction. Some of the high temporal-frequency narrow-band signals (3, 5, and 6 kHz) contain most of the signal power at the speed of sound lines in the vertical spectral slice plot. These signals has some dependence on the free-stream Mach number (see Figure 4.7). These maybe vibrations originating from the tunnel fan that are currently limiting the top speed of the tunnel; some older optical wavefronts collected in this tunnel under similar measurement conditions do not show these narrow-band signals. Because the portion of these signals with the most power is traveling vertically through the test section instead of steam wise, the tunnel walls maybe excited by the fan and resonating.

The stationary modes that have been discussed previously that lay along the temporal-frequency axis in the horizontal spectral slice plot also appear in the same location in the vertical spectral slice plot. These stationary modes appear the be constant when viewed from either direction and through out time. As a white-noise is generally not physical unless it is bandwidth limited with a falloff of at least $1/f^2$ [4]. Some of these stationary modes are likely cause by vibrations of various optical elements, especially at low temporal-frequencies. At higher temporal-frequencies, the stationary modes maybe related to electronic noise from the high-speed camera, higher order optical noise from the laser, or even numerical error from the processing code.

4.4.2 3-D Representations of Multidimensional Spectral Estimation

While the two-dimensional slices are fairly informative, particularly when it comes to signal strength of various flow structures and their velocities, a three-dimensional plot allows better visualization of the overall flow structures although some details are lost because typically only one power level can be plotted at a time. The same data that has been previously shown in two-dimensional form, is depicted in Figure 4.6 as an isosurface with a power of $10^{-14} \mu\text{m}^2/\text{Hz}/\text{m}^{-1}/\text{m}^{-1}$ and

shown from four different views. This particular isosurface encompasses approximately 99.9% of the power of the optical disturbances. The largest feature is the boundary layer which resembles an ellipsoidal plane that is tilted in the $f - \xi_s$ plane. The other main feature is the acoustic signal which appears as a cone which is slightly tilted in the direction of upstream-moving disturbances. The acoustic signal separates into several spikes at high temporal frequencies some of which are constructive interference from aliased signal ($\xi_x \approx 25 \text{ m}^{-1}$, $\xi_y \approx \pm 60 \text{ m}^{-1}$, and $f \approx 20 \text{ kHz}$) which is better visualized in the 20 kHz temporal-frequency spectral slice in Figure 4.5. There may also be a small number of dominant duct modes at these high temporal-frequencies. The last feature is the stationary modes which appears as the cylindrical structure along the center of the plot (near zero spatial-frequency in x and y), which have a near constant shape and magnitude through all temporal-frequency ranges.

Figure 4.7 shows two views of an isosurface of the multidimensional spectrum over a range of Mach numbers. All of these plots are of an isosurface with the same power as used in Figure 4.6. The stationary modes seems to be constant throughout the range of Mach numbers indicating that they are most likely not flow related. The boundary layer signal increases in power significantly as the Mach number is increased while also the slope and thus the velocity is significantly increased as well. As shown in [20], the aero-optical OPD_{RMS} of the flat-plate boundary layer on the walls of the wind tunnel is expected to vary according to

$$\text{OPD}_{\text{RMS}} = BK_{GD}\rho_\infty M^2 \delta \sqrt{C_f} G(M). \quad (4.20)$$

Hence the significant increase in the power of the boundary-layer spectrum with Mach number that can be observed in Figure 4.7 is expected based on the M^2 dependence in Equation 4.20. The increase in slope of the boundary-layer signal is also expected, and is caused by the increase in the convection speed of the boundary-layer aero-optical disturbances as the free-stream Mach number increases. The acoustic signal sees some interesting evolution as well. Along with the strength greatly increasing with Mach number, the slope of the upstream traveling disturbances decreases significantly while the downstream moving acoustic disturbances do not see much change other than an increase in signal strength.

As the angle of the optical beam changes as it looks through the test section the horizontal spatial-frequency goes from measuring only the axial component of the optical disturbance to measuring a combination of the axial and span wise component. This can be seen in Figure 4.8 with the same isosurface value as shown in previous figures and at a Mach number of 0.5. The 90° case

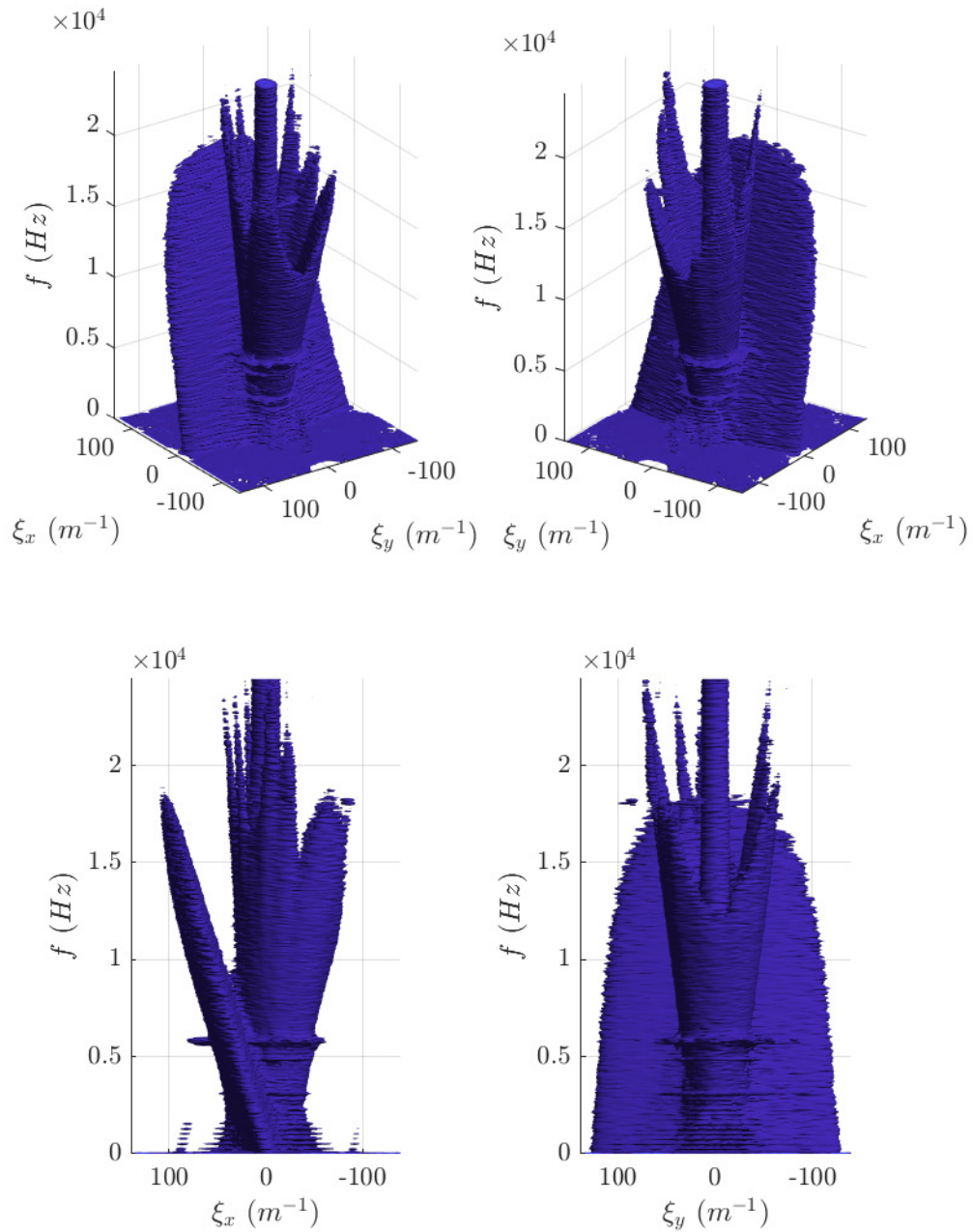


Figure 4.6. Three-dimensional view of the multidimensional spectral plot showing an isosurface at a power of $10^{-14} \mu\text{m}^2/\text{Hz}/\text{m}^{-1}/\text{m}^{-1}$. The isosurface encompasses 99.9% of the power of the wavefront.

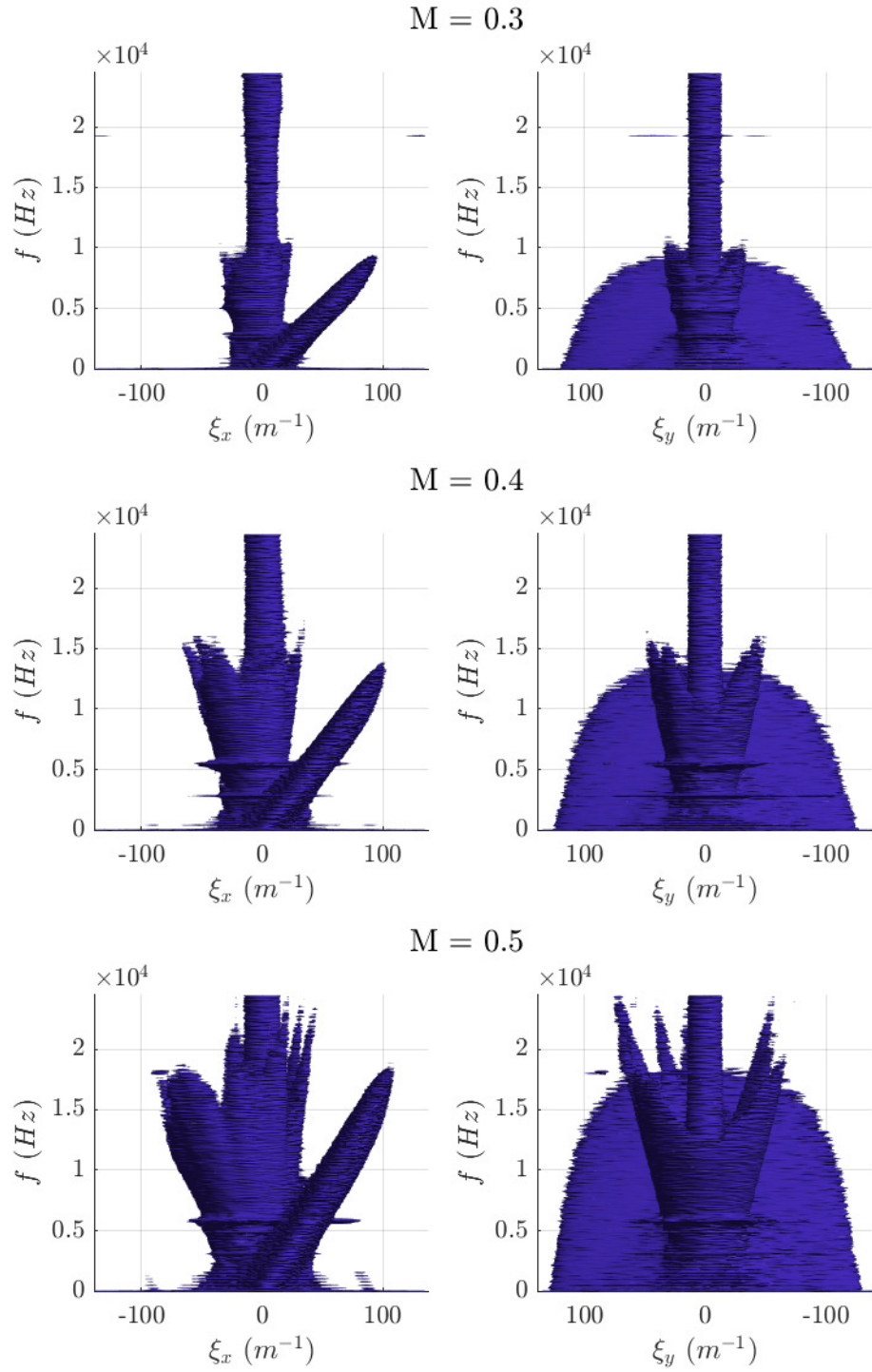


Figure 4.7. Multidimensional spectral estimate isosurfaces as the Mach number increased from 0.3 to 0.5. The isosurfaces are all shown at a power of $10^{-14} \mu\text{m}^2/\text{Hz}/\text{m}^{-1}/\text{m}^{-1}$ and all encompass 99.9% of the wavefront power.

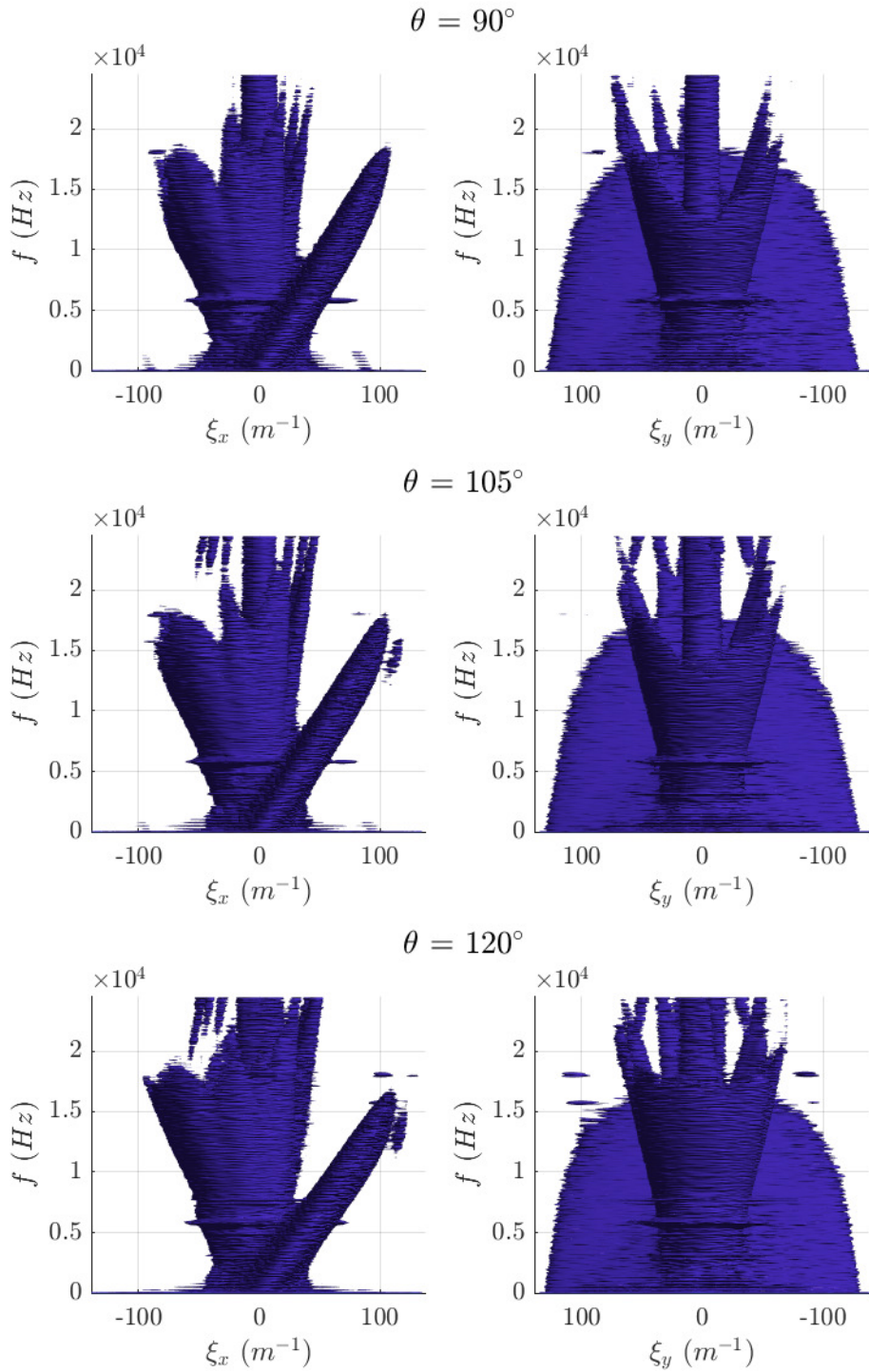


Figure 4.8. Multidimensional spectral estimate isosurfaces of different viewing angles through the test section at a Mach number of 0.5. The isosurfaces are all shown at a power of $10^{-14} \mu m^2/Hz/m^{-1}/m^{-1}$ and all encompass 99.9% of the wavefront power.

has been shown previously and the vertical component of the optical disturbance sees little change as the viewing angle is increase except a small reduction in the boundary layer signal and some additional signal at the high temporal-frequencies in the acoustic cone. As the angle is increased the side of the acoustic cone traveling in the direction of flow is significantly in power, with a large amount of the signal being aliased into the upstream-traveling side as ‘stalactites’ as odd angles. The upstream-traveling acoustic signal is also increased in power but to a lesser extent. The stationary mode pillar experiences some change as well as the viewing angle hits 120° and is stretched in the horizontal direction. The effective velocity of the optical disturbances is reduced for the disturbances traveling in the same direction as the flow and increased for the disturbances traveling in the opposite direction.

While these three-dimensional isosurfaces offer some significant insight into the overall structure of the various optical disturbances they do not show how the spectral inside of the isosurface is distributed. Views inside of the isosurface of the horizontal and vertical plane waves were shown in Figure 4.4 while Figure 4.9 shows slices at various temporal-frequencies. The temporal-frequencies spectral slices shown are at: 0 Hz, the blade-passing frequency at 517 Hz, the second harmonic of the blade-passing frequency at 1551 Hz, and additional slices at 5, 10, and 20 kHz. The slice at 0 Hz temporal frequency shows the spatial frequencies of the wavefront disturbance that does not change with time. This temporally constant wavefront disturbance is typically called the “mean lensing” component of the wavefront measurement, since it has an effect similar to a lens placed in the beam. The mean lensing slice at 0 Hz shows a mostly axisymmetric pattern with most of its power concentrated at low spatial frequencies. There appear to be the occasional spike radiating out from the center, most noticeably in line with the boundary layer signal.

The next four slices, for $f=517.1$ Hz to 10 kHz, show a vertical line associated with the boundary layers aero-optical disturbance, which progressively moves towards positive x-spatial frequencies with increasing frequency. The boundary-layer disturbance appears to be rotated slightly counter-clockwise indicating that the interrogation beam is slightly rotated between the test section and the wavefront sensor. The boundary layer signals at the lower temporal-frequencies appear to have equal decay in both the positive and negative ξ_x directions while at the higher frequencies, the decay is much more gradual in the positive ξ_x direction. This could be indicative of the lower temporal-frequency disturbances in the boundary layer typically traveling at a more uniform speed very near the free-stream velocity likely being either in the outer boundary layer or free-stream tunnel turbulence. The higher temporal-frequency disturbances seem to have a much wider range

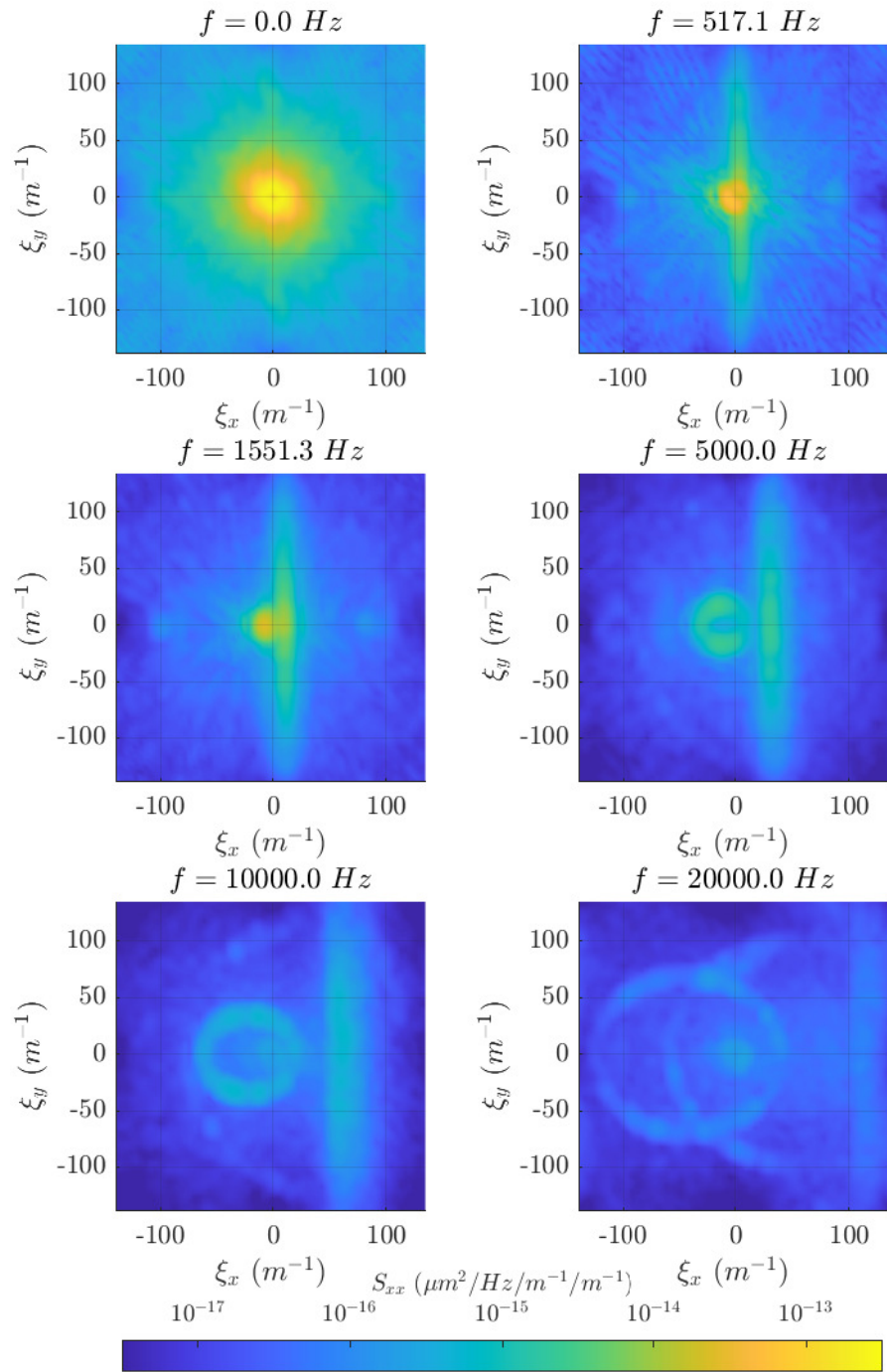


Figure 4.9. Multidimensional spectral estimate slices at various temporal-frequencies.

of velocities that approach the free-stream velocity and are likely small structures that reside in different parts of the boundary layer and hence travel with a wide range of convection velocities.

The acoustic disturbances show an interesting evolution as the temporal-frequency increases. At low temporal-frequencies, the acoustic disturbances are concentrated near zero spatial frequency and with strong power. At high temporal-frequencies the acoustic disturbances appear as elliptically shaped rings. At 20 kHz, there are two elliptical shapes that are easily identifiable, the smaller one is the signal that is actually present at that frequency while the other one is aliased data due to the limited temporal sample rate. There is constructive interference where the two acoustic ring intersect. The 10 kHz slice also shows a small amount of acoustic aliasing. Both the 10 and 20 kHz acoustic rings show some non-uniform signal power throughout the circumference which are also visible in the three-dimensional views as the spikes at the high temporal-frequencies.

4.4.3 Acoustic Cone

The shape of the acoustic cone can be visualized by plotting the relationship between the temporal frequency and the vertical and axial wavenumbers for a beam going through a duct at 90° . Figure 4.10 shows the acoustic cone mode lines for a small set of duct modes at various Mach numbers for a duct that is 1 meter square. The cross-sectional wavenumbers are $k_x = m\pi/l_x$ and $k_y = n\pi/l_y$ with the vertical spacial-frequency, $\xi_y = k_y/2\pi$. The horizontal spacial-frequency is related to the axial wavenumbers, Equation 2.30, for sound traveling upstream or downstream.

The plot on the left of Figure 4.10 shows the acoustic cone when $m = 0$ and $n \in [0, 3]$ at Mach numbers of 0, 0.3, and 0.6. Only shown is the positive vertical spatial-frequency. As the vertical spatial-frequency of a duct-mode varies only with the mode number n each set occupies a distinct plane, $\xi_y = n/2l_y$. Only acoustic cone modal lines representing the cut-on duct modes are shown.

The plot on the right of Figure 4.10 shows the acoustic modal lines at $\xi_y = 0$ for $n = 0$ which fill the inside of the acoustic cone. The Mach number has a far greater impact on the acoustic cone for the waves traveling upstream. As the Mach number increases, the cut-on frequency (minimum value in f) decreases and the horizontal spatial-frequency at the cut-on frequency also decreases. This effect is more pronounced at higher mode numbers. The phase velocity of a downstream-traveling acoustic wave can travel upstream.

It maybe possible to individually resolve the separate acoustic duct modes using optical wavefronts if the spatial frequency resolution where high enough. To measure of the vertical mode number, n , the spatial-frequency resolution would need to be $\Delta\xi_y \geq 1/2l_y$ for a square duct. With

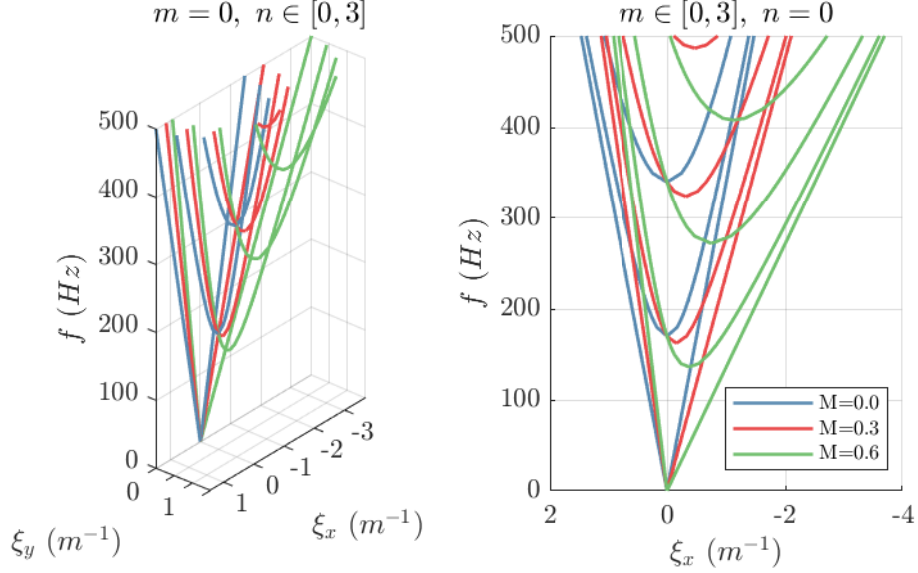


Figure 4.10. Acoustic duct mode lines showing the spatial-frequency location as a function of temporal-frequency, Mach number, and mode number.

a single beam going through the duct perpendicularly, the axial wave number is directly measurable but its sensitivity is diminished as the temporal-frequency is increased. It would be most sensitive to measuring modes that have just been cut-on.

4.4.4 Signal Aliasing

In the spectral slices shown in Figure 4.4, when a signal crosses a plane represented by one of the Nyquist frequencies (positive or negative) it is transposed to the conjugate Nyquist frequency plane and continues on with the same gradient as before. This behavior is illustrated in Figure 4.11 using tiled horizontal and vertical multidimensional spectrum slices. The tiling process for the spectral slices,

$$S_{xx}^{\xi_y=0} = \begin{bmatrix} S_{xx}^{\xi_y=0} & S_{xx}^{\xi_y=0} & S_{xx}^{\xi_y=0} \\ S_{xx}^{\xi_y=0} & S_{xx}^{\xi_y=0} & S_{xx}^{\xi_y=0} \\ S_{xx}^{\xi_y=0} & S_{xx}^{\xi_y=0} & S_{xx}^{\xi_y=0} \end{bmatrix}, \quad (4.21)$$

where $S_{xx}^{\xi_y=0}$ is the spectral slice showing the horizontal moving disturbances at $\xi_y = 0$. The temporal frequency is tiled,

$$f = \begin{bmatrix} f - f_s & f & f + f_s \end{bmatrix}, \quad (4.22)$$

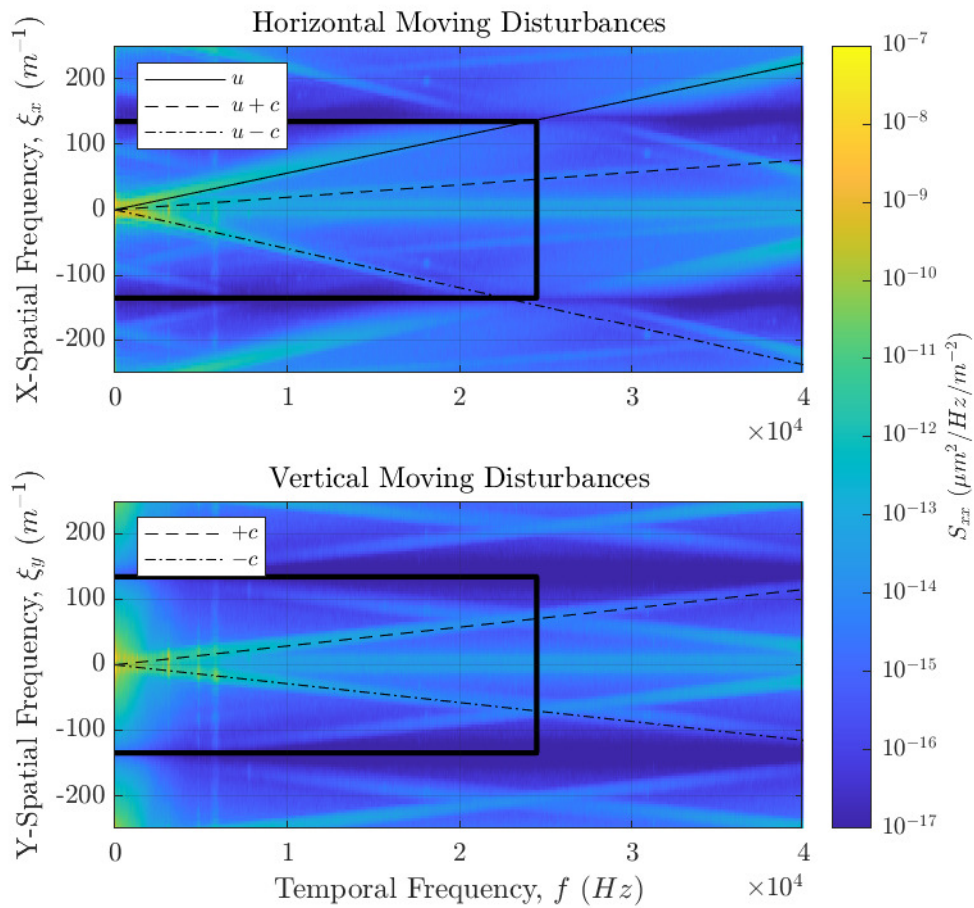


Figure 4.11. Artificially increased temporal sample rate using a dispersion analysis. The black box represents original dispersion plot.

where the other frequencies are similarly tiled. This tiling process could be used on the full multidimensional spectrum with the tiling occurring on each axis. This process has the effect of artificially increasing the sampling rate while also duplicating all of the data many times [32].

In Figure 4.11, the black box represents the original extents of the spectrum along with lines representing the free-stream velocity and the sonic lines. When these characteristic lines are extended past the original sample rate, aliased information becomes more apparent. On the upstream moving disturbance side there is some noticeable aliasing that is present including a significant spike at 18 kHz (-80 m^{-1}) while aliased and about 31 kHz (-200 m^{-1}) when it has been unaliased. As that upstream moving acoustic disturbance crosses the spatial Nyquist frequency, the signal strength drops significantly to local background levels. The boundary layer signal is unfortunately to well aligned with its tiled self for any aliased data to be noticeable. The vertically moving disturbances have some significant temporal aliasing but little to no spatial aliasing.

There maybe some circumstances when aliased data cannot even be identified, such is likely the case for the boundary layer signal shown in the horizontal moving disturbances plot because the signal is directly inline with its aliased self. This may also cause an issue when trying to analyze the original spectrum, particularly at the higher frequencies where the aliased data is sufficiently strong and overlapping the true signal. To avoid this the sample rate velocity,

$$V_s = f/\xi, \quad (4.23)$$

should sufficiently different enough from the disturbance's characteristic velocity. This difference will vary for the depending on the spectral width of the signal. The sample rate velocity of the spectrum in Figure 4.11 is 176.4 m/s, the free-stream velocity is 174.3 m/s and the boundary layer has a significant spectral with to the signal such that it would be difficult to separate the real and aliased signals. The upstream-traveling acoustic wave however is a fairly thin signal that is distinguishable from the aliased signal and it has a characteristic velocity of -173.0 m/s.

4.5 Summary

The use of multidimensional spectral estimation on optical wavefronts can provide significant additional insight to the various components that are being measured, including the desired aero-optical signal but also various forms of noise including sound and vibration. The process of filtering these multidimensional spectra will be discussed in Chapters 6 and 7.

CHAPTER 5

SYNTHETIC WAVEFRONT

In the preceding chapter, the way that wavefront data appears in multidimensional spectra was shown using data acquired in Notre Dame's White Field wind tunnel, for a representative wind-tunnel aero-optical test setup shown in Figure 2.4. The spectra and accompanying discussion showed how individual sources of optical aberration can be identified in the spectra, such as boundary-layer aero-optical signals, acoustic noise sources, mechanical vibration, etc. In following chapters of this dissertation, filtering techniques will be presented for extracting or removing signals or noise sources from wavefront data such as shown in Chapter 3. As a first step towards this objective of developing and examining filtering approaches, this chapter presents methods used to construct a "synthetic" wavefront that contains typical optical and aero-optical signals, which will be used to test and examine different filtering techniques described in Chapter 6.

In order to best understand how some basic filters perform on a set of data, a fully known synthetic wavefront was generated such that all of the various components could be generated separately with the combined product filtered and compared to the synthetic wavefront containing only relevant aero-optical data. This was done by constructing a multidimensional spectrum where each source component was separately generated with parameters that can be modified to alter the output signal as necessary. The resulting multidimensional spectrum could then be used to create the equivalent spatial- and temporally-resolved wavefront signal in the physical domain by inverse Fourier transforming the spectrum.

This synthetic wavefront generation technique produces a qualitative representation that closely matches the measured wavefront but leaves room for improvement in producing a more physically accurate synthetic wavefront. It should be stressed that, although physical models for the spectral behavior are presented for some of the signal components, the shape of the spectrum for each signal component was largely constructed to qualitatively match details observed in the spectra for experimental data such as shown in Chapter 3. This qualitative character to the constructed spectrum for some components should not influence the ability to use the synthesized spectral and wavefront data for examination of filtering approaches, since the constructed data still have the

important behaviors exhibited by measured data.

The synthetic wavefront was generated to approximate the same sampling conditions used to acquire the data first presented in Section 3.4; these sampling conditions are reasonably typical for Shack-Hartmann wavefront measurements at the time of writing. The sample rate was 200 m⁻¹ (i.e. 200 lenslets/m equivalent in the measurement beam) with 64 (2⁶) samples in the spatial dimensions and 30,000 Hz with 8192 (2¹³) samples in the temporal dimension. Figure 5.1 shows the multidimensional spectra estimation of the measured wavefront that was used for the model. The optical wavefront was measured in the University of Notre Dame Whitefield wind tunnel at a Mach number of 0.6 with a 10-inch diameter beam. The beam angle through the test section was 90°.

The signals that were assumed to be statistically independent from one another, such as the boundary layer signal, were converted into dimensional space separately and then summed together, while signals that were assumed to be related to one another, such as the sound and vibration components, were first summed together in frequency space. Figure 5.2 shows the input dispersion plot with each signal component separately colored. The aero-optical signal is shown in red, the stationary modes in blue, duct acoustics in magenta, blade-passing frequency related noise in green, slowly varying mean-lensing in yellow, and background noise in cyan.

5.1 General Spectrum Construction

The general process of developing most of the component signals was to determine an approximate shape, normalize it in the appropriate dimensions, and scale the result by using a function derived from a hyperbola,

$$\frac{\log_{10}(WF) - b}{b^2} - \frac{\xi_{\rho_N}^2}{a^2} = 1, \quad (5.1)$$

such that the signal strength at unity of the normalized radial frequency, $\log_{10}(WF(\xi_{\rho_N} = 1))$, and the limiting slope, a/b , are inputs. This results in the signal strength of the wavefront being

$$\log_{10}(WF) = b - \sqrt{\frac{\xi_{\rho_N}^2}{m^2} + b^2}, \quad (5.2)$$

where

$$b = \frac{1}{2 \log_{10}(WF(\xi_{\rho_N} = 1))} \cdot \left(\log_{10}(WF(\xi_{\rho_N} = 1))^2 - \frac{1}{m^2} \right). \quad (5.3)$$

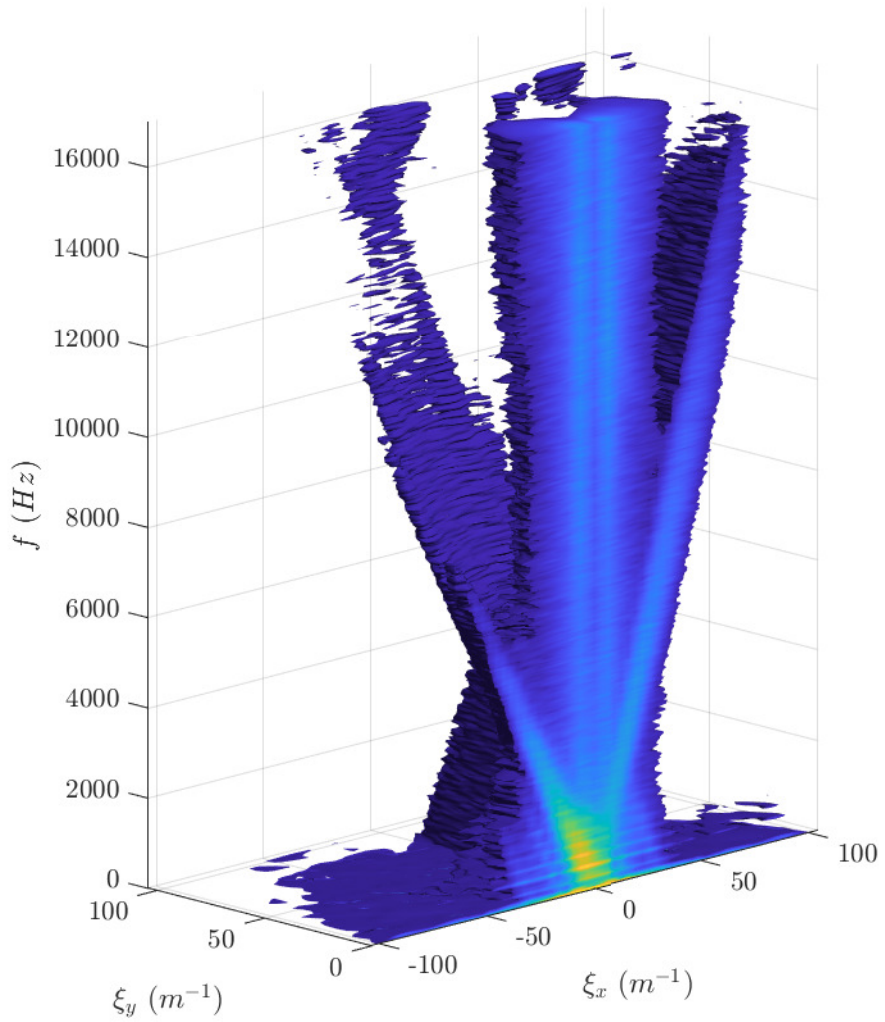


Figure 5.1. Multidimensional spectral estimation that the synthetic wavefront is based on.

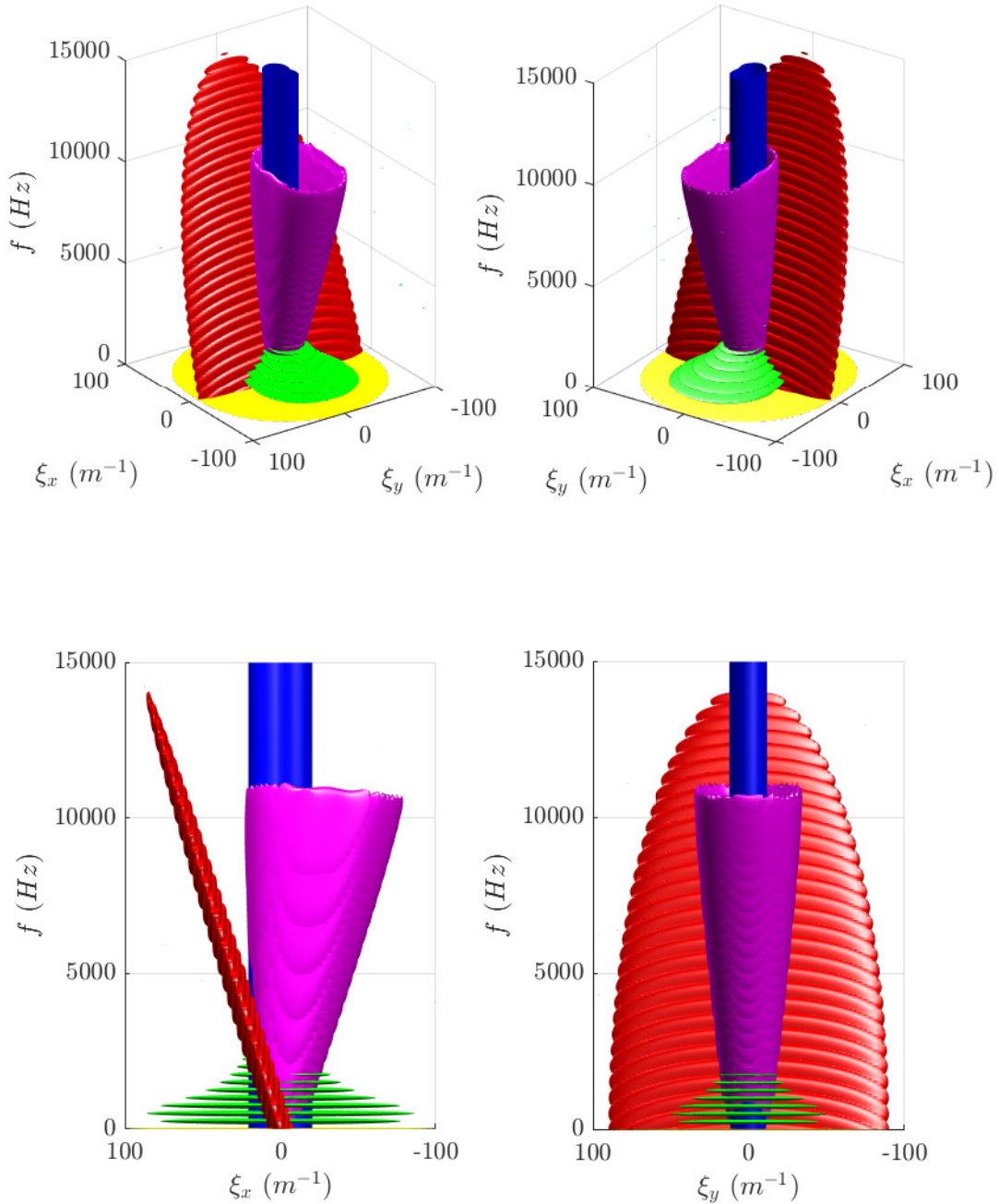


Figure 5.2. Synthetic wavefront input dispersion plot of an aero-optical signal and various signal corruption components. The aero-optical signal is shown in red, the stationary modes in blue, duct acoustics in magenta, blade-passing frequency related corruption in green, slowly varying mean-lensing in yellow, and background in cyan.

TABLE 5.1

VALUES USED IN THE CONSTRUCTION OF THE MULTIDIMENSIONAL
SPECTRUM FOR THE BOUNDARY LAYER SIGNAL

Variable	Value
a_x	8
a_y	90
a_t	175
m	-0.13
u_{BL}	163.2 m/s
$\log_{10}(WF(\xi_{\rho_N} = 1))$	-14.5

5.2 Aero-Optical Signal

The aero-optical signal was generated to approximate an optical beam passing perpendicularly through a test section with boundary layers on each of the test section walls. An ellipsoid was chosen to approximate the boundary-layer signal because it is the simplest shape that best resembles the aero-optical signal in Figure 5.1. This signal was approximated by creating an ellipsoid,

$$\xi_{\rho_N}^2 = (\xi_{x,R}/a_x)^2 + (\xi_{y,R}/a_y)^2 + (f_R/a_t)^2 \quad (5.4)$$

which had been rotated into the plane representing the boundary-layer's dispersion velocity,

$$\begin{bmatrix} \xi_{x,R} \\ \xi_{y,R} \\ f_R \end{bmatrix} = \begin{bmatrix} \cos \theta_u & 0 & \sin \theta_u \\ 0 & 1 & 0 \\ -\sin \theta_u & 0 & \cos \theta_u \end{bmatrix} \begin{bmatrix} \xi_x \\ \xi_y \\ f \end{bmatrix} \quad (5.5)$$

where $\theta_u = \tan^{-1}(-1/u_{BL})$. Equations 5.2 and 5.3 were then used to calculate the multidimensional spectrum of the boundary layer signal. The values used are shown in Table 5.1. In Figure 5.2 the aero-optical signal is shown in red.

TABLE 5.2

VALUES USED IN THE CONSTRUCTION OF THE MULTIDIMENSIONAL
SPECTRUM FOR THE SIGNAL OF THE STATIONARY MODES

Variable	Value
m	-0.175
ξ_{ρ_0}	5
$\log_{10}(WF(\xi_{\rho_N} = 1))$	-14.5

5.3 Stationary Mode Signals

The collection of stationary modes is a temporally constant signal at low spatial frequencies that is often has a cross-section in the plane of spatial-frequencies that is circular. In the particular case that is being modeled, the stationary modes have a cross-section of two circular regions offset along the ξ_x -axis that just overlap one another. A smooth function was chosen to approximate this overlapping circle type stationary mode,

$$\xi_{\rho_N} = \frac{\xi_\rho}{\xi_{\rho_0} \sqrt{10 - 6 \cos(2\xi_\theta + \pi)}}. \quad (5.6)$$

This spectrum for the stationary modes component is shown in blue in Figure 5.2. Table 5.2 shows the values used in generating the spectrum.

5.4 Sound and Vibration Signals

The sound and vibrating component signals are comprised of two parts. The first of these is the blade-passing frequency and its harmonic disturbances (shown in green in Figure 5.2) and the second is the acoustic duct modes (shown in magenta).

5.4.1 Blade-Passing Frequency Disturbance

Like the stationary modes, the blade-passing frequency disturbances were modeled with the same cross-sectional shape as the stationary mode, Equation 5.6, but as narrow-band discs,

$$\xi_{\rho_N}^2 = \frac{\sqrt{\xi_x^2 + (AR\xi_y)^2}}{\xi_{\rho,BPF} \sqrt{10 - 6 \cos(2\xi_\theta + \pi)}} + \left(\frac{f \pm BPFn}{f_T} \right)^2 \quad (5.7)$$

TABLE 5.3

VALUES USED IN THE CONSTRUCTION OF THE MULTIDIMENSIONAL
SPECTRUM FOR THE BLADE-PASSING FREQUENCY DISTURBANCE

Variable	Value
AR	1
BPF	500 Hz
f_c	500 Hz
f_T	100 Hz
m	-0.13
ξ_{ρ_0}	20
$\log_{10}(WF(\xi_{\rho_N} = 1))$	-14

where AR is the aspect ratio of the cross-sectional shape, n is the harmonic number, f_T is the disc thickness, and $\xi_{rho,BPF}$ is

$$\xi_{rho,BPF} = \frac{\xi_{\rho_0}}{\sqrt{1 + \frac{BPFn - BPF}{f_c}}} \quad (5.8)$$

where f_c is the effectively cutoff frequency for modulating the strength of each disc as the harmonic number increased from $n = 0.5$ to $n = 5$ in steps of 0.5. A list of values is shown in Table 5.3.

5.4.2 Acoustic Cone

The acoustic duct mode disturbances form a cone which in the $f - \xi_x$ plane is defined by the lines $u \pm c$, while in the $f - \xi_y$ plane is defined by the speed of sound. At each temporal frequency step an ellipse was defined based on the constraining lines and the distance to that ellipse used to calculate a normalized radial frequency,

$$\xi_{\rho_N}^2 = \frac{\sqrt{(\xi_x - \xi_{x_0})^2 + (\xi_y - \xi_{y_0})^2}}{\sqrt{\xi_{x_a}^2 \cos^2 \xi_\theta + \xi_{y_a}^2 \sin^2 \xi_\theta - 1}} \frac{\sqrt{\xi_{x_a}^2 \cos^2 \xi_\theta + \xi_{y_a}^2 \sin^2 \xi_\theta}}{\xi_{\rho_T}}, \quad (5.9)$$

where ξ_{x_0} and ξ_{y_0} are the midpoint between the sonic lines in the x and y directions as a function of f , ξ_{x_a} and ξ_{y_a} are the distances from the midpoint to the sonic lines as a function of f , and ξ_{ρ_T} is the thickness of the ellipse. The strength of the disturbance was decreased logarithmically as a

TABLE 5.4

VALUES USED IN THE CONSTRUCTION OF THE MULTIDIMENSIONAL
SPECTRUM FOR THE ACOUSTIC CONE DISTURBANCE

Variable	Value
m	-0.3
ξ_{c_x}	115 m^{-1}
ξ_{c_ρ}	200 m^{-1}
ξ_{ρ_T}	8 m^{-1}
$\log_{10}(WF(\xi_{\rho_N} = 1, f = 0))$	-13
$\log_{10}(WF(\xi_{\rho_N} = 1, f = f_s/2))$	-16

function of $|f|$ from $f = 0$ to $f = f_s/2$ with Equation 5.3 becoming,

$$b(f) = \frac{1}{2b_0(f)} \left(b_0^2(f) - \frac{1}{m^2} \right), \quad (5.10)$$

where

$$b_0(f) = \frac{\log_{10}(WF(\xi_{\rho_N} = 1, f = f_s/2)) - \log_{10}(WF(\xi_{\rho_N} = 1, f = 0))}{f_s/2} |f| + \log_{10}(WF(\xi_{\rho_N} = 1, f = f_0)). \quad (5.11)$$

Two low-pass spatial filters (more discussion in Chapter 6) were used to replicate some of the signal attenuation that happens at the low spatial frequencies in the x-direction. First a low-pass filter in ρ was used,

$$WF = WF \sqrt{\frac{1}{1 + \left(\frac{\xi_\rho}{\xi_{c_\rho}}\right)^2}}, \quad (5.12)$$

followed by a low-pass filter in the x-direction,

$$WF = WF \sqrt{\frac{1}{1 + \left(\frac{\xi_x}{\xi_{c_x}}\right)^2}}. \quad (5.13)$$

The values used in creating the spectrum are shown in Table 5.4.

TABLE 5.5

VALUES USED IN THE CONSTRUCTION OF THE MULTIDIMENSIONAL
SPECTRUM FOR THE MEAN-LENSING DISTURBANCE

Variable	Value
AR	0.55
f_T	50 Hz
m	-0.5
ξ_{ρ_0}	25
$\log_{10}(WF(\xi_{\rho_N} = 1))$	-14.5

5.5 Mean-Lensing Signal

The mean lensing part of the optical signal is the integrated effect of steady optical aberrations added by lenses, mirror, windows, etc, in the beam path. The aberrations are effectively random and a physical model cannot be developed for them. The mean-lensing signal (shown in yellow in Figure 5.2) uses same cross-sectional as the blade-passing frequency disturbances and represents the slowly varying spatial disturbance,

$$\xi_{\rho_N}^2 = \frac{\sqrt{\xi_x^2 + (AR\xi_y)^2}}{\xi_{\rho_0} \sqrt{10 - 6 \cos(2\xi_\theta + \pi)}} + \left(\frac{f}{f_T}\right)^2. \quad (5.14)$$

Table 5.5 shows a list of the values used in creating this component of the wavefront signal.

5.6 Background Noise Signal

Background noise in the wavefront data originates from sources which are random in nature. The background noise disturbance (with a few small spots shown in cyan in Figure 5.2) was simulated using normally distributed random noise with a mean noise level, $\mu(\log_{10}(WF)) = -18$, and deviation, $\sigma(\log_{10}(WF)) = 0.75$.

5.7 Synthetic Wavefront Creation

A synthetic signal can be created from a power spectrum by solving for x in Equation 4.5 and using the Inverse Fast Fourier Transform,

$$x(t) = \text{REAL} \left[\text{IFFT} \left\{ \sqrt{S_{xx} \cdot N \cdot f_{samp}} \cdot \exp i\phi \right\} \right], \quad (5.15)$$

where **REAL** is the real component and ϕ is a random set of phases for each point in the measurement space. As shown previously this relation can be extended into n -dimensions,

$$f(\mathbf{x}) = \text{REAL} \left[\text{IFFT}_n \left\{ \sqrt{\mathbf{S}_{\mathbf{xx}} \cdot \prod \vec{N} \cdot \vec{f}_{\text{samp}}} \cdot \exp i\phi \right\} \right]. \quad (5.16)$$

Care should be taken when constructing the random set of phases, as the zero-frequency component has zero phase, $\phi(0,0,0) = 0$, and the phases on either side of it are conjugates of one another, $\phi(\pm\xi_x, \pm\xi_y, \pm f) = -\phi(\mp\xi_x, \mp\xi_y, \mp f)$.

It was assumed that the aero-optical signal, the stationary modes, the background noise, and the sound and vibration combination of modes were statistically independent of one another and, as such, could be separately transformed into physical space. The components of the sound and vibration sources, the blade-passing frequency, the acoustic cone, and the mean-lensing, were assumed to be related to one another and thus were summed together in frequency space prior to being transformed into physical space. Once the separate components were in physical space the total wavefront was obtained by summing up the separate components with the aero-optical signal saved along side the total wavefront. Some frames from the synthetic wavefront are shown in Figure 5.3 with the total wavefront shown on top and the aero-optical only signal shown on the bottom. Flow is from right to left. The aero-optical signal is noticeable to some degree in the total wavefront signal, but can be overpowered by the various noise sources.

5.8 Comparison to Measured Data

A multidimensional spectral plot of the total synthetic wavefront is shown in Figure 5.4. In this view the aero-optical signal is more noticeable but there still remains some significant overlap with the various noise sources. While the mean-lensing component is not as visible in this isosurface, the rest of the dispersion plot in a good representation of the input dispersion plot shown in Figure 5.2. The blade-passing frequency was depicted as symmetric in the synthetic wavefront while measured

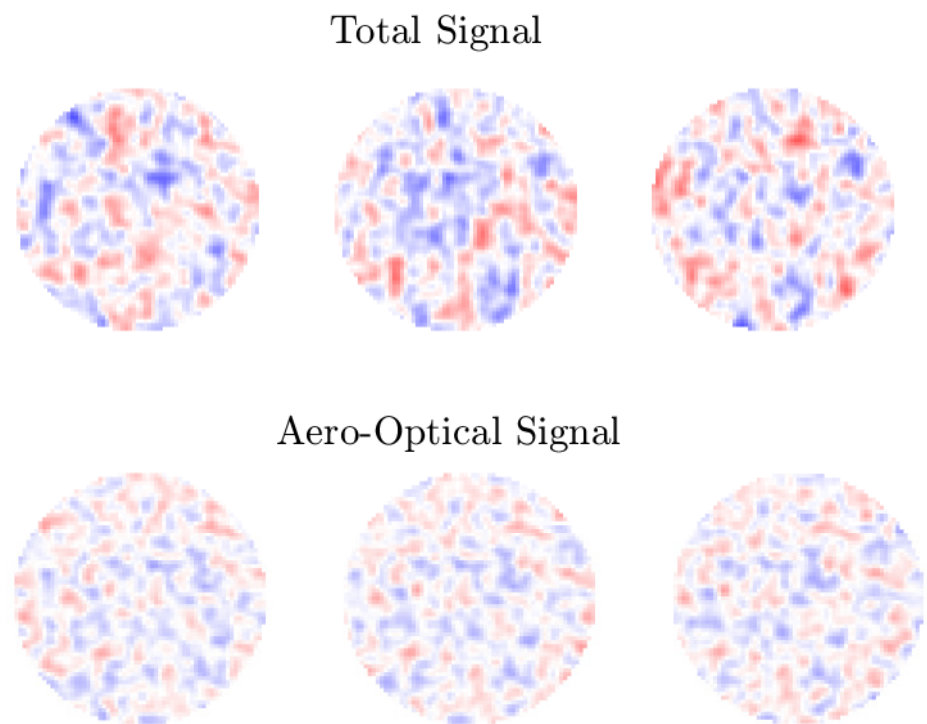


Figure 5.3. Sample frames from the synthetic wavefront with the total wavefront signal on top and the aero-optical only signal bottom. Flow is from right to left.

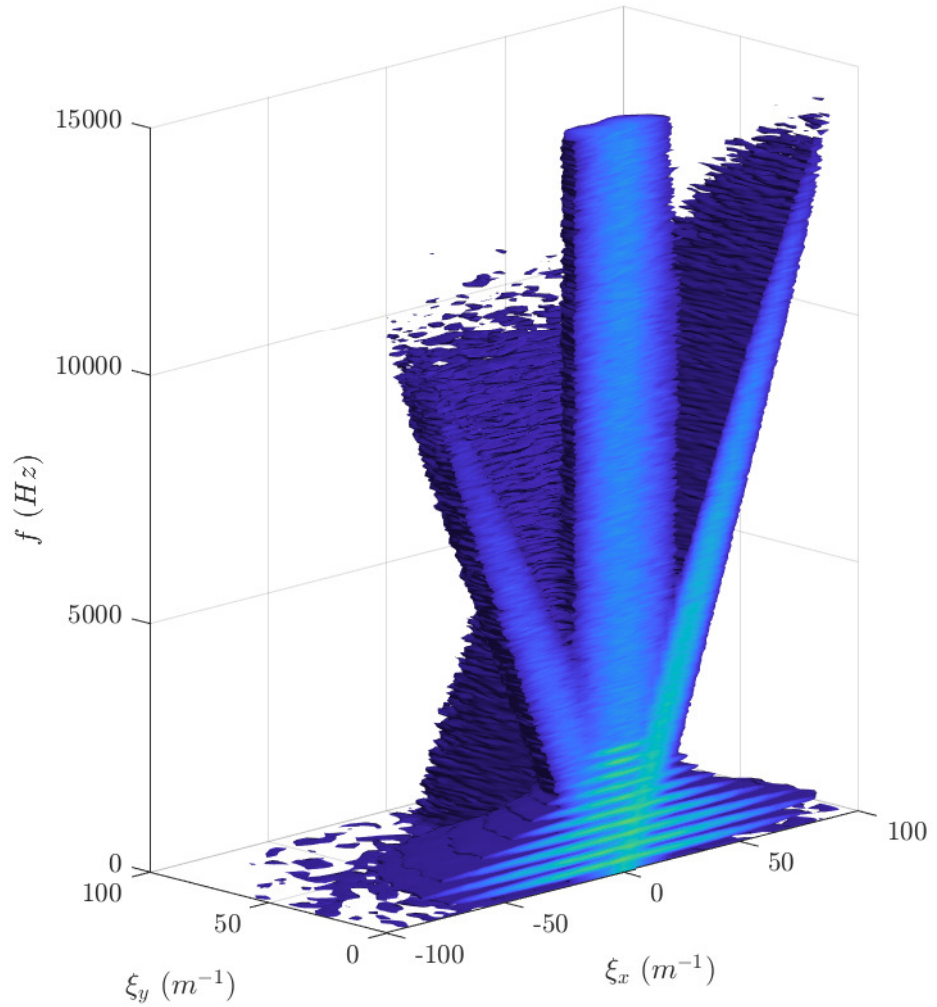


Figure 5.4. Synthetic wavefront output dispersion plot of an aero-optical signal and various signal corruption components.

data (shown in Figure 4.6) shows more signal on the side traveling in the direction of flow. The harmonics of the BPF are more on the upstream traveling side of the dispersion and are a little less pronounced in the measured data. The total synthetic wavefront has a OPD_{RMS} of $0.0112 \pm 0.0006 \mu\text{m}$ with the aero-optical only signal having a OPD_{RMS} of $0.0073 \pm 0.0003 \mu\text{m}$. The measured wavefront presented in Figure 4.6 had a OPD_{RMS} of $0.0874 \pm 0.0263 \mu\text{m}$. The overall OPD_{RMS} of the synthetic wavefront was 12.8% when compared to the measured wavefront indicating that the algorithms used to generate the wavefront are not representative of reality and can provide a future path of research in order to produce more realistic synthetic wavefronts.

CHAPTER 6

SINGLE SENSOR FILTERING TECHNIQUES

Using multidimensional spectral estimates on wavefronts, as shown in Chapter 4, clear differences in source disturbances become evident. When just the wavefront measurement itself is available, digital filters can be used to separate or isolate a single disturbance source or at least minimize the impact from other sources. The digital filters used in this dissertation, use a transfer function, $H(j\omega)$, and are applied in Fourier space. The transfer functions themselves are typically derived in Laplace space, $H(s)$, but because $s = j\omega$ they are valid in Fourier space as well [22]. The transfer function is compromised of two components which attenuate the signal, gain and phase. The filter gain is the magnitude of the transfer function, $G(\omega) = |H(j\omega)|$, while the filter phase is the argument, $\Phi(\omega) = \arg(H(j\omega))$. In the simplest case, the filtered signal is the inverse Fourier transform of the gain multiplied by the Fourier transform of the signal,

$$f_F(\mathbf{x}) = \text{REAL} (\text{IFFT}_n[H(j\omega) \text{FFT}_n\{\mathbf{x}\}]), \quad (6.1)$$

where f is the signal function and f_F is the filtered signal.

6.1 Temporal Filter Methods

The methods presented in this section are based on Butterworth filters but could be extended to other types of filters. The square of the transfer function of a Butterworth filter is [9],

$$|H(j\omega)|^2 = G^2(\omega) = \frac{G_0^2}{1 + \left(\frac{j\omega}{j\omega_c}\right)^{\pm 2n}}, \quad (6.2)$$

where G_0 is the zero-frequency gain, ω_c is the cutoff angular frequency, n is the filter order (number of filters in a series), and \pm represents either a low-pass (+) or high-pass (-) filter. The gain of this filter is

$$G(\omega) = \frac{G_0}{\sqrt{1 + \left(\frac{\omega}{\omega_c}\right)^{\pm 2n}}}. \quad (6.3)$$

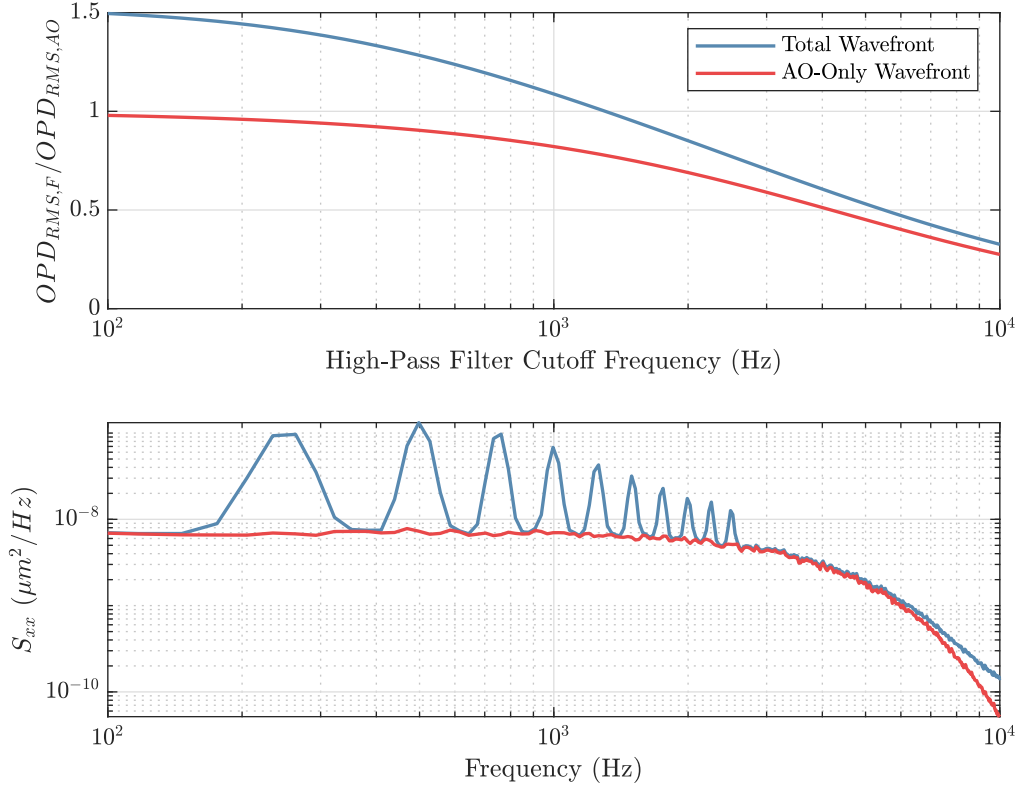


Figure 6.1. The *opdrms* of high-pass temporal filtered wavefronts relative to the *opdrms* of the aero-optical only unfiltered wavefront. Power spectra of both of the simulated wavefront versions.

A band-pass filter can be constructed by placing a low-pass in series with a high-pass filter and a band-stop by placing the two types in parallel.

In many tests, a large portion of the wavefront noise is at low frequencies primarily caused by mechanical vibration. In general, a high-pass filter is useful in temporal space for removing this noise, since in many cases most of the power in the aero-optical signal occurs at higher frequency than the low-frequency mechanical vibration, as shown in Figure 6.1. This figure shows the high-pass filtered OPD_{RMS} of both the total and aero-optical only wavefronts high-pass filters with various cutoff frequencies, relative to that of the unfiltered OPD_{RMS} aero-optical only wavefront. Along with the filter performance plot is the power spectra of both of the simulated wavefront versions. The results in Figure 6.1 were computed for the synthetic wavefront created in Chapter 5. The figure shows how a high-pass filter decreases the energy in the total wavefront and in the actual aero-optical wavefront, as the cutoff frequency increases. The total wavefront ratio crosses unity around 1200 Hz, which is around the third harmonic of the blade-passing frequency in this simulated wavefront.

At this cutoff frequency 75% of the aero-optical signal remains and the remaining signal is made up by the remaining contamination. This approach can provide a computationally inexpensive way of estimating the aero-optical portion of the wavefront for calculations that rely on the OPD_{RMS} of a wavefront. While it is more straightforward to determine a cutoff frequency for this synthetic wavefront since all of the signal components are fully known, a measured wavefront will likely take some knowledge or expectation of the contamination that is present in the measurement in order to select a high-pass filter cutoff frequency.

An example of band-pass and band-stop filtering is shown in Figure 6.2. The figure shows several wavefront frames of the measured data presented in Chapter 3 in the Notre Dame White Field wind tunnel (see Figure 3.16) that is band-stop filtered in the left column and band-pass filtered in the right column. The flow is from right-to-left and the band-pass filtered wavefront clearly shows upstream-moving optical disturbances (moving left-to-right against the flow direction) associated with acoustic duct modes traveling upstream from the fan. On the other hand, the band-stop filtered wavefronts on the left of Figure 6.2 show much slower-moving optical disturbances that are in general moving in the direction of the flow. In particular, the downstream-moving disturbances on the left side of Figure 6.2 have the appearance of boundary-layer aero-optical disturbances, with a scale on the order of the boundary-layer thickness.

Note that for filters that operate in one-dimension, the filters were applied over both positive and negative frequencies to the n-dimensional Fourier transform in order to preserve the direction of travel of the signal. This also allowed several filters to be applied in series with one another without having to perform a Fourier and inverse Fourier transform for each successive filter. Temporal filters are also used in sizing and/or designing adaptive optics systems [21] for example. A low-pass filter with a cutoff at the bandwidth of either a fast-steering or deformable mirror is often used to define the signal that the system needs to reject [59]. A control system may need to have the bandwidth reduced in order to keep a mirror's travel within limits [33], while a high-pass filter would inform designers of the remaining optical aberrations that cannot be corrected.

6.2 Upstream/Downstream Moving

In the preceding section, filters based on temporal frequency only were discussed. In this section, another filtering approach is presented in which signals are identified based on their dispersion velocity. For the filtering of upstream and downstream moving optical disturbances a logistic function

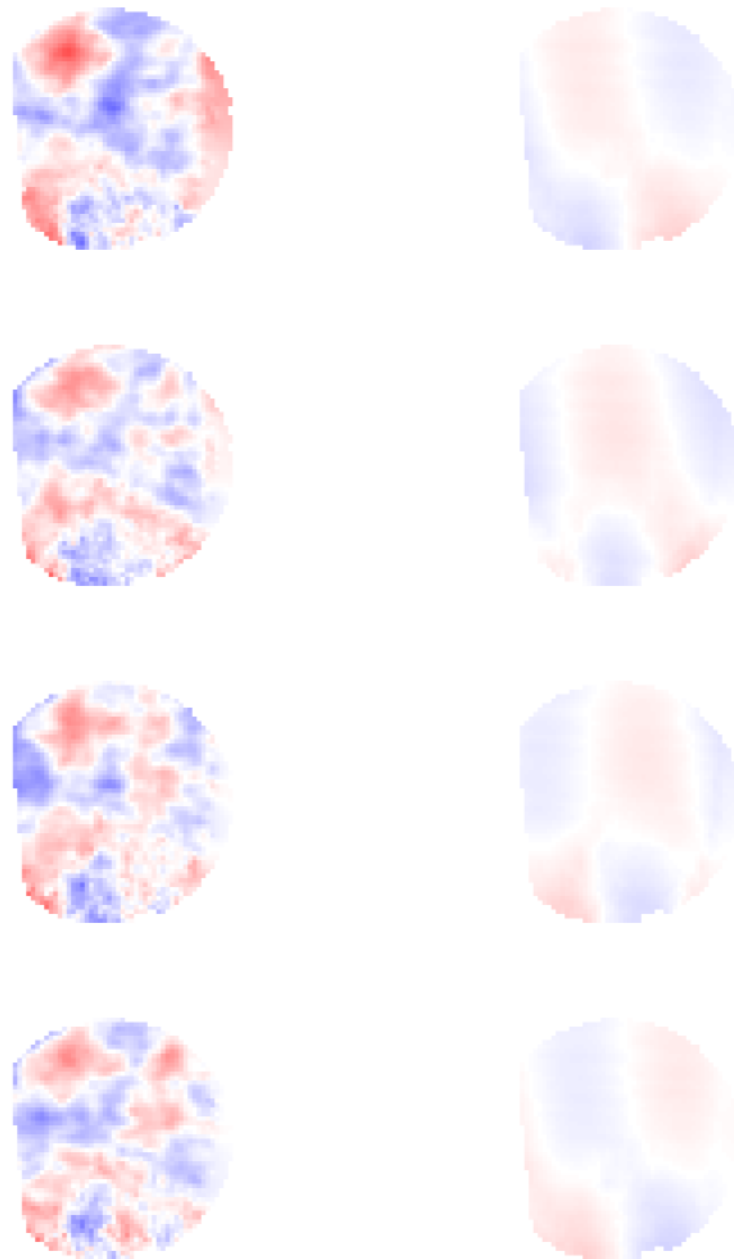


Figure 6.2. Measured wavefronts filtered at the blade-passing frequency (532 ± 10 Hz).
The left column is band-stop filtered while the right is band-pass filtered.

was chosen,

$$f(x) = \frac{1}{1 + \exp\{-kx\}}. \quad (6.4)$$

This function was then expanded into two-dimensions (x and t) with the filter ideally returning a value of one in both the first and third quadrants and zero otherwise, for a filter that acts on disturbances moving in the direction of flow. To accomplish this, the logistic curve in each dimension was scaled and offset to output values between negative one and positive one,

$$G_t(f) = \frac{2}{1 + \exp\{-k_t f\}} - 1 \quad (6.5)$$

and

$$G_x(\xi_x) = \frac{2}{1 + \exp\{\pm k_x \xi_x\}} - 1, \quad (6.6)$$

where \pm determines whether the filter is designed to act on upstream-traveling disturbances (+) or downstream-traveling (-). These two gain functions are then multiplied together and scaled to output values between zero and one,

$$G(\xi_x, f) = \frac{(G_t \cdot G_x) + 1}{2}. \quad (6.7)$$

As the values of k_x and k_t go to infinity an ideal filter is obtained. In a plot of the gain with the horizontal spatial frequency on the x-axis and the temporal frequency on the y-axis, an ideal filter for obtaining only the downstream traveling disturbances would have a gain of one in the first and third quadrants, zero in the second and fourth quadrants, and a value of 1/2 when either frequency is zero. The value of 1/2 would equally split the component of a disturbance that is neither traveling upstream or downstream between the two directions.

The multidimensional spectrum using an ideal downstream moving filter on the synthetic wavefront is shown in Figure 6.3 along side the dispersion of the unfiltered wavefront. All of the upstream traveling disturbances are removed and the disturbances at $\xi_x = 0 \text{ m}^{-1}$ are significantly reduced. Some of the stationary modes remain while only the acoustic and vibration signals that are propagating in the direction of flow remain. The aero-optical signal is clipped slightly at $\xi_x = 0$ due to the spatial width of the signal. The ratio of the time-averaged spatial-RMS of the filtered signal when compared to the aero-optical only signal was 1.24 while the unfiltered ratio was 1.53. When the filter was applied to only the aero-optical signal the ratio was 0.96. This filter method will retain any disturbance that is traveling in the direction of flow. Even with an ideal filter there

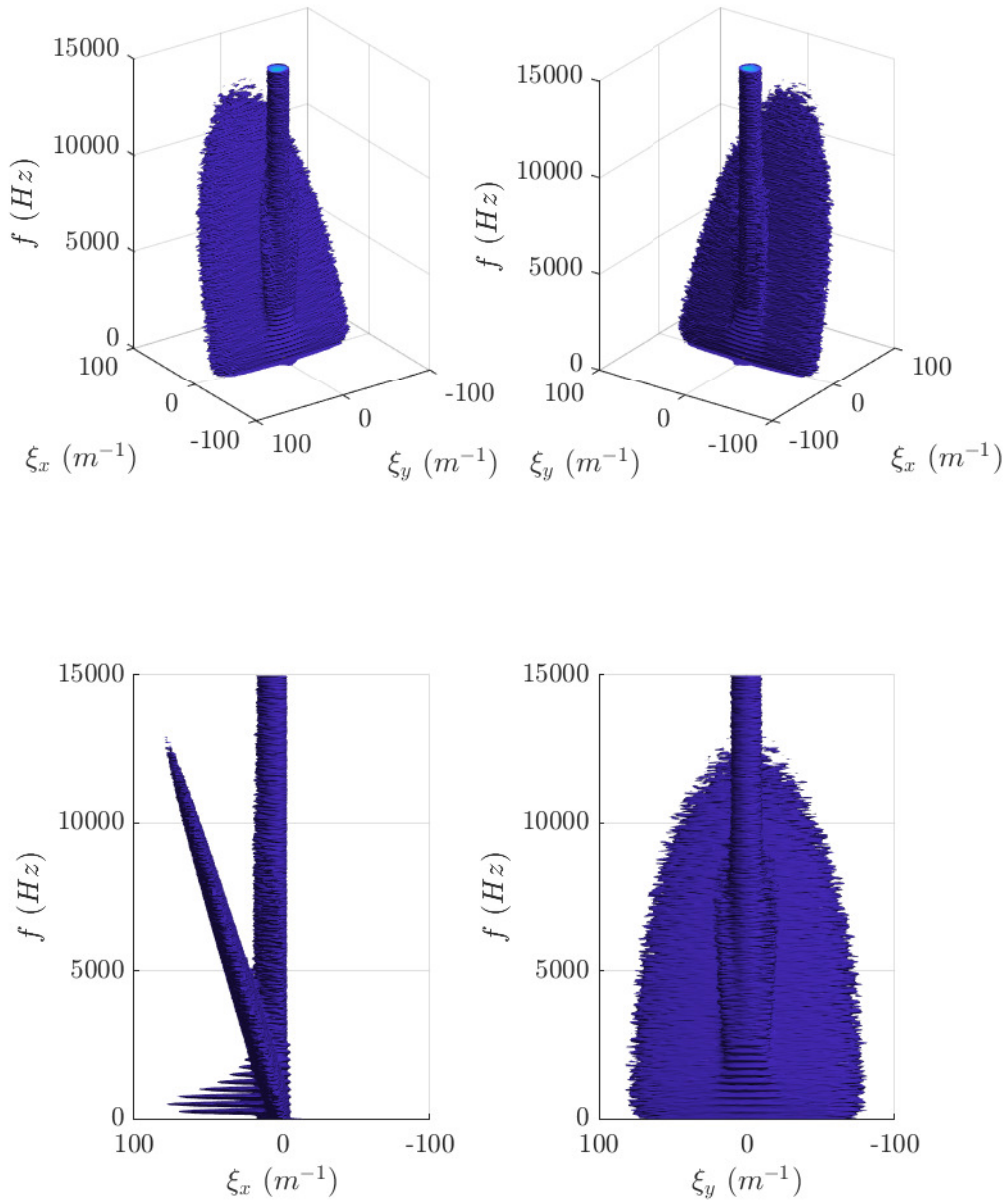


Figure 6.3. Multidimensional spectral isosurface of the synthetic wavefront with a downstream filter in place.

is some slight attenuation of the aero-optical signal due to signal having some spectral width that crosses into upstream-moving portion of the dispersion plot.

6.3 Velocity Filtering

Using dispersion analysis on a multidimensional spectral plot shows that flow structures traveling at a given speed as having a constant slope. A plane in the multidimensional spectral plot can be used to measure a flow structure's velocity in both x and y -directions. The distance from any given point in the multidimensional spectral space to a plane described by the velocities v_x and v_y can be computed by

$$d = \frac{|v_x \xi_x + v_y \xi_y - f|}{\sqrt{v_x^2 + v_y^2 + 1}}. \quad (6.8)$$

Equation 6.8 above can therefore be used to construct a low-pass or high-pass filter that retains only disturbances that are traveling at that velocity, or to exclude those disturbances respectively,

$$G(d) = \frac{1}{\sqrt{1 + \left(\frac{d}{d_c}\right)^{\pm 2n}}}. \quad (6.9)$$

where d_c is the cutoff distance from the theoretical plane defined by the velocities v_x and v_y . Because of difference in the temporal and spatial sample rates of several orders of magnitude, the filter function used frequencies that have been normalized by the sample rate.

A low-pass velocity-filter of the synthetic wavefront is shown in Figure 6.4. The filter was constructed for a v_x at the mean boundary-layer velocity, v_y of zero, d_c of 1/80, and n of 1. The filtered multidimensional spectral plot shows primarily only the aero-optic signal remains with some additional low-frequency content from the blade-passing frequency and harmonic disturbances as well as some stationary and acoustic disturbances. The ratio of the OPD_{RMS} relative to that of the aero-optical only signal went from 1.53 in the unfiltered case to 1.01 in the filtered case. This method can provide a very effective way to quickly estimate the OPD_{RMS} of a convecting aero-optical disturbance in a noise-contaminated wavefront.

Another use of the velocity filter is measuring the speed of a broadband convecting disturbance such as the aero-optical signal of a boundary layer. This can be accomplished by applying a series of low-pass velocity filters to the multidimensional spectrum of the wavefront along with a high-pass

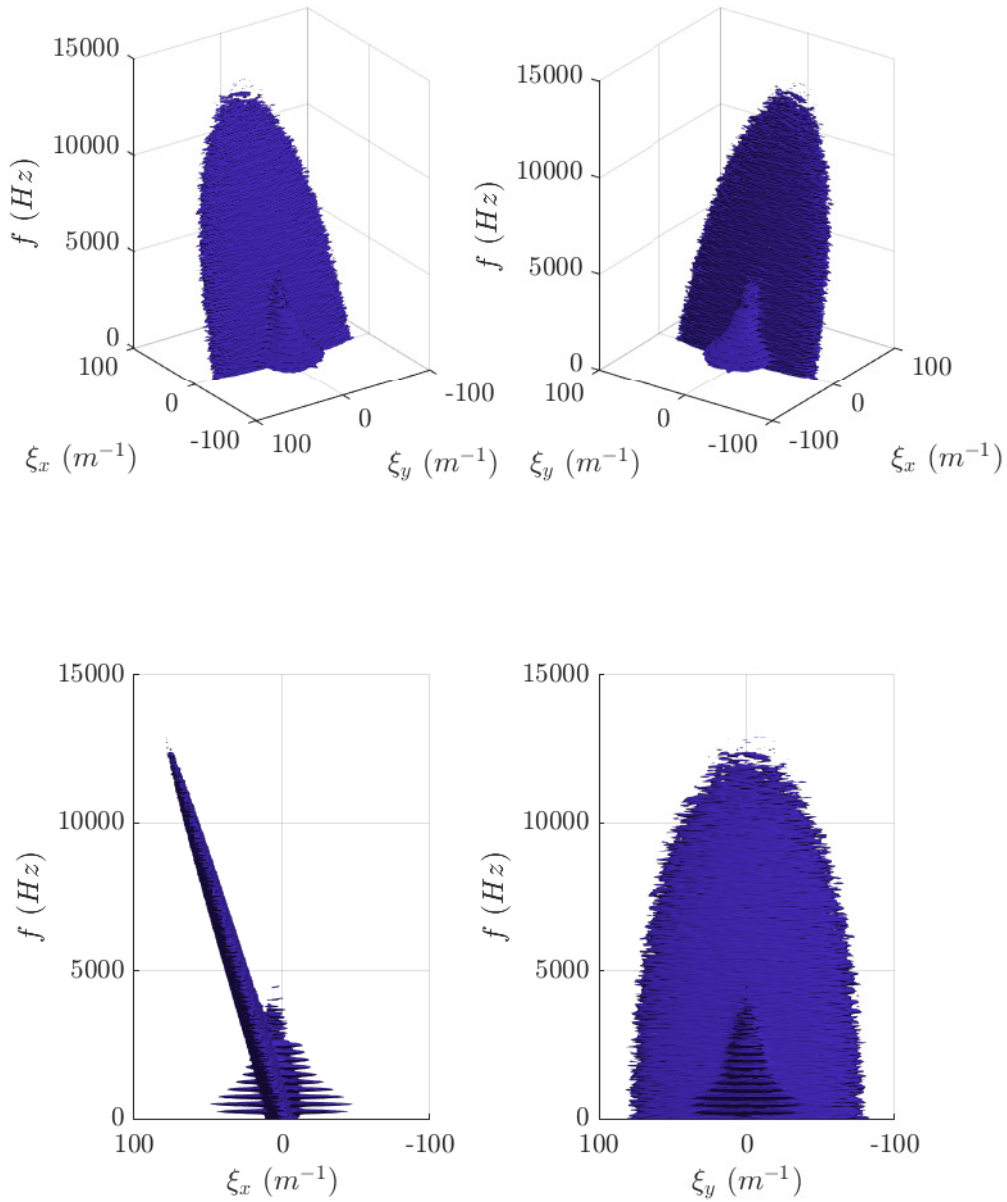


Figure 6.4. Multidimensional spectral isosurface of the synthetic wavefront with a low-pass velocity-filter in place.

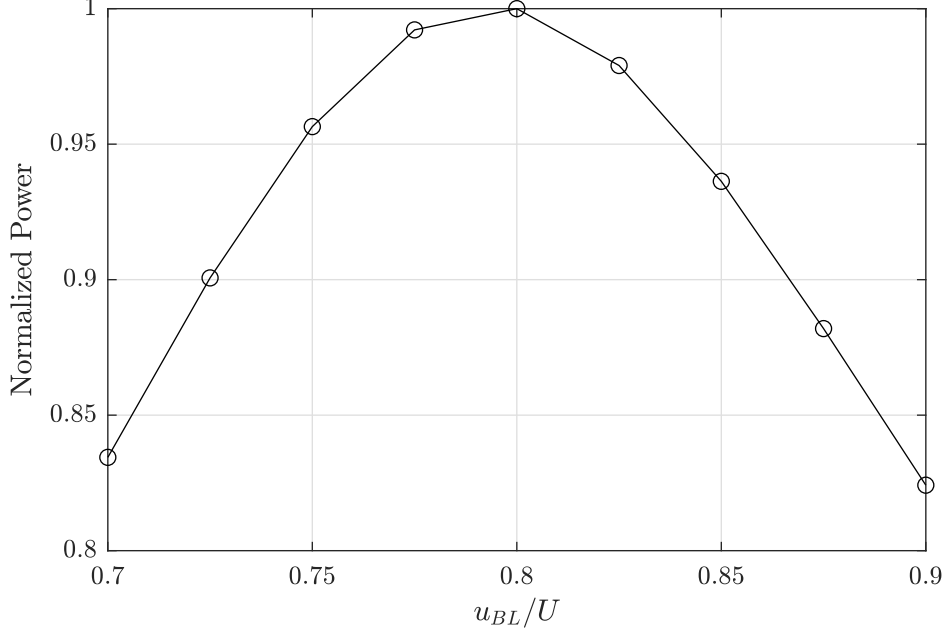


Figure 6.5. Boundary layer velocity measurement of the synthetic wavefront using a combination of a low-pass velocity filter and a high-pass radial frequency filter. The maximum value at $u_{BL}/U = 0.8$ corresponds with the actual value used in the creation of the synthetic wavefront.

radial frequency filter to remove a significant portion of the stationary modes and acoustic cone,

$$S_{xx,f}(\xi_x, \xi_y, f) = S_{xx}(\xi_x, \xi_y, f) G_v^2 G_\rho^2, \quad (6.10)$$

where G_v is the velocity filter and G_ρ is the radial frequency filter. Once the wavefront has been filtered in multidimensional spectral space, the total power remaining can be calculated,

$$P = \sum (S_{xx,f} \prod \vec{f}_s). \quad (6.11)$$

The average convective velocity of the structure will be the maximum power output.

This velocity finding procedure was tested on the synthetic wavefront which had a known boundary-layer mean velocity in Figure 6.5. The low-pass velocity filter used the same parameters as used previously except that v_x was varied and the high-pass radial frequency filter used a cutoff value of 0.1 with an order of 2. The radial frequency, $\xi_\rho = \sqrt{\xi_x^2 + \xi_y^2}$, was normalized by the spatial sampling rate. In this case boundary layer speed was determined to be 163 m/s which corresponds to the design velocity of the synthetic signal of $0.8U$. For signals where the mean-velocity

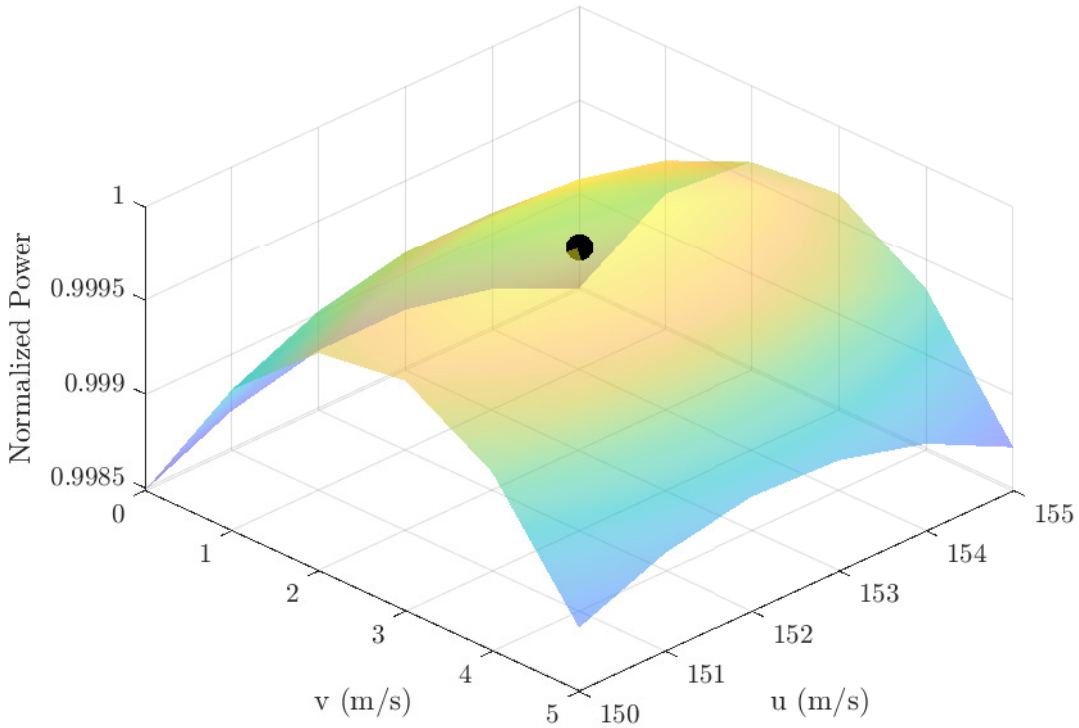


Figure 6.6. Velocity low-pass filter used to determine the mean disturbance velocity of measured data presented in Figure 4.6. The velocity in the x-direction was measured to be 207 m/s and -17 m/s in the y-direction.

component that is not aligned with either the horizontal or vertical axis, both velocity components can be varied as shown in Figure 6.6. In this case the same filtering parameters were used as the synthetic case except the distance cutoff was 1/40 and both v_x and v_y were variables. The velocity was measured using the boundary-layer optical disturbances in the multidimensional spectral plot to be approximately 152 m/s in the x-direction and 3 m/s in the y-direction. The boundary-layer velocity was approximately $0.85U$ when compared to the pitot probe measurement of the free-stream velocity and the overall flow angle of the boundary-layer was approximately 1.1° .

6.4 Baseline Spectrum

If all of the narrow-band temporal signals could be assumed to be measurement contamination that need to be filtered out, a method for calculating the baseline of the spectrum would provide

a simple way of filtering a portion of the signal contamination. For analysis of Raman spectra, the baseline spectra must often be removed [52]. This task is often performed manually which has brought a number of attempts to create automated technique estimate the baseline spectra [39, 51, 52, 61]. One of those techniques [52], a small-window moving average-based fully automated baseline estimation method was used in this research. At each spatial frequency location the baseline spectra was computed along the temporal axis. Figure 6.7, shows the multidimensional spectra of an unfiltered measurement (top left) and its estimated baseline spectra (top right). The bottom plot of the figure shows the spectra along the green line in the two multidimensional spectral plots. The total power of the signal has been reduced by 71% with all of the narrow-band signals removed. A large portion of this signal removal is the very low temporal-frequency components. The blade-passing frequency and harmonics are completely removed but the broadband acoustic duct-modes remain intact. The peak of the boundary-layer signal is reduced slightly as well as the high frequency fluctuations.

6.5 Basic Filter Summary

Three different basic wavefront filters were shown and discussed in this chapter. The temporal filter is most useful when filtering out a frequency band of optical noise. Besides filtering out optical noise, band-pass filters can be used to analyze a wavefront over a narrow-band to examine the optical aberrations at specific frequencies that significantly contribute to the overall optical disturbance; for example, as was shown in Chapter 3, band-pass filters along with an implementation of an acoustic mode-marching method can help determine with some confidence that a narrow-band signal is likely to have been created by the wind-tunnel fan and can be removed.

Filters that separate upstream and downstream-moving disturbances are useful to filter out the optical contamination that comes from acoustic signals that are traveling upstream from a wind-tunnel fan. These filters would also be useful for separating out an aero-optical signal that has a broad range of velocities that can occur in a span wise measurement of a boundary layer. The velocity filter is the most useful for isolating the aero-optical portion of a wavefront measurement given the aero-optical signal has a fairly narrow and constant velocity range. This filter also can be used to measure the speed associated with an optical disturbance in both x and y-directions.

The spectral baseline provides an simple way of removing all of the narrow-band signals with slight attenuation to the broadband signals. The broadband acoustic and stationary modes remain but could be filtered with via other techniques such as using a velocity filter. Narrow-band features

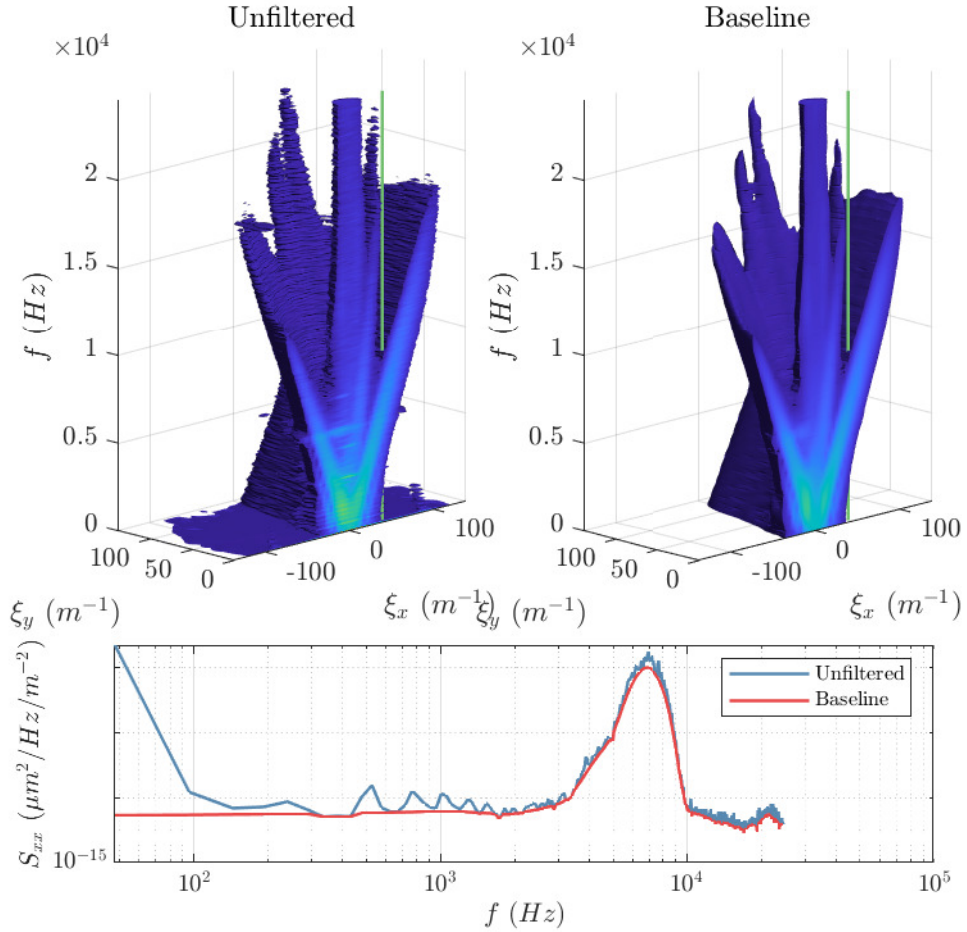


Figure 6.7. Baseline spectrum estimation. The top left plot shows the unfiltered multidimensional spectrum and the baseline spectrum on the top right. The green line in each of these plots represents the location at which the spectra in the bottom plot is shown.

that are not likely to be environmental contamination could be easily added back in.

CHAPTER 7

MULTIPLE SENSOR FILTERING TECHNIQUES

The previous chapter investigated filtering optical wavefront corruption by applying a variety of filters to the wavefront in the multidimensional spectral domain. These techniques involve only data from the optical wavefront itself and user knowledge and experience to obtain filtered data. When additional data is available, such as from microphones or accelerometers, a targeted filter approach becomes possible.

This kind of approach is described in a previous study [31] in which a combination of linear stochastic estimation (LSE) and spectral proper orthogonal decomposition (SPOD) was used to remove vibration related contamination from aero-optical wind-tunnel measurements. This process along with optical tip and tilt removal showed approximately an 85% reduction in the measured OPDRMS by using accelerometer measurements to remove vibration effects from optical wavefront measurements.

7.1 Optical Tip and Tilt

Although they are usually not employed in areo-optical investigations, Zernike polynomials have been traditionally used for modal decomposition of the optical aberrations of an optical system [5]. These polynomials are defined on the unit circle and form a set of orthogonal functions,

$$Z_n^m(\rho, \theta) = R_n^m(\rho) \cos(m\theta) \quad (7.1)$$

where $R_n^m(\rho)$ is the radial basis function and $\cos(m\theta)$ is the angular basis function. For values of $-m$ the angular basis function becomes $\sin(m\theta)$. The radial basis function are developed from Jacobi polynomials but for purposes in this study, only a few simple ones will be used. An optical wavefront can be represented by a summation of Zernike polynomials multiplied by their corresponding coefficients

$$\text{WF} = \sum Z_j a_j. \quad (7.2)$$

The Noll naming scheme is a method of organizing the Zernike polynomials into a single notation of Z_j , along with normalizing each polynomial to have a spatial RMS equal to one [42]. The first three of these using the Noll naming scheme are piston, tip, and tilt. Piston is simply the average OPD value of the wavefront

$$Z_1 = 1. \quad (7.3)$$

Tip and tilt are the best planar fit to the OPD along the x-axis and y-axis respectively where tip is

$$Z_2 = 2\rho \cos \theta, \quad (7.4)$$

and tilt is

$$Z_3 = 2\rho \sin \theta. \quad (7.5)$$

Once the coefficients for these modes are solved for they can be filtered out

$$WF^F = WF - \sum Z_j a_j. \quad (7.6)$$

7.2 LSE-SPOD

The LSE-SPOD technique starts with performing SPOD on the primary data set and then using the Fourier transforms of the additional sensor data to perform a filtering operation. The spectral proper orthogonal decomposition technique is described in detail by Schmidt and Colonius [50]. A schematic of the SPOD algorithm is shown in Figure 7.1. The algorithm begins by separating the original data set, Q , into a number of smaller blocks,

$$Q = \begin{bmatrix} | & | & & | \\ q^{(1)} & q^{(2)} & \dots & q^{(N)} \\ | & | & & | \end{bmatrix}, \quad Q \in \mathbb{C}^{M \times N} \quad (7.7)$$

where M is the total number of degrees of freedom (number of spatial points times the block length in time) and N is the number of blocks. Each block is then Fourier Transformed in the temporal dimension or through all dimensions. Once in the frequency domain the data blocks are then

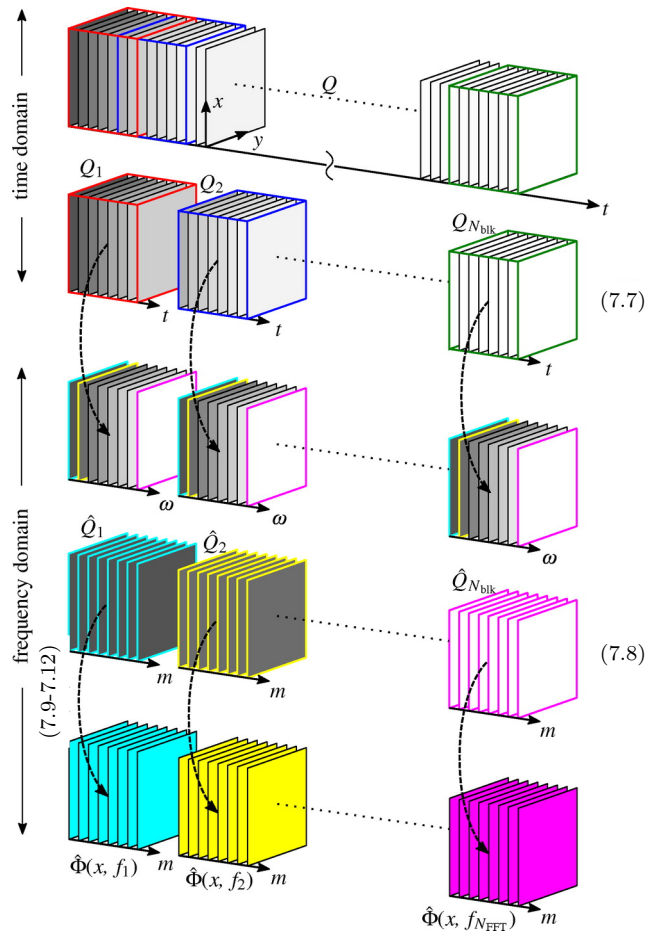


Figure 7.1. Schematic of the SPOD algorithm (taken from [50]). The numbers in parentheses denote the equations used.

reorganized by creating new blocks of identical temporal-frequencies,

$$\hat{Q} = \begin{bmatrix} | & | & & | \\ \hat{q}^{(1)} & \hat{q}^{(2)} & \dots & \hat{q}^{(N)} \\ | & | & & | \end{bmatrix}, \quad \hat{Q} \in \mathbb{C}^{M \times N} \quad (7.8)$$

where M is now the number of spatial points times the number of blocks and N is block length in time. Proper orthogonal decomposition is then performed separately on each temporal-frequency block via either traditional POD

$$\hat{C} = \frac{1}{N-1} \hat{Q} \hat{Q}^H, \quad (7.9)$$

$$\hat{C} W \hat{\Phi} = \hat{\Phi} \hat{\Lambda}, \quad (7.10)$$

or the method of snapshots,

$$\hat{Q}^H W \hat{Q} \hat{\Psi} = \hat{\Psi} \hat{\Lambda}, \quad (7.11)$$

$$\hat{\Phi} = \hat{Q} \hat{\Psi}, \quad (7.12)$$

where H denotes the Hermitian transpose, W is a weighting matrix, Φ is the set of deterministic spatial functions, Λ is the eigen-values, and Ψ is the coefficient matrix.

The linear stochastic estimation portion of the technique is described by Adrian [2]. This process uses a linear sum, L_{ij} , of additional measurements, y_j , to approximate a measured signal, x_i ,

$$x_i^{LSE} = L_{ij} y_j, \quad (7.13)$$

where

$$L_{ij} = \langle x_i y_k \rangle \langle y_j y_k \rangle^{-1}. \quad (7.14)$$

When combined with SPOD, the estimation matrix, L , becomes

$$L = (\hat{\Psi} \hat{y}^H) (\hat{y} \hat{y}^H)^{-1}, \quad (7.15)$$

which allows for an estimated version of the coefficient matrix to be calculated

$$\hat{\Psi}^E = L \hat{y}. \quad (7.16)$$

The estimated coefficient matrix contains portions of the original signal that best resemble the additional sensor data. Assuming that the additional sensor data represents signal contamination of the original signal, a filtered coefficient matrix can be computed from the difference between the original and estimated coefficient matrices.

$$\hat{\Psi}^F = \hat{\Psi} - \hat{\Psi}^E. \quad (7.17)$$

A filtered signal, Q^F can be constructed by using the filtered coefficient matrix and the spatial functions,

$$\hat{Q} = \hat{\Psi}^F \hat{\Phi}^H. \quad (7.18)$$

7.3 Filtering Experimental Data

The filtering technique described in the preceding section was applied to the same data sets that were shown in Figure 4.7. Simultaneous accelerometer and microphone measurements were made alongside the optical wavefront measurements. The locations of some of the additional sensors are shown in Figure 7.2 with a CAD drawing of the test section in Figure 7.3. Table 7.1 shows a list of the additional sensors including the number designation used in Figures 7.2 and 7.3, the model of the sensor and preamplifier used as well as a sensor grouping designation. All of the test-section mounted sensors are shown in their approximate locations in Figure 7.3 in a view that is looking at the wind-tunnel model from inside of the test-section with the flow moving from left-to-right. The dashed box represent the optical window on the opposite side of the tunnel from the model which was moved up or downstream depending on the beam angle relative to the flow. Sensors 11-13 were attached to this optical window and moved with it. The picture in Figure 7.2 was taken from the opposite side of the test-section and model that is shown in Figure 7.3 and as such the flow goes from right-to-left.

Two microphones were used for ambient measurement (a ACO 7016B [12] and a Brüel & Kjær 4939 [8]), four microphones were used for test-section noise measurement (PCB 103B02 [43]), and ten accelerometers were located throughout the setup (PCB 352C33 [44]). One of the ambient microphones was mounted to the top of the optics bench facing the test-section and can be seen in Figure 7.2 just to the right of the primary lens and the other ambient microphone was hanging below the optics bench end towards the test-section.

The test-section microphones were in groups of two either upstream or downstream from the

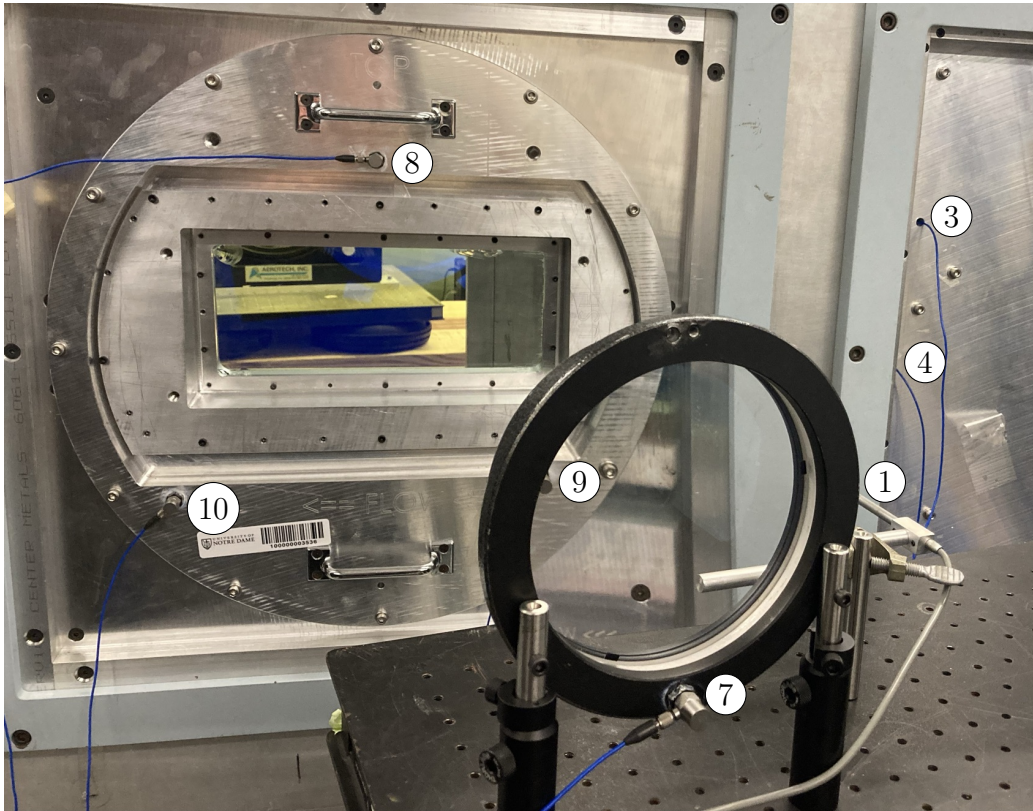


Figure 7.2. The locations of some of the additional sensors used in the LSE-SPOD filtering. The sensors are labeled with the sensor numbers, see Table 7.1.

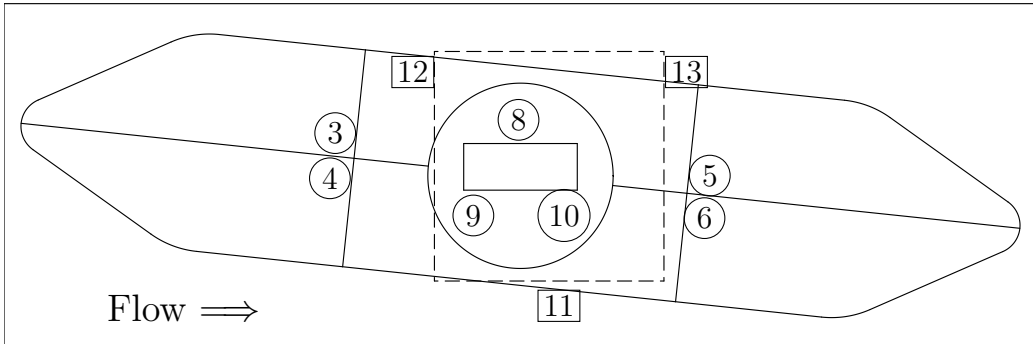


Figure 7.3. CAD drawing view of the inside of the test-section with some of the sensor locations labeled. Flow is from left to right. The numbers in the circles are the sensor numbers on the model side of the test-section. The numbers in the square are the sensor numbers opposite of the model side. The dashed line represents the optics window opposite of the model for the beam angle of 90°. The window was moved up and downstream depending on the beam angle.

TABLE 7.1

ADDITIONAL SENSORS USED THE THE LSE-SPOD FILTERING.

Channel	Sensor Type	Model	Preamp	Group
1	Microphone	ACO 7016B	B&K 2690	Ambient
2	Microphone	B&K 4939	B&K 2690	Ambient
3	Microphone	PCB 103B02	PCB 483C	Test Section
4	Microphone	PCB 103B02	PCB 483C	Test Section
5	Microphone	PCB 103B02	PCB 483C	Test Section
6	Microphone	PCB 103B02	PCB 483C	Test Section
7	Accelerometer	PCB 352C33	PCB 483C	Primary Lens
8	Accelerometer	PCB 352C33	PCB 483C	Test Section
9	Accelerometer	PCB 352C33	PCB 483C	Test Section
10	Accelerometer	PCB 352C33	PCB 483C	Test Section
11	Accelerometer	PCB 352C33	PCB 482A22	Test Section
12	Accelerometer	PCB 352C33	PCB 482A22	Test Section
13	Accelerometer	PCB 352C33	PCB 482A22	Test Section
14	Accelerometer	PCB 352C33	PCB 482A22	Optics Bench
15	Accelerometer	PCB 352C33	PCB 482A22	Return Mirror
16	Accelerometer	PCB 352C33	PCB 482A22	Return Mirror

optical beam by about 20-inches, with the upstream microphone locations viewable in Figure 7.2 (sensors 3 and 4) and shown in Figure 7.3. The model installed in the test-section represents the outside of an aircraft fuselage with a 5-foot diameter and is angled to account for the aircraft's angle-of-attack (6°) for steady-level-flight at cruise. This results in the fuselage model being shifted approximately 2-inches higher from the test-section centerline upstream at the microphone location. The duct microphones were placed about 2.75-inches from the model centerline.

There were six accelerometers attached to the test-section windows, with three being on each side as shown in Figure 7.3. The locations of the three accelerometers (sensors 8-10) on the model side can be seen in Figure 7.2, the three accelerometers on the other window used the opposite pattern (two high and one low). The optical window on the far side of the test-section was moved laterally depending on the angle of the beam relative to the flow. One accelerometer was placed on the primary lens (also shown, sensor 7) and one was placed in the center of the optics bench. The last two accelerometers were located on the back of the return mirror with one on the top and the other on the side.

The power-spectra of all of the sensors at the three Mach numbers are shown in Figure 7.4. These plots are presented as Strouhal number per unit characteristic length with the different groups of sensors shown together. The blade-passing frequency for these data sets is at a St/l of approximately 3 m^{-1} with a clear and consistent narrow-band signal at that St/l for all but the $M = 0.3$ run, which has a slight increase in signal for some of the sensors. For the $M = 0.5$ case there is an additional strong narrow-band signal at 20 m^{-1} for all sensors and a slightly broader signal at 38 m^{-1} that is only present in the test-section mounted sensors that may be due to extra fan vibration which was limiting the top speed of the wind-tunnel. The test-section mounted microphones are picking up boundary layer acoustic noise above St/l of approximately 20 m^{-1} .

Two variants of the filtering technique were tried. The first was a standard LSE-SPOD technique in which the spectral POD was performed on the data set that was Fourier transformed in time only. For the second technique, which will be referred to here as LSE-MSPOD, the spectral POD was applied to a data set in which the Fourier transform was performed in all dimensions of space and time, which is a portion of the computation for the multidimensional spectral estimation. Figures 7.5 and 7.6 show multidimensional power spectrum plots at a temporal block length of 2^{10} with no overlap. These plots show the $f \cdot \xi_x$ plane of the multidimensional spectrum that captures horizontally-moving (streamwise) plane waves with a portion of the acoustic cone isosurface wrapping behind it. Both of these methods performed effectively identically to one another with

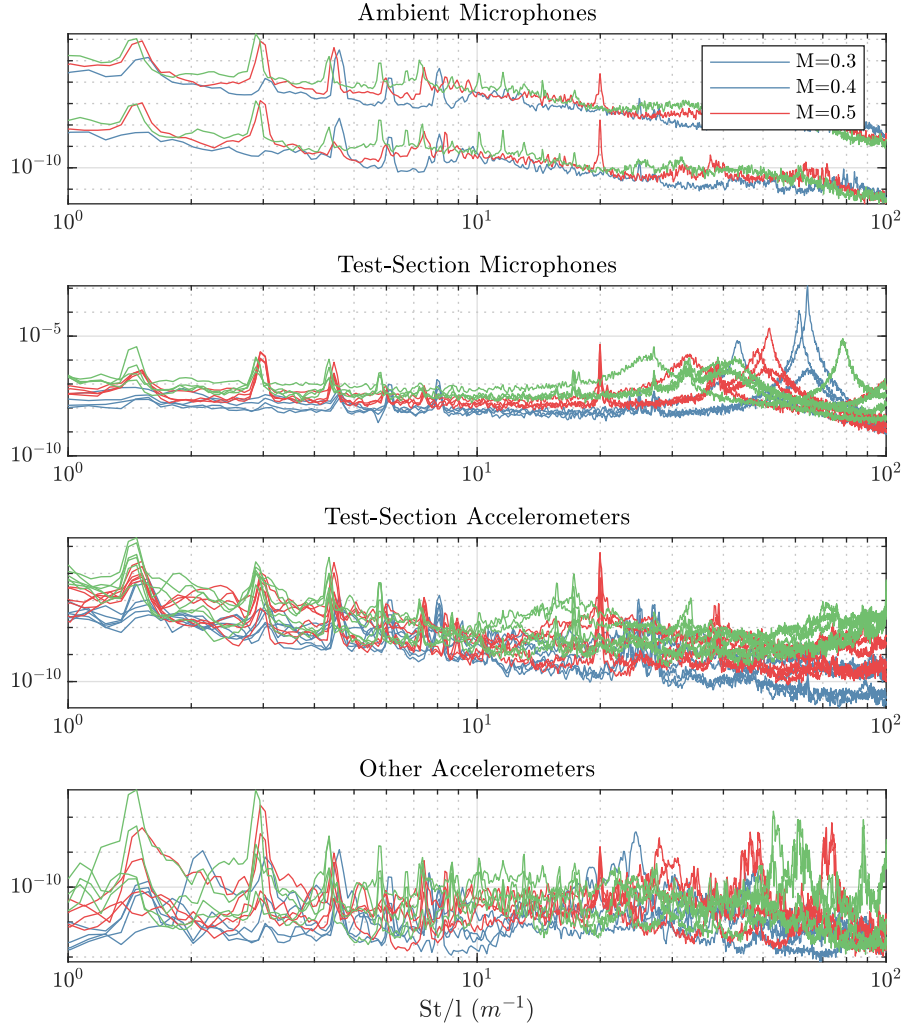


Figure 7.4. Power-spectra of the additional sensor measurements at the three Mach numbers tested. The x-axis is in Strouhal number per characteristic length (St/l).

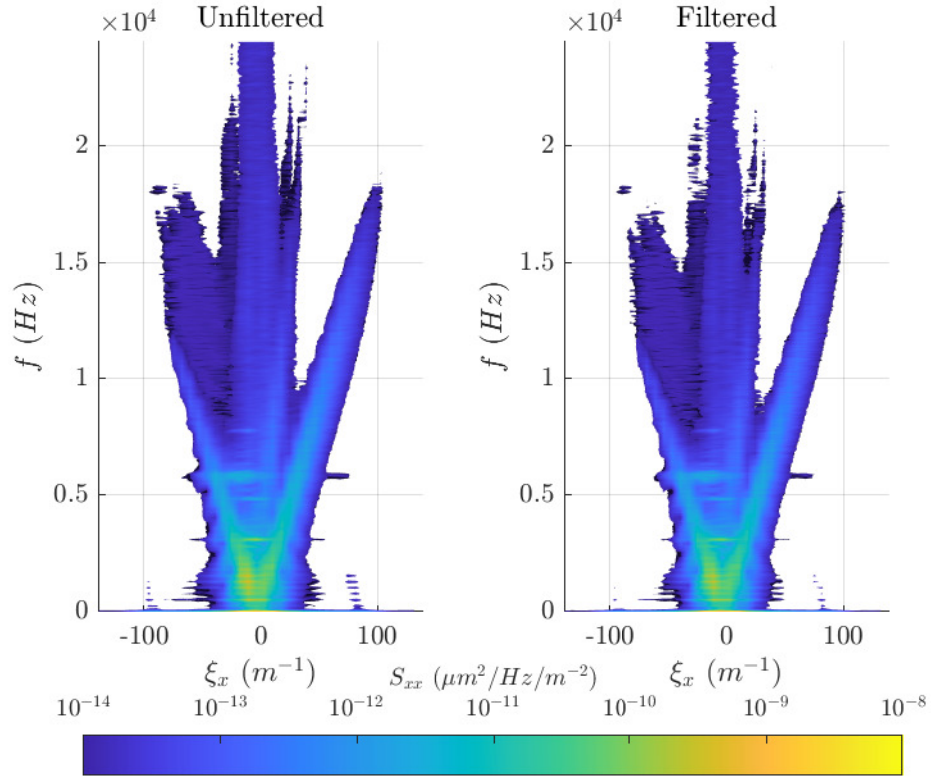


Figure 7.5. A multidimensional power spectrum of an unfiltered wavefront and the same wavefront filtered with the LSE-SPOD method using all 16 additional microphone or accelerometer measurements.

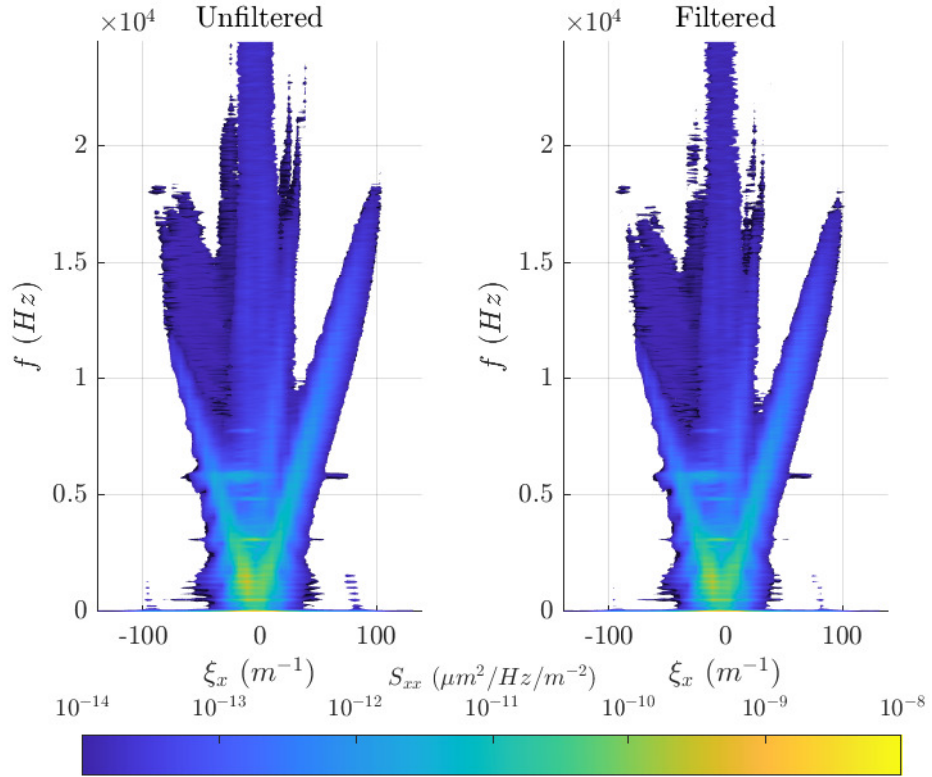


Figure 7.6. A multidimensional power spectrum of an unfiltered wavefront and the same wavefront filtered with the LSE-MSPOD method using all 16 additional microphone or accelerometer measurements.

TABLE 7.2

OPD_{RMS} (μm) COMPARISON OF USING DIFFERENT COMBINATIONS OF ADDITIONAL SENSOR INFORMATION IN THE LSE-MSPOD FILTERING PROCESS.

	M=0.3	M=0.4	M=0.5
Original	0.0561	0.0521	0.0824
Tip/Tilt Removal	0.0120(78.6%)	0.0195(62.6%)	0.0291(64.7%)
Accelerometers	0.0102(81.8%)	0.0168(67.7%)	0.0251(69.5%)
Ambient Microphones	0.0103(81.7%)	0.0170(67.3%)	0.0254(69.1%)
Duct Microphones	0.0103(81.6%)	0.0170(67.3%)	0.0255(69.0%)
Test-Section Sensors	0.0103(81.6%)	0.0168(67.8%)	0.0252(69.4%)
All Sensors	0.0099(82.3%)	0.0163(68.8%)	0.0242(70.6%)
Velocity Filter	0.0090(83.9%)	0.0146(72.1%)	0.0217(73.7%)
+All Sensors	0.0075(86.7%)	0.0122(76.7%)	0.0181(78.0%)

a 14.2% drop in overall RMS value of the filtered wavefront (both time and space). There is a significant drop in the signal at the blade-passing frequency and its harmonics, especially at the higher spatial frequencies. The stationary signal information is also significantly reduced along with the high temporal-frequency acoustic signal. The aero-optical boundary layer signal is also partially reduced, which is most noticeable at higher temporal-frequencies. Some of this lost signal can be restored by increasing the overlap of the temporal frequency blocks, but this also restores some of the unwanted high temporal-frequency contamination.

Table 7.2 shows the time averaged OPD_{RMS} of three different data sets at a beam angle through the test-section of 90°. The data sets were at Mach numbers of 0.3, 0.4, and 0.5 and had an unfiltered OPD_{RMS} of 0.0561, 0.0521, and 0.0824 μm respectively. Note that in the raw processed wavefronts, the OPD_{RMS} at a Mach number of 0.3 was higher than the 0.4 case. There was a significant drop of between 62.6 and 78.6% in the OPD_{RMS} by removing the Zernike modes corresponding to tip and tilt. It is at this point the Mach number of 0.4 case has a higher OPD_{RMS} than the 0.3 case as would be expected [20]. Note that it is standard practice to remove optical tip/tilt from wavefront measurements, since tip/tilt is largely imposed by the measurement optics rather than the actual aero-optical flow.

Table 7.2 also shows the effect of five different combinations of additional sensors that were used for filtering with the LSE-MSPOD process (the bracketed percentage in Table 7.2 shows the percent reduction in OPD_{RMS} due to the filtering). The first set was all of the accelerometers which resulted in an additional drop in OPD_{RMS} of between 3 and 5%. The second and third sets used either the ambient or duct microphones and those sets had slightly less reduction than the accelerometers. The fourth set was the test-section sensors comprised of six window mounted accelerometers and four duct mounted microphones. This set of sensors performed the same as all of the accelerometers, while the use of all of the additional sensors in the last set performed the best, with an additional reduction in OPD_{RMS} of 4 to 6% from the tip/tilt removal cases.

A velocity filter was also tried in addition to just the tip/tilt removal or in conjunction with tip/tilt and all the sensors being used in the LSE-MSPOD process. The velocity filter performed better than the all-sensors removal case by an additional 1.5 to 3%. When all sensors were used with LSE-MSPOD on the velocity filtered wavefronts an additional 3 to 4% of the OPD_{RMS} was removed compared to just the velocity-filtered case or an additional 8.1% reduction for only doing tip/tilt removal on the Mach number of 0.3 case or 14.1 and 13.3% reduction for the 0.4 and 0.5 Mach number cases.

In summary, Table 7.2 shows that using either the temporal or multidimensional version of the LSE-SPOD filtering technique can help remove some of the narrow-band acoustic and vibration reduction in an optical wavefront. These temporally narrow-band signals have broadband spatial content that is attenuated. This additional reduction does seem to be somewhat tied to the number of sensors used with more sensors having a greater impact on the signal reduction. Since the vibrations and acoustics have the same primary source, the wind-tunnel fan, they seems to do a relatively equivalent job at filtering the optical contamination. Accelerometers have the benefit of easier installation but the microphones do not necessarily have to be installed inside of the wind-tunnel.

CHAPTER 8

CONCLUSION

BIBLIOGRAPHY

1. 2pem. A schematic illustration of a shwfs. https://commons.wikimedia.org/wiki/File:Shack_Hartmann_WFS_lensletarray.svg.
2. R. J. Adrian. On the role of conditional averages in turbulence theory. In *Symposia on Turbulence in Liquids*, 1975.
3. M. An, I. Gertner, M. Rofheart, and R. Tolimieri. Discrete fast fourier transorm algorithms: A tutorial survey. *Advances in Electronics and Electron Physics*, 80:1–67, 1991. doi: 10.1016/S0065-2539(08)60607-1.
4. R. B. Blackman and J. W. Tukey. *The Measurement of Power Spectra - From the Point of View of Communications Engineering*. Dover, 1958.
5. M. Born and E. Wolf. *Principles of Optics*. Pergamon, 1965.
6. S. Braun, editor. *Encyclopedia of Vibration*. Academic Press, 2001.
7. Brüel & Kjær. 2670. <https://www.bksv.com/-/media/literature/Product-Data/bp1584.ashx>, November 2018. Product Data.
8. Brüel & Kjær. 4939. <https://www.bksv.com/-/media/literature/Product-Data/bp1851.ashx>, October 2021. Product Data.
9. S. Butterworth. On the theory of filter amplifiers. *Experimental Wireless and the Wireless Engineer*, 7:536–541, 1930.
10. B. L. Catron, M. R. Rennie, S. Gordeyev, and E. J. Jumper. Effect of acoustic disturbances on aero-optical measurements. In *2018 Plasmadynamics and Lasers Conference*, 2018. doi: 10.2514/6.2018-3903.
11. B. L. Catron, M. R. Rennie, S. Gordeyev, and E. J. Jumper. Filtering of acoustic disturbances from aero-optical measurements. In *AIAA Scitech 2020 Forum*, 2020. doi: 10.2514/6.2020-0683.
12. A. CO. Sound measurement microphone. <https://www.aco-japan.co.jp/pdf/en-microphone.pdf>. Product Catalog.
13. N. De Lucca, S. Gordeyev, E. J. Jumper, and D. J. Wittich. Effects of engine acoustic waves on optical environment around turrets in-flight on aaol-t. *Optical Engineering*, 57(6), 2018. doi: 10.1117/1.OE.57.6.064107.
14. O. T. . E. Director. Fy99 annual report - airborne laser (abl). <https://www.globalsecurity.org/military/library/budget/fy1999/dot-e/airforce/99abl.html>, 2000.
15. E. J. Fitzgerald and E. J. Jumper. The optical distortion mechanism in a nearly incompressible free shear layer. *Journal of Fluid Mechanics*, 512:153–189, 2004. doi: 10.1017/S0022112004009553.
16. G. Gabard and R. Astley. A computational mode-matching approach for sound propagation in three-dimensional ducts with flow. *Journal of Sound and Vibration*, 315:1103–1124, 2008. doi: 10.1016/j.jsv.2008.02.015.

17. J. M. Geary. *Introduction to Wavefront Sensors*. SPIE Optical Engineering Press, 1995.
18. J. H. Gladstone and T. P. Dale. Researches on the refraction, dispersion, and sensitiveness of liquids. *Philosophical Transactions of the Royal Society of London*, 153:317–343, 1863.
19. J. W. Goodman. *Introduction to Fourier Optics*. McGraw-Hill, 1968.
20. S. Gordeyev, A. E. Smith, J. A. Cress, and E. J. Jumper. Experimental studies of aero-optical properties of subsonic turbulent boundary layers. *Journal of Fluid Mechanics*, 740:214–253, 2014. doi: 10.1017/jfm.2013.658.
21. D. P. Greenwood. Bandwidth specification for adaptive optics systems. *Journal of the Optical Society of America*, 67(3):390–393, 1977. doi: 10.1364/JOSA.67.000390.
22. R. W. Hamming. *Digital Filters*. Dover, 3rd edition, 1998.
23. L. Huang, M. Idir, K. Kaznatcheev, L. Zhou, and A. Asundi. Comparison of two-dimensional integration methods for shape reconstruction from gradient data. *Optics and Lasers in Engineering*, 64, 2015. doi: 10.1016/j.optlaseng.2014.07.002.
24. F. Jacobsen and P. M. Iller Juhl. *Fundamentals of General Linear Acoustics*. John Wiley & Sons, 2013.
25. Z. Ji and Z. Fang. Numerical mode-matching approach for acoustic attenuation prediction of expansion chambers with single inlet and double outlets. In *Proceedings of Meetings on Acoustics*, Vol. 19, 2013. doi: 10.1121/1.4799442.
26. W. C. G. Jr., Y. Hidaka, and T. Tanzawa. Refractivity of combustion gases. *Combustion and Flame*, 40:213–219, 1980. doi: 10.1016/0010-2180(81)90124-3.
27. E. J. Jumper and E. J. Fitzgerald. Recent advances in aero-optics. *Progress in Aerospace Sciences*, 37(3):299–339, 2001. doi: 10.1016/S0376-0421(01)00008-2.
28. E. J. Jumper, M. A. Zenk, S. Gordeyev, D. Cavalieri, and M. R. Whiteley. Airborne aero-optics laboratory. *Optical Engineering*, 52(7), 2013. doi: 10.1117/1.OE.52.7.071408.
29. M. V. Klein and T. E. Furtak. *Optics*. John Wiley & Sons, 2nd edition, 1986.
30. D. T. Kyrazis. Airborne laser laboratory departure from kirtland air force base and a brief history of aero-optics. *Optical Engineering*, 52(7), 2013. doi: 10.1117/1.OE.52.7.071403.
31. N. D. Lucca, S. Gordeyev, A. Smith, E. Jumper, M. Whiteley, and T. Neale. The removal of tunnel vibration induced corruption in aero-optical measurements. In *45th AIAA Plasmadynamics and Lasers Conference*, 2014. doi: 10.2514/6.2014-2494.
32. K. P. Lynch, R. Spillers, N. E. Miller, D. R. Guildenbecher, and S. Gordeyev. Aero-optical measurements of a mach 8 boundary layer. In *AIAA AVIATION 2021 Forum*, 2021. doi: 10.2514/6.2021-2831.
33. P.-Y. Madec. Overview of deformable mirror technologies for adaptive optics and astronomy. In *SPIE Astronomical Telescopes + Instrumentation*, 2012. doi: 10.1117/12.924892.
34. V. N. Mahajan. Strehl ratio for primary aberrations: some analytical results for circular and annular pupils. *Journal of the Optical Society of America*, 72(9):1258–1266, 1982. doi: 10.1364/JOSA.72.001258.
35. V. N. Mahajan. Strehl ratio for primary aberrations in terms of their aberration variance. *Journal of the Optical Society of America*, 73(6):860–861, 1983. doi: 10.1364/JOSA.73.000860.

36. A. McAlpine, R. Astley, V. Hii, N. Baker, and A. Kempton. Acoustic scattering by an axially-segmented turbofan inlet duct liner at supersonic fan speeds. *Journal of Sound and Vibration*, 294:780–806, 2006. doi: 10.1016/j.jsv.2005.12.039.
37. J. H. McClellan. Multidimensional spectral estimation. *Proceedings of the IEEE*, 70(9):1029–1039, 1982. doi: 10.1109/PROC.1982.12431.
38. P. M. Morse and K. U. Ingard. *Theoretical Acoustics*. McGraw-Hill, 1968.
39. P. A. Mosier-Boss, S. H. Lieberman, and R. Newbery. Fluorescence rejection in raman spectroscopy by shifted-spectra, edge detection, and fft filtering techniques. *Applied Spectroscopy*, 49(5):630–638, 1995. doi: 10.1366/0003702953964039.
40. M. L. Munjal. *Acoustics of Ducts and Mufflers*. John Wiley & Sons, 2nd edition, 2014.
41. A. M. Nightingale and S. Gordeyev. Shack-hartmann wavefront sensor image analysis: A comparison of centroiding methods and image-processing techniques. *Optical Engineering*, 52(7), 2013. doi: 10.1117/1.OE.52.7.071413.
42. R. J. Noll. Zernike polynomials and atmospheric turbulence. *Journal of the Optical Society of America*, 66(3):207–211, 1976. doi: 10.1364/JOSA.66.000207.
43. PCB Piezotronics. 103B02. https://wwwpcb.com/contentStore/docs/pcb_corporate/pressure/products/specsheets/103b02_c.pdf, October 2020. Product Specifications - Revision: C.
44. PCB Piezotronics. 352C33. https://wwwpcb.com/contentStore/docs/pcb_corporate/vibration/products/specsheets/352c33_h.pdf, April 2008. Product Specifications - Revision: H.
45. Peerless. XT25SC90-04. <https://tymphony-driver-files.s3.us-west-1.amazonaws.com/files/driver/pdfs/XT25SC90-04.Rev1.MP1%20-%20Product%20Sheet.pdf>, August 2021. Product Sheet - Revision: 1.
46. C. Porter, M. Rennie, and E. Jumper. Aero-optic effects of a wingtip vortex. *AIAA Journal*, 51(7):1533–1541, 2013. doi: 10.2514/1.J050899.
47. Powell. Propagation of a pressure pulse in a compressible flow. *The Journal of the Acoustical Society of America*, 31(11):1527–1535, 1959. doi: 10.1121/1.1907660.
48. R. H. Randall. *An Introduction to Acoustics*. Dover Publications, 1951.
49. R. M. Rennie, D. A. Duffin, and E. J. Jumper. Characterization and aero-optic correction of a forced two-dimensional weakly compressible shear layer. *AIAA Journal*, 46(11):2787–2795, 2008. doi: 10.2514/1.35290.
50. O. T. Schmidt and T. Colonius. Guide to spectral proper orthogonal decomposition. *AIAA Journal*, 58(3):1023–1033, 2020. doi: 10.2514/1.J058809.
51. G. Schulze, A. Jirasek, M. M. L. Yu, A. Lim, R. F. B. Turner, and M. W. Blades. Investigation of selected baseline removal techniques as candidates for automated implementation. *Applied Spectroscopy*, 59(5):545–574, 2005. doi: 10.1366/0003702053945985.
52. H. G. Schulze, R. B. Foist, K. Okuda, A. Ivanov, and R. F. B. Turner. A small-window moving average-based fully automated baseline estimation method for raman spectra. *Applied Spectroscopy*, 66(7):757–764, 2012. doi: 10.1366/11-06550.
53. J. P. Siegenthaler. *Guidelines for Adaptive-Optic Correction Based on Aperture Filtration*. Doctoral dissertation, University of Notre Dame, Notre Dame, IN, 2008.

54. J. P. Siegenthaler, S. Gordelyev, and E. Jumper. Shear layers and aperture effects for aero-optics. In *36th AIAA Plasmadynamics and Lasers Conference*, 2005. doi: 10.2514/6.2005-4772.
55. A. E. Smith, S. Gordelyev, and E. J. Jumper. Recent measurements of aero-optical effects caused by subsonic boundary layers. *Optical Engineering*, 52(7), 2013. doi: 10.1117/1.OE.52.7.071404.
56. H. A. Stine and W. Winovich. Light diffusion through high-speed turbulent boundary layers. Technical Report RM A56B21, National Advisory Committee For Aeronautics, May 1956.
57. S. L. Valley. Handbook of geophysics and space environments. Technical Report ADA056800, Air Force Cambridge Research Laboratories, April 1965.
58. K. Wang and M. Wang. Aero-optics of subsonic turbulent boundary layers. *Journal of Fluid Mechanics*, 696:122–151, 2012. doi: 10.1017/jfm.2012.11.
59. M. R. Whiteley and . S. Gibson. Adaptive laser compensation for aero-optics and atmospheric disturbances. In *38th Plasmadynamics and Lasers Conference*, 2007. doi: 10.2514/6.2007-4012.
60. A. G. Wilson. Propagation of acoustic perturbations in non-uniform ducts with non-uniform mean flow using eigen analysis in general curvilinear coordinate systems. *Journal of Sound and Vibration*, 443:605–636, 2019. doi: 10.1016/j.jsv.2018.11.023.
61. J. Zhao, H. Lui, D. I. McLean, and H. Zeng. Automated autofluorescence background subtraction algorithm for biomedical raman spectroscopy. *Applied Spectroscopy*, 61(11):1225–1232, 2007. doi: 10.1366/000370207782597003.